8-2015

THE EFFECT OF HIGH-PRESSURE DEVITRIFICATION AND DENSIFICATION ON BALLISTIC-PENETRATION RESISTANCE OF FUSED SILICA

Vasudeva Avuthu
Clemson University, vavuthu@g.clemson.edu

THE EFFECT OF HIGH-PRESSURE DEVITRIFICATION AND Ddensification ON BALLISTIC-PENETRATION RESISTANCE OF FUSED SILICA

A Thesis
Presented to
the Graduate School of
Clemson University

In Partial Fulfillment
of the Requirements for the Degree
Master of Science
Mechanical Engineering

---

by
Vasudeva Reddy Avuthu
August 2015

Accepted by:
Dr. Mica Grujicic, Committee Chair
Dr. Chenning Tong
Dr. Jay Ochterbeck

ABSTRACT

Despite the clear benefits offered by more advanced transparent materials, (e.g. transparent ceramics offer a very attractive combination of high stiffness and high hardness levels, highly-ductile transparent polymers provide superior fragment-containing capabilities, etc.), ballistic ceramic-glass like fused-silica remains an important constituent material in a majority of transparent impact-resistant structures (e.g. windshields and windows of military vehicles, portholes in ships, ground vehicles and spacecraft) used today. Among the main reasons for the wide-scale use of glass, the following three are most frequently cited: (i) glass-structure fabrication technologies enable the production of curved, large surface-area, transparent structures with thickness approaching several inches; (ii) relatively low material and manufacturing costs; and (iii) compositional modifications, chemical strengthening, and controlled crystallization have been demonstrated to be capable of significantly improving the ballistic properties of glass. In the present work, the potential of high-pressure devitrification and densification of fused-silica as a ballistic-resistance-enhancement mechanism is investigated computationally.

In the first part of the present work, all-atom molecular-level computations are carried out to infer the dynamic response and material microstructure/topology changes of fused silica subjected to ballistic impact by a nanometer-sized hard projectile. The analysis was focused on the investigation of specific aspects of the dynamic response and of the microstructural changes such as the deformation of highly sheared and densified regions, and the conversion of amorphous fused silica to SiO_2 crystalline allotropic modifications (in particular, α-quartz and stishovite). The microstructural changes in question were determined by carrying out a post-processing atom-coordination procedure. This procedure suggested the formation of high-density

stishovite (and perhaps α-quartz) within fused silica during ballistic impact. To rationalize the findings obtained, the all-atom molecular-level computational analysis is complemented by a series of quantum-mechanics density functional theory (DFT) computations. The latter computations enable determination of the relative potential energies of the fused silica, α-quartz and stishovite under ambient pressure (i.e. under their natural densities) as well as under imposed (as high as 50 GPa) pressures (i.e. under higher densities) and shear strains. In addition, the transition states associated with various fused-silica devitrification processes were identified.

In the second part of the present work, the molecular-level computational results obtained in the first portion of the work are used to enrich a continuum-type constitutive model (that is, the so-called Johnson-Holmquist-2, JH2, model) for fused silica. Since the aforementioned devitrification and permanent-densification processes modify the response of fused silica to the pressure as well as to the deviatoric part of the stress, changes had to be made in both the JH2 equation of state and the strength model. To assess the potential improvements with respect to the ballistic-penetration resistance of this material brought about by the fused-silica devitrification and permanent-densification processes, a series of transient non-linear dynamics finite element analyses of the transverse impact of a fused-silica test plate with a solid right-circular cylindrical steel projectile was conducted. The results obtained revealed that, provided the projectile incident velocity and, hence, the attendant pressure, is sufficiently high, fused silica can undergo impact-induced energy-consuming devitrification, which improves its ballistic-penetration resistance.

Keywords: Ceramic-glass, fused-silica, devitrification, ballistic-resistance, all-atom molecular-level computations, Johnson-Holmquist-2

DEDICATION

This thesis would have been impossible without the unwavering love and support from my father, Mr. Jagadeeswara Reddy Avuthu, my mother, Mrs. Vara Lakshmi Avuthu, and my brother Vivekananda Reddy Avuthu to whom this thesis is dedicated.

ACKNOWLEDGEMENTS

I wish to express my sincere gratitude to my advisor, Professor Mica Grujicic, for his continuous encouragement, supervision, useful suggestions, and support throughout this research endeavor. His extensive knowledge and timely suggestions have been helpful in providing elegant solutions to the problems encountered throughout this research project.

My sincere thanks is also due to my advisory committee members Professor Chenning Tong, and Professor Jay Ochterbeck for their valuable suggestions during the course of this research project. Other faculty members of the department of Mechanical Engineering at Clemson University and the administrative staff are also greatly acknowledged for their support.

This acknowledgement will not be complete without the mention of my friends and colleagues at Clemson University whose valuable support and insightful discussions have helped mold this research into its existing form. Finally, I would like to thank my family and friends for their continuous support and encouragement during the whole tenure of my research.

TABLE OF CONTENTS

Page

TABLE OF CONTENTS (Continued)

TABLE OF CONTENTS (Continued)

TABLE OF CONTENTS (Continued)

LIST OF TABLES

Table Page

LIST OF FIGURES

Figure Page

LIST OF FIGURES (Continued)

CHAPTER 1: INTRODUCTION AND BACKGROUND, AND THESIS OUTLINE

1.1. Introduction and Background

Currently, a number of materials and design strategies are employed in transparent, ballistic-impact-resistant vehicle structures (e.g. windshields, door windows, viewports, etc.). Among the most recently introduced transparent materials and technologies, the following have received the most attention: (a) transparent crystalline ceramics (e.g. aluminum-oxinitride spinel, AlON, sapphire [1]); (b) new transparent polymer materials (e.g. transparent nylon [2]); (c) new interlayer technologies (e.g. polyurethane bonding layers [3]); and (d) new laminate structure designs [e.g. 4]. Despite the clear benefits offered by these materials and technologies (e.g. transparent ceramics offer a very attractive combination of high stiffness and high hardness levels, highly ductile transparent polymers provide superior fragment containing capabilities, etc.), ballistic ceramic glass like fused-silica remains an important constituent material in a majority of transparent impact-resistant structures used today. Among the main reasons for the wide-scale use of glass, the following three are most frequently cited: (i) glass-structure fabrication technologies enable the production of curved, large surface-area, transparent structures with thickness approaching several inches; (ii) relatively low material and manufacturing costs; and (iii) compositional modifications, chemical strengthening, and controlled crystallization have been demonstrated to be capable of significantly improving the ballistic properties of glass [e.g. 2].

While ceramic glasses are widely used in blast-/ballistic-resistant transparent structures, the intrinsic ballistic-resistance of these materials is lower compared to the more advanced transparent-materials/strategies mentioned above. This is the reason that there is a considerable amount of research activity aimed at improving the intrinsic ballistic-resistance of these materials.

In the present work, the potential of ceramic-glass devitrification and permanent-densification on the ability of this material to absorb the kinetic energy and, thus, defeat the ballistic impactor is investigated computationally. Since the phenomena and processes associated with glass devitrification and permanent densification take place at the atomic length-scale, all-atom atomistic-level and quantum-mechanical calculations had to be employed. On the other hand, in order to assess the potential of glass devitrification and permanent densification on the ballistic-penetration resistance of the ceramic glasses, continuum-level finite-element type calculations of the projectile/target-plate interactions had to be carried out. The work conducted is presented in Chapters II, III and IV. A brief description of the work presented in these chapters is given below. This is followed by Section V, in which a list of key findings and conclusions resulting from the present work is given and suggestions are made for future work.

In the early stage of the present work, the continuum-level computational analysis was carried out using the commercial software AUTODYN from Century Dynamics. The work conducted is summarized in Chapter II. Unfortunately, the user license for AUTODYN was not renewed and the work presented in Chapter II had to be terminated and re-directed towards the available finite-element package ABAQUS/Explicit from Dassault Systèmes. In the early stage of the present work, molecular-level modeling and simulations of the high-pressure volumetric response and irreversible densification of a prototypical soda-lime glass are first employed. The molecular-simulation results obtained were next used to modify the pressure vs. ***degree-of-compression*** (the negative of volumetric strain) and yield strength vs. pressure relations in order to account for the effects of irreversible densification. These relations are next used to upgrade the Equation of State and the strength constitutive laws of an existing material model for glass. This was followed by a set of transient non-linear dynamics calculations of the transverse impact

of a glass test plate with a solid right-circular cylindrical steel projectile. The results obtained show that irreversible densification can provide only a minor improvement in the ballistic resistance of glass and only in the case of high-velocity (ca. 1000m/s) projectiles. Furthermore, it was demonstrated that if through modifications in glass chemistry and microstructure, the key irreversible compaction parameters can be adjusted, significant improvements in the glass ballistic resistance can be attained and over a relatively wide range of projectile velocities. Per recommendation of the sponsor, the Army Research Laboratory, the subsequent work overviewed below focused on fused silica, a ceramic glass which possesses a higher intrinsic ballistic-penetration resistance than soda-lime glass.

In the first part of the work dealing with fused silica, overviewed in Chapter III, the behavior of this material under high pressure and shear stresses is investigated using atomic-scale and quantum-mechanical computational methods and tools. Towards that end, all-atom molecular-level computations are carried out to infer the dynamic response and material microstructure/topology changes of fused silica subjected to ballistic impact by a nanometer-sized hard projectile. The analysis was focused on the investigation of specific aspects of the dynamic response and of the microstructural changes such as the deformation of highly sheared and densified regions, and the conversion of amorphous fused silica to SiO_2 crystalline allotropic modifications (in particular, α-quartz and stishovite). The microstructural changes in question were determined by carrying out a post-processing atom-coordination procedure. This procedure suggested the formation of stishovite (and perhaps α-quartz) within fused silica during ballistic impact. To rationalize the findings obtained, the all-atom molecular-level computational analysis is complemented by a series of quantum-mechanics density functional theory (DFT) computations. The latter computations enable determination of the relative potential energies of

the fused silica, α-quartz and stishovite under ambient pressure (i.e. under their natural densities) as well as under imposed (as high as 50 GPa) pressures (i.e. under higher densities) and shear strains. In addition, the transition states associated with various fused-silica devitrification processes were identified.

In the second part of the work dealing with fused silica, overviewed in Chapter IV, our molecular-level computational results pertaining to the response of fused silica to high pressures (and shear stresses), as reported in Chapter III, are used to enrich a continuum-type constitutive model (that is, the so-called Johnson-Holmquist-2, JH2, model) for this material. Since the aforementioned devitrification and permanent-densification processes modify the response of fused silica to the pressure as well as to the deviatoric part of the stress, changes had to be made in both the JH2 equation of state and the strength model. To assess the potential improvements in respect to the ballistic-penetration resistance of this material brought about by the fused-silica devitrification and permanent-densification processes, a series of transient non-linear dynamics finite element analyses of the transverse impact of a fused-silica test plate with a solid right-circular cylindrical steel projectile was conducted. The results obtained revealed that, provided the projectile incident velocity and, hence, the attendant pressure, is sufficiently high, fused silica can undergo impact-induced devitrification, which improves its ballistic penetration resistance.

1.2 Thesis Outline

Within the present work, three main works regarding the effect of high-pressure on ballistic penetration resistance of glass are addressed: (a) The Effect of High-pressure Densification on Ballistic-penetration Resistance of Soda-lime Glass; (b) all-atom molecular-level analysis of the ballistic-impact-induced densification and devitrification of fused silica; and (c) the effect of high-pressure devitrification and densification on ballistic-penetration resistance of fused silica. These three aspects of the present work are discussed in detail in Chapters 2, 3 and 4, respectively. A summary of the main findings obtained and of the main conclusions reached in the present work is given in Chapter 5. Also, in Chapter 5, a list of suggestions for future work is provided.

1.3 References

1. E. Strassburger, P. Patel, W. McCauley and D. W. Templeton, "*Visualization of Wave Propagation and Impact Damage in a Polycrystalline Transparent Ceramic- AlON,*" Proceedings of the 22nd International Symposium on Ballistics, November 2005, Vancouver, Canada.
2. AMPTIAC Quarterly: *Army Materials Research*: *Transforming Land Combat Through New Technologies,* 8, no.4, 2004.
3. E. Strassburger, P. Patel, J. W. McCauley, C. Kovalchick, K. T. Ramesh and D. W. Templeton, "*High-Speed transmission Shadowgraphic and Dynamic Photoelasticity Study of Stress Wave and Impact Damage Propagation in Transparent Materials and Laminates Using The Edge-on Impact Method,*" Proceedings of the 23rd International Symposium on Ballistics, Spain, April 2007.
4. D. Z. Sun, F. Andreiux, A. Ockewitz, "*Modeling of the Failure Behavior of Windscreens and Component Tests*," 4th LS-DYNA Users' Conference, Bamberg, Germany, 2005.

CHAPTER 2: THE EFFECT OF HIGH-PRESSURE DENSIFICATION ON BALLISTIC PENETRATION RESISTANCE OF SODA-LIME GLASS

2.1 Abstract

Molecular-level modeling and simulations of the high-pressure volumetric response and irreversible densification of a prototypical soda-lime glass are first employed. The molecular-simulation results obtained were next used to modify the pressure vs. degree-of-compression (the negative of volumetric strain) and yield strength vs. pressure relations in order to account for the effects of irreversible densification. These relations are next used to upgrade the Equation of State and the strength constitutive laws of an existing material model for glass. This was followed by a set of transient non-linear dynamics calculations of the transverse impact of a glass test plate with a solid right-circular cylindrical steel projectile. The results obtained show that irreversible densification can provide only a minor improvement in the ballistic resistance of glass and only in the case of high-velocity (ca. 1000m/s) projectiles. Furthermore, it was demonstrated that if through modifications in glass chemistry and microstructure, the key irreversible compaction parameters can be adjusted, significant improvements in the glass ballistic resistance can be attained and over a relatively wide range of projectile velocities.

2.2. Introduction

A public domain literature review carried out as part of the present work revealed that several different materials and design strategies are currently being used in transparent ballistic-impact resistant vehicle structures (e.g. windshields, door windows, viewports, etc.). Among the most recently introduced transparent materials and technologies, the following have received the most attention: transparent crystalline ceramics (e.g. aluminum-oxinitride spinel, AlON, sapphire [1]), new transparent polymer materials (e.g. transparent nylon [2]), and new interlayer technologies (e.g. polyurethane bonding layers [3]), and new laminate structure designs [e.g. 4]. Despite the clear benefits offered by these materials and technologies (e.g. transparent ceramics offer a very attractive combination of high stiffness and high hardness levels, highly ductile transparent polymers provide superior fragment containing capabilities, etc.), ballistic glass remains an important constituent material in a majority of transparent impact resistant structures used today. Among the main reasons for the wide-scale use of glass, the following three are most frequently cited: (a) glass-structure fabrication technologies enable the production of curved, large surface-area, transparent structures with thickness approaching several inches; (b) relatively low material and manufacturing costs; and (c) compositional modifications, chemical strengthening, and controlled crystallization have demonstrated to be capable of significantly improving the ballistic properties of glass [e.g. 2].

The development of new glass-based transparent impact resistant structures aimed at reducing the vulnerability of protected vehicle occupants and on-board instrumentation to various threats typically includes extensive prototyping and laboratory/field testing. These prototyping/testing programs are critical for ensuring the utility and effectiveness of the transparent impact resistant structures. However, the use of prototyping/testing programs is

generally expensive, time-consuming and involves destructive test procedures. While the role of prototyping/testing programs remains critical, they are increasingly being complemented by the corresponding computation-based modeling and simulation efforts. However, the availability of realistic physically-based material models describing deformation/fracture response of ballistic glass under high-deformation-rate/high-pressure loading conditions is one of the key requirements for attaining a high level of utility and fidelity of these computation-based modeling and simulation approaches. Therefore, one of the main objectives of the present work is to further advance the application of computational modeling/simulation-based engineering approaches of transparent impact-resistant structures via improvements in the accuracy of the existing ballistic-glass material models.

A comprehensive literature review carried out as part of the present work revealed that the mechanical behavior of glass is modeled predominantly using three distinct approaches: (a) molecular-modeling methods; (b) continuum-material approximations, and (c) models based on explicit crack representation. A brief overview and the main findings for each of these three approaches are given in the remainder of this section.

2.2.1 Molecular-level Material Modeling

The first molecular-level computational investigation of glass reported in open literature can be traced back to the 1976 work of Woodcock et al [5]. Since that time, major advances in computer technology and the introduction of high-fidelity quantum mechanics based force-fields (inter-atomic potentials) have allowed for more accurate computational modeling of glass elastic constants, strength, chemical and thermal diffusivities, surface energies, etc. Of interest to the present work, a great number of researchers have investigated, using molecular modeling techniques, the propensity of various types of glass (of different chemistries and microstructures) to undergo irreversible (permanent) densification when subjected to high hydrostatic pressures on the order of 10GPa [e.g. 6-8]. The emphasis in these investigations was placed on elucidating the main atomic-level mechanisms and processes (e.g. increased coordination number, often referred to as coordination defects, creation of new metastable chemical bonds, etc.) associated with high pressure irreversible densification of glass. In the present work, on the other hand, molecular-modeling investigations of high-pressure irreversible densification of glass will be carried out in order to assess its effect on the continuum-level pressure vs. degree-of-compression (the negative of volumetric strain) relation, also known as the Equation of State (EOS). In addition, the ability of glass densification to act as a potent energy absorbing process, and thus, as a glass-toughening mechanism is investigated.

2.2.2 Continuum-level Material Modeling

Within the continuum-level glass models [e.g. 9-15], glass is treated as a continuum material whose stiffness and strength properties may become degraded by nucleation, growth, and coalescence of cracks. The fundamental assumption in these models is that the elastic-stiffness and strength degradations are the result of inelastic deformation caused by micron and sub-micron size cracks, and that this degradation can be quantified using a so-called "damage tensor" whose evolution during loading can be formulated using generalized Griffith-type crack initiation and propagation criteria for brittle materials. In addition, some continuum models account for the interactions between the cracks, their coalescence, friction between fragments, competition between micro-cracking leading to fine-scale fragmentation of glass and macro-cracking giving rise to coarse fragmentation, etc. In addition to the physically-based continuum-material models for glass mentioned above, the Johnson Holmquist 2 (commonly referred to as the JH2 model, [16]) is often used to model the behavior of glass under high-loading rate conditions. Despite its phenomenological nature, the JH2 model has been found to often provide a reasonably good account for glass response under these loading conditions. For this reason, the JH2 model will be used in the present work for coupling with the molecular modeling approaches mentioned above. Specifically, the polynomial EOS used to account for the hydrostatic/volumetric response of glass within the JH2 model will be modified to include pressure vs. degree-of-compression results which will be obtained using the aforementioned molecular modeling procedure. In addition, molecular-level results pertaining to irreversible densification-induced strengthening will be used to modify the JH2 strength constitutive law.

2.2.3 Explicit Crack Representation Material Models

Within this material-modeling framework, glass is treated as a linear elastic material, and its fracture is considered to take place via nucleation, propagation and coalescence of discrete (rather than smeared-out/homogenized) cracks during impact [e.g. 17]. In other words, while within the continuum modeling framework the stiffness/strength-degrading effect of smeared-out cracks is included only implicitly, in the explicit crack representation material models cracks are considered as discrete entities and their effect on material stiffness/strength is accounted for explicitly. When the latter-type of glass models are implemented into a finite element computational framework, crack nucleation and propagation are handled by duplicating nodes at the crack tip/front. Adaptive re-meshing is used to provide a rich enough set of possible fracture paths around the crack tip. As a crack grows, forces at newly cracked (free) surfaces are brought to zero in accordance with the Griffith criterion to account for crack growth induced unloading. This enables explicit modeling of the crack coalescence process which can lead to fragment formation. The major disadvantages of the discrete models are that they are extremely computationally expensive and become intractable as the number of cracks increases. That is, in order to capture all possible crack nucleating sites, meshes with micron-size element are ultimately required. Hence, despite the fact that inclusion of high-pressure densification effects may also be beneficial to the discrete glass models, due to their prohibitively high computational costs they will not be considered in the present work.

As demonstrated above, molecular-level, continuum-level and discrete modeling are maturing areas of glass research which are capable of revealing complex intrinsic mechanisms and phenomena associated with deformation and fracture in glass. However, these modeling approaches are typically concerned only with the effect of the observed processes/mechanisms on

the behavior of glass at their respective length scales and practically no reports were found where the knowledge about glass behavior at one length scale was used to improve glass models at other length scale(s). Therefore, the main objectives of the present work are: (a) to investigate and quantify (using molecular-level modeling and simulation techniques) the irreversible densification process in soda-lime glass at high pressures; (b) to determine if modifications in the EOS and the strength constitutive law of the JH2 continuum-material model for soda-lime glass to include the effects of high-pressure irreversible densification obtained in (a) significantly alters the mechanical response of glass under ballistic-loading conditions; and (c) to carry out a preliminary assessment of high-pressure irreversible densification as an energy-absorbing/strength-enhancing mechanism in glass. Toward that end, molecular-level calculations are carried out first to quantify the basic pressure vs. degree-of-compression relation in glass at high-pressure as this material undergoes irreversible densification. Also, molecular-level simple shear tests were carried out to assess the extent of irreversible-densification induced strengthening. The results obtained are next used to modify the JH2 EOS and strength constitutive law for glass. Then, a series of transient non-linear dynamics analyses of transverse impact of a glass test-panel with a solid right-circular cylinder Fragment Simulating Projectile (FSP) is carried out to examine: (a) the extent of change in the temporal and spatial distribution of deformation and damage and (b) the resulting change in ballistic-penetration resistance brought about by the aforementioned modifications in the glass material model.

2.2.4 Chapter Organization

The organization of the paper is as follows: A discussion of the inter-atomic force field potentials, computational cell, and the computational method used in the molecular-level simulations are all presented in Chapters 2.3. Then a brief overview of the JH2 continuum-material model for glass is provided in Chapters 2.4. The main results obtained in the present work (including the definition of a FSP transverse-impact problem for a glass test-panel) are presented and discussed in Chapters 2.5, while the key conclusions resulting from the present study are summarized in Chapters 2.6.

2.3. Molecular-level Modeling of Glass

At the molecular level, soda-lime glass is treated as a discrete material consisting of: (a) silicon (Si) and oxygen (O) atoms mutually bonded via a single covalent bond and forming a connected, non-structured/amorphous network of silica (SiO_4^{4-}) tetrahedra; (b) oxygen anions (O^{2-}) attached as terminal functional-groups to the fragmented silica tetrahedra network; and (c) sodium cations (Na^{+}) dispersed between fragmented silica tetrahedra networks and ionically bonded to the oxygen anions. To fully account for the bonding and non-bonding types of interactions between the atoms/ions listed above one must define the respective interaction-potential functions (commonly referred to as the force-fields), as well as the associated atomic-polar and ionic charges.

While glass is an amorphous material and does not possess any long-range regularity in its atomic/molecular structure, modeling of bulk behavior of glass is typically done at the molecular level by assuming the existence of a larger unit cell. Repetition of this cell in the three orthogonal directions (the process also known as application of the "periodic boundary conditions") results in the formation of an infinitely-large bulk-type material.

Molecular-modeling simulations typically rely on one of the following two techniques: (a) molecular statics, the technique within which the potential energy of the molecular structure in question is minimized with respect to the position of the constituent atoms and ions in the unit cell as well as with respect to the size and shape of the unit cell; and (b) molecular dynamics, a technique within which the Newton's equations of motion are solved for all interacting atoms an ions in the system as a function of time and the appropriate ensemble averages are used to assess/quantify various molecular-level material properties.

The discussion presented above indicates that the three main components of a molecular-level model which must be defined are: (a) the force-fields; (b) the initial unit cell size and shape as well as the initial positions of atoms and ions within it; and (c) the computational procedure to be employed. A brief description of these three components used in the present molecular-level investigation of soda-lime glass behavior under high pressures is presented in the remainder of this chapter.

2.3.1 Force-fields

While accurate simulations of a system of interacting particles (i.e. atoms or ions) generally entail the application of quantum mechanical techniques, such techniques are computationally quite expensive and are usually feasible only in systems containing up to a few hundreds of interacting particles. In addition, the main goal of simulations of the systems containing a large number of particles is generally to obtain the systems' bulk properties which are primarily controlled by the location of atomic nuclei and the knowledge of the electronic structure, provided by the quantum mechanics techniques, is not critical. Under these circumstances, a good insight into the behavior of a system can be obtained if a reasonable, physically-based approximation of the potential (force-field) in which atomic nuclei move is available. Such a force-field can be used to generate a set of system configurations which are statistically consistent with a fully quantum-mechanical description.

As stated above, a crucial point in the molecular-level simulations of multi-particle systems is the choice of the force-fields which describe, in an approximate manner, the potential energy hyper-surface on which the atomic nuclei move. In other words, the knowledge of force-fields enables determination of the potential energy of a system in a given configuration. In general, the potential energy of a system of interacting particles can be expressed as a sum of the valence (or bond), $E_{valence}$, cross-term, $E_{cross\text{-}term}$, and non-bond, $E_{non\text{-}bond}$, interaction energies as:

$$E_{total} = E_{valence} + E_{cross-term} + E_{non-bond} \tag{2-1}$$

The valence energy generally includes a bond stretching term, E_{bond}, a two-bond angle term, E_{angle}, a dihedral bond-torsion term, $E_{torsion}$, an inversion (or an out-of-plane interaction) term, E_{oop}, and a Urey-Bradlay term (which involves interactions between two particles bonded to a common particle), E_{UB}, as:

$$E_{valence} = E_{bond} + E_{angle} + E_{torsion} + E_{oop} + E_{UB} \tag{2-2}$$

A schematic explanation of the first four types of valence atomic interactions is given in Figure 2-1.

The cross-term interacting energy, $E_{cross\text{-}term}$, accounts for the effects such as bond length and angle changes caused by the surrounding atoms and generally includes: stretch-stretch interactions between two adjacent bonds, $E_{bond\text{-}bond}$, stretch-bend interactions between a two-bond angle and one of its bonds, $E_{bond\text{-}angle}$, bend-bend interactions between two valence angles associated with a common vertex particle, $E_{angle\text{-}angle}$, stretch-torsion interactions between a dihedral angle and one of its end bonds, $E_{end\_bond\text{-}torsion}$, stretch-torsion interactions between a dihedral angle and its middle bond, $E_{middle\_bond\text{-}torsion}$, bend-torsion interactions between a dihedral angle and one of its valence angles, $E_{angle\text{-}torsion}$, and bend-bend-torsion interactions between a dihedral angle and its two valence angles, $E_{angle\text{-}angle\text{-}torsion}$, terms as:

$$\begin{aligned} E_{cross-term} = {} & E_{bond-bond} + E_{angle-angle} + E_{bond-angle} + E_{end\_bond-torsion} + E_{middle\_bond-torsion} \\ & + E_{angle-torsion} + E_{angle-angle-torsion} \end{aligned} \tag{2-3}$$

The non-bond interaction term, $E_{non\text{-}bond}$, accounts for the interactions between non-bonded particles and includes the van der Waals energy, E_{vdW}, the Coulomb electrostatic energy, $E_{Coulomb}$, and the hydrogen bond energy, $E_{H\text{-}bond}$, as:

$$E_{non-bond} = E_{vdW} + E_{Coulomb} + E_{H-bond} \tag{2-4}$$

Particle interactions in the soda-lime glass system under investigation are modeled using COMPASS (Condensed-phased Optimized Molecular Potential for Atomistic Simulation Studies), the first ab initio force-field that enables an accurate and simultaneous prediction of various gas-phase and condensed-phase properties of organic and inorganic materials [18,19].

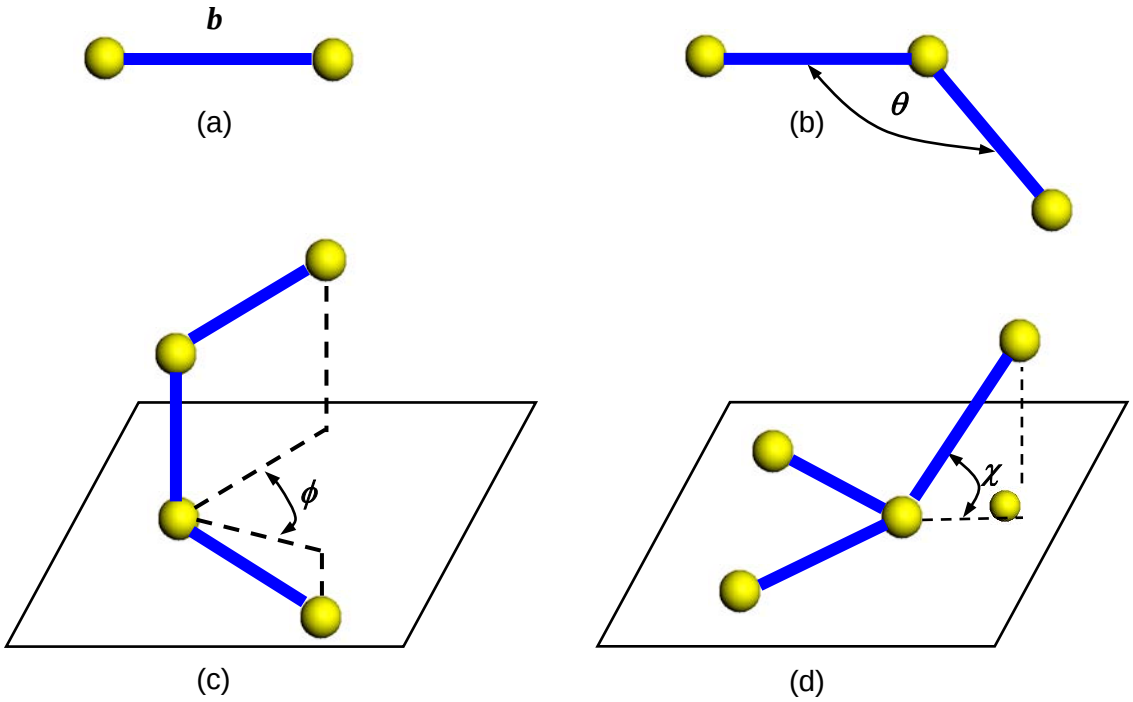

Figure 2-1 A schematic of the: (a) stretch; (b) angle; (c) torsion; and (d) inversion valence atomic interactions.

The COMPASS force-field uses the following expression for various components of the potential energy:

$$E_{bond} = \sum_{b}\left[K_2(b-b_0)^2 + K_3(b-b_0)^3 + K_4(b-b_0)^4\right] \tag{2-5}$$

$$E_{angle} = \sum_{\theta}\left[H_2(\theta-\theta_0)^2 + H_3(\theta-\theta_0)^3 + H_4(\theta-\theta_0)^4\right] \tag{2-6}$$

$$E_{torsion} = \sum_{\phi}\left[V_1\left[1-\cos\left(\phi-\phi_1^0\right)\right]+V_2\left[1-\cos\left(2\phi-\phi_2^0\right)\right]+V_3\left[1-\cos\left(3\phi-\phi_3^0\right)\right]\right] \tag{2-7}$$

$$E_{oop} = \sum_{x} K_x \chi^2 \tag{2-8}$$

$$E_{bond-bond} = \sum_{b}\sum_{b'} F_{bb'}(b-b_0)(b'-b_0') \tag{2-9}$$

$$E_{angle-angle} = \sum_{\theta}\sum_{\theta'} F_{\theta\theta'}(\theta-\theta_0)(\theta'-\theta_0') \tag{2-10}$$

$$E_{bond-angle} = \sum_{b}\sum_{\theta} F_{b\theta}(b-b_0)(\theta-\theta_0) \tag{2-11}$$

$$E_{end\_bond-torsion} = \sum_{b}\sum_{\phi} F_{b\phi}(b-b_0)\left[V_1\cos\phi + V_2\cos 2\phi + V_3\cos 3\phi\right] \tag{2-12}$$

$$E_{middle\_bond-torsion} = \sum_{b'}\sum_{\phi} F_{b'\phi}(b'-b_0')\left[F_1\cos\phi + F_2\cos 2\phi + F_3\cos 3\phi\right] \tag{2-13}$$

$$E_{angle-torsion} = \sum_{\theta}\sum_{\phi} F_{\theta\phi}(\theta-\theta_0)\left[V_1\cos\phi + V_2\cos 2\phi + V_3\cos 3\phi\right] \tag{2-14}$$

$$E_{angle-angle-torsion} = \sum_{\phi}\sum_{\theta}\sum_{\theta'} K_{\phi\theta\theta'}\cos\phi(\theta-\theta_0)(\theta'-\theta_0') \tag{2-15}$$

$$E_{Coulomb} = \sum_{i>j}\frac{q_i q_j}{\varepsilon r_{ij}} \tag{2-16}$$

$$E_{vdW} = \sum_{i>j} \left[\frac{A_{ij}}{r_{ij}^{9}} - \frac{B_{ij}}{r_{ij}^{6}} \right] \tag{2-17}$$

where b and b′ are the bond lengths, θ the two-bond angle, ϕ the dihedral torsion angle, χ the out of plane angle, q the atomic charge, ε the dielectric constant, r_{ij} the i-j atomic separation distance. b_0, K_i (i=2-4), θ_0, H_i (i=2-4), ϕ_i^0 (i=1-3), V_i (i=1-3), $F_{bb'}$, b'_0, $F_{\theta\theta'}$, θ'_0, $F_{b\theta}$, $F_{b\phi}$, $F_{b'\phi}$, F_i (i=1-3), $F_{\theta\phi}$, $K_{\phi\theta\theta'}$, A_{ij}, and B_{ij} are the material-system dependent parameters implemented into Discover [20], the atomic simulation program used in the present work.

2.3.2 Computational Cell

In the molecular-level modeling portion of the work, a 2916 particle computational cell was created with a chemical composition of $(Na_2O)_{0.15}$ $(SiO_2)_{0.85}$. The molecular-level unit cell was constructed with a cubic geometry having a uniform edge-length of 3.347nm. An amorphous cell of sodium silicate glass was thus created with a density of 2.613g/cm^3. The three edges (a, b and c) of the cell were aligned respectively with the three coordinate axes (x, y and z). To create a bulk-material environment for the particles, periodic boundary conditions were applied to all six faces of the unit cell.

To create the initial particle configuration in the unit cell, the Visualizer [21] from Accelrys was first used to construct a short silica-chain fragment. The fragment was then "grown" by a duplicate-and-attach process using the same program. The resulting silica network was next used within the Amorphous Cell program [22] from Accelrys to randomly populate the computational cell while ensuring that the target material density of 2.613g/cm^3 was attained. Lastly, sodium cations were added to obtain an electrically neutral system of particles. An example of a typical molecular-level topology within a single unit cell is displayed in Figure 2-2.

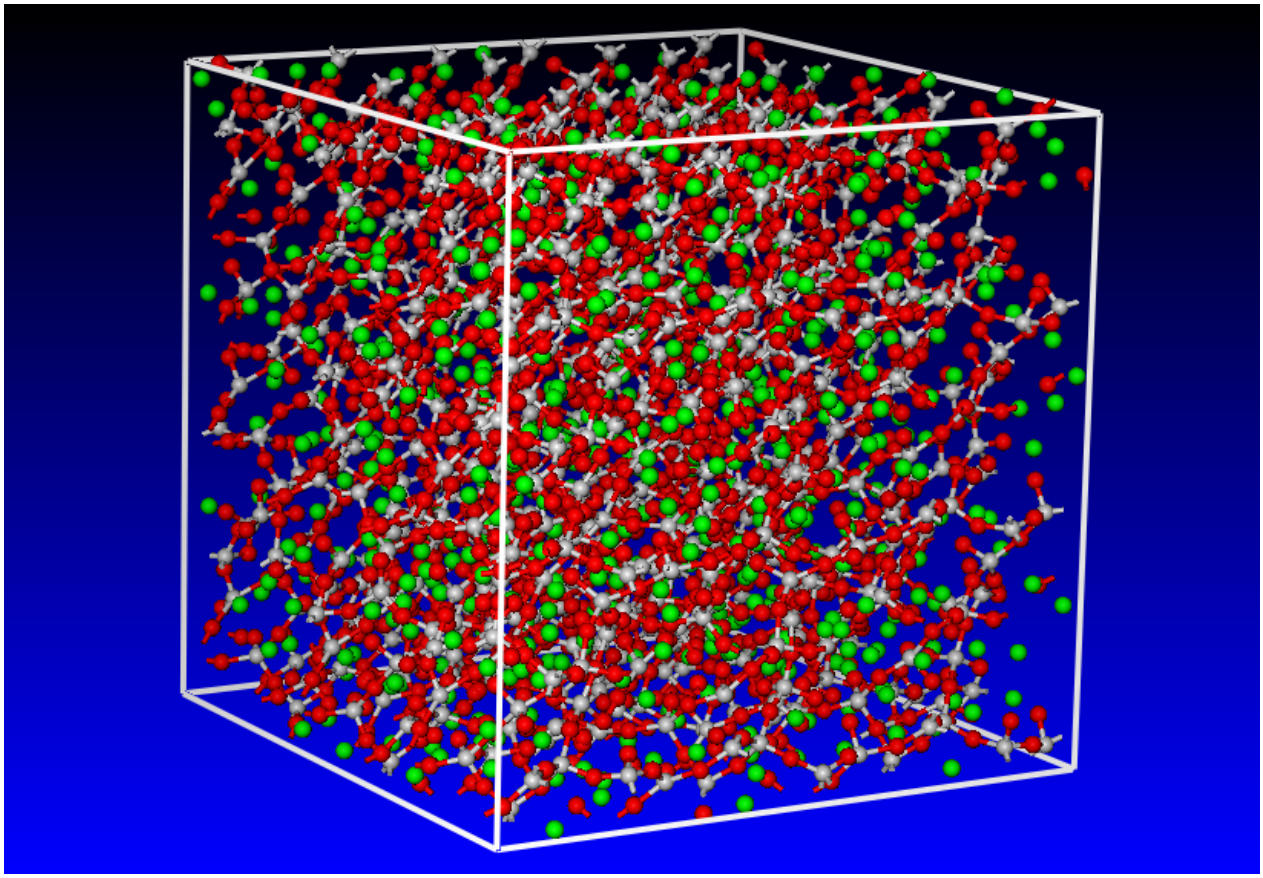

Figure 2-2 The computational unit cell for soda-lime glass molecular-level simulations used in the present work.

2.3.3 Computational Method

High-pressure irreversible densification of glass was studied using a conventional NPT dynamics method within the Discover program [20] from Accelrys, where N (the number of particles), P (pressure), and T (temperature) are the system variables that are held constant or ramped in a controlled manner during compression-simulation runs. The equations of motion were integrated using the velocity Verlet algorithm with a time step of 1.0fs. To comply with typical ballistic-impact loading conditions, pressure was ramped linearly at a rate of 0.3GPa/ps. Pressure ramping was accomplished by 3GPa discrete increments in pressure followed by 10.0ps equilibration times at a given pressure level. Temperature, on the other hand was held constant at a value of 300K using a Nosé Thermostat [23].

At the end of equilibration at each pressure level, the average material density was computed from the corresponding pair-correlation functions. This procedure yielded the sought pressure vs. degree-of-compression relation for the pressurization portion of a loading cycle. To determine the corresponding pressure vs. degree-of-compression relation during the depressurization portion of a loading cycle, pressure was decreased in a similar manner as discussed above. Differences in the pressure vs. degree-of-compression relations for the pressurization and depressurization portions of the loading cycle are then used to quantify the extent of high-pressure irreversible densification of glass.

As will be explained later in more detail, irreversible-densification can affect the ballistic-penetration of glass not only via increased density but also through the associated changes in the material strength. Too assess the extent of densification-induced strengthening,

molecular-level simple-shear tests were carried out. These tests were conducted through the use of a Discover input file which was written in a Basic Tool Command Language (BTCL). This enabled the use of a scripting engine that provides very precise control of simulation runs, e.g. a cell deformation to be carried out in small steps each followed by energy minimization. The minimization portion of the molecular-level simple shear tests was carried out using a combination of three (Steepest Descent, Conjugate Gradient, and Newton's) potential-energy minimization algorithms within Discover [20]. These algorithms are automatically activated/ deactivated as the molecular-level configuration approaches its energy minimum (i.e. the Steepest Descent method is activated at the beginning of the energy-minimization procedure, while the Newton's method is utilized in the last stages of the simulation).

2.4. JH2 Continuum-material Model

To completely define a continuum-level material dynamic model, the relationships between the flow variables (pressure, mass-density, energy-density, temperature, etc.) must be specified. These relations typically involve: (a) an EOS; (b) a strength equation; (c) a failure equation and (d) an erosion equation. These equations arise from the fact that, in general, the total stress tensor can be decomposed into a sum of a hydrostatic stress (pressure) tensor (which causes a change in the volume/density of the material) and a deviatoric stress tensor (which is responsible for the shape change of the material). An EOS then is used to define the corresponding functional relationship between pressure, mass density (degree-of-compression) and internal energy density (temperature). Likewise, a strength relation is used to define the appropriate equivalent plastic strain, equivalent plastic strain rate, and temperature dependencies of the materials yield strength. This relation, in conjunction with the appropriate yield-criterion and flow-rule relations, is used to compute the deviatoric part of stress under elastic-plastic loading conditions. In addition, a material model generally includes a failure criterion (i.e. an equation describing the hydrostatic or deviatoric stress and/or strain condition(s) which, when attained, cause the material to fracture and lose its ability to support, abruptly in the case of brittle materials or gradually in the case of ductile materials, normal and shear stresses). Such failure criterion in combination with the corresponding material-property degradation and the flow-rule relations governs the evolution of stress during failure. The erosion equation is generally intended for eliminating numerical difficulties arising from highly distorted Lagrange cells. Nevertheless, the erosion equation is often used to provide additional material failure mechanisms especially in materials with limited ductility.

To summarize, the EOS along with the strength and failure equations (as well as with the equations governing the onset of plastic deformation and failure and the plasticity and failure induced material flow) enable assessment of the evolution of the complete stress tensor during a transient non-linear dynamics analysis. Such an assessment is needed in order to solve the governing (mass, momentum and energy) conservation equations. It is important to note that separate evaluations of the pressure and the deviatoric stress enable inclusion of the nonlinear effects in the EOS. Generally these effects are shock related but, in the present work, they will be, at least partly, attributed to the phenomenon of high-pressure irreversible densification.

In the present work, glass was modeled using the JH2 brittle-material model [25,26]. The JH2 model is a phenomenological model which postulates the existence of two terminal glass states: (a) an intact material; and (b) a failed material. The two material states are weighted by a single scalar variable called damage, D, whose evolution is governed by an inelastic (plasticity-like deformation model). The JH2 model includes a polynomial-type EOS, a strength model (based on the von Mises yield criterion, normality flow rule and a pressure and strain-rate hardening constitutive relation), a progressive failure model, and an instantaneous geometric strain-based erosion criterion. The values of all the JH2 material-model parameters for soda-lime float glass are available in the ANSYS/Autodyn materials library [24]. Further details of the JH2 model for brittle materials are provided in the remainder of this section.

2.4.1 Polynomial Equation of State

Within the JH2 polynomial EOS, the effect of internal-energy density is neglected and the pressure vs. degree-of-compression in a damage-free material is defined as:

$$P = K_1\mu + K_2\mu^2 + K_3\mu^3, \quad \mu > 0 \quad (\textit{hydrostatic compression}) \tag{2-18}$$

and

$$P = K_1\mu, \quad \mu < 0 \quad (\textit{hydrostatic tension}) \tag{2-19}$$

Where degree-of-compression is $\mu = (\rho/\rho_0 - 1)$ and ρ is the current density, while ρ_0 (the reference density), K_1 (the bulk modulus), K_2 and K_3 are material specific constants.

After glass has begun to accumulate damage (i.e. when the extent of damage is no longer zero, D>0), Eq. (18) has to be upgraded to include the effect of bulking. Bulking is a phenomenon associated with the fact that fragments of fractured materials are not generally fully conformable and, consequently fractured material is associated with a larger volume (a lower density at a constant pressure) than the damage-free material. The bulking modified polynomial EOS is then given by [24]:

$$P = K_1\mu + K_2\mu^2 + K_3\mu^3 + \Delta P, \quad \mu > 0 \tag{2-20}$$

where the bulking-induced pressure increment, ΔP, is determined from energy considerations and varies from zero at D=0 to ΔP_{max} at D=1.0. Assuming that a fraction of the internal elastic energy decrease (due to decrease in deviatoric stresses in the material) is converted to an increase in potential internal energy, the bulking induced pressure increment ΔP at a time $t+\Delta t$ can be represented in terms of ΔP at the time t as:

$$\Delta P(t+\Delta t) = -K\mu(t+\Delta t) + \sqrt{(K_1\mu(t+\Delta t) + \Delta P(t))^2 + 2\beta K_1 \Delta U}, \quad \mu(t+\Delta t) \tag{2-21}$$

where ΔU is the decrease in deviatoric elastic energy due to damage induced yield-strength reduction and β is the fraction of the deviatoric elastic energy converted to hydrostatic potential/elastic energy. The decrease in deviatoric elastic energy is given by:

$$\Delta U = U_t - U_{t+\Delta t} \tag{2-22}$$

where

$$U_t = \frac{\sigma_t^2}{6G} \tag{2-23}$$

The parameters σ_t and G appearing in Eq. (23) are the actual yield strength and the damage-free shear modulus of the glass material, respectively.

2.4.2 Strength Model

Within the JH2 strength model [25,26], the normalized yield strength is defined as a damage-weighted rule of mixtures of the corresponding damage-free and fractured yield strengths as:

$$\sigma^* = \sigma_i^* - D(\sigma_i^* - \sigma_f^*) \tag{2-24}$$

where subscripts i and f are used to denote intact and fractured material states and the superscript * indicates that the corresponding yield strength is normalized by the Hugoniot Elastic Limit (HEL) (uni-axial stress) yield strength, i.e. :

$$\sigma^* = \frac{\sigma}{\sigma_{HEL}} \tag{2-25}$$

The normalized yield strengths σ_i^* and σ_f^* are also defined in the same manner as σ^*. The normalized (pressure and strain rate dependent, ideal-plastic) yield strength of the damage-free material, σ_i^*, and the fractured material, σ_f^*, are respectively given by:

$$\sigma_i^* = A(P^* + T^*)^N (1 + C \ln \dot{\varepsilon}^*) \tag{2-26}$$

$$\sigma_f^* = B(P^*)^M (1 + C \ln \dot{\varepsilon}^*) \tag{2-27}$$

where A, B, C, M, N and σ_{HEL} appearing in Eqs. (25)-(27) are all material specific constants while P^* and T^* are respectively defined as:

$$P^* = \frac{P}{P_{HEL}} \tag{2-28}$$

and

$$T^* = \frac{T}{P_{HEL}} \tag{2-29}$$

where P and T are the actual pressure and the maximum hydrostatic tensile pressure that the glass material can withstand, respectively, and P_{HEL} is the pressure at the Hugoniot Elastic Limit. A schematic of the JH2 strength model in the normalized yield strength vs. normalized pressure plane is displayed in Figure 2-3.

As shown in Ref. [26] P_{HEL} and σ_{HEL} are related to the (uni-directional shockwave-based) uniaxial-strain compressive strength, HEL, as: $HEL = P_{HEL} + \frac{2}{3}\sigma_{HEL}$. Since both P_{HEL} and σ_{HEL} are dependent on the compression ratio at the HEL, both of these parameters can be determined from HEL. Finally, the dimensionless material strain rate, $\dot{\varepsilon}^*$, appearing in Eqs. (28) and (29) is defined as:

$$\dot{\varepsilon}^* = \frac{\dot{\varepsilon}}{\dot{\varepsilon}_0} \tag{2-30}$$

where $\dot{\varepsilon}$ is the actual strain rate and $\dot{\varepsilon}_0$ is the reference strain rate (typically set to 1.0 s^{-1}).

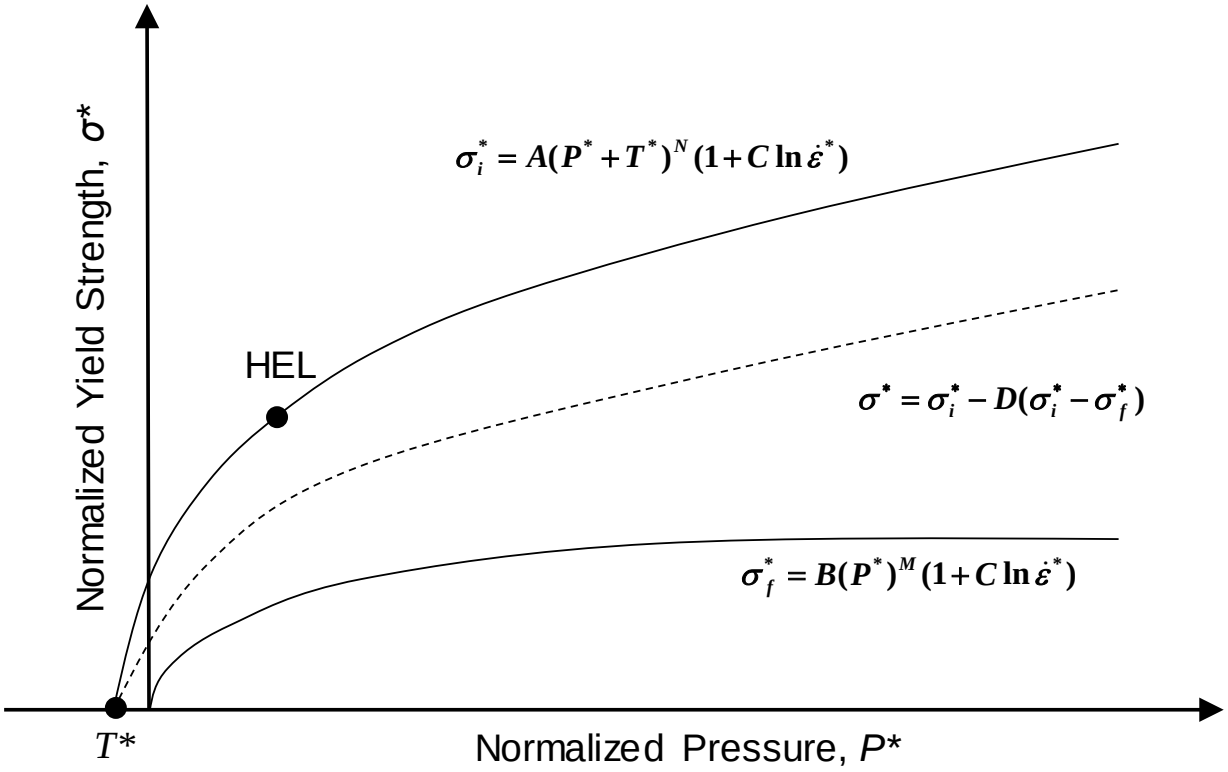

Figure 2-3 A schematic of the JH2 strength model in the normalized yield strength, σ^*, vs. normalized pressure, P^*, plane.

2.4.3 Failure Model

Within the JH2 failure model [25,26], the evolution/accumulation of damage is defined as

$$D = \sum \frac{\Delta \varepsilon_p}{\varepsilon_p^f} \tag{2-31}$$

where $\Delta\varepsilon_p$ is the increment in equivalent plastic strain with an increment in loading and the failure strain ε^f_p is a pressure dependent equivalent fracture strain which is defined as:

$$\varepsilon_p^f = D_1 (P^* + T^*)^{D2} \tag{2-32}$$

where D_1 and D_2 are material specific constants.

Within the JH2 failure model, fracture occurs when either damage reaches a critical value of 1.0 or when negative pressure reaches a value of T. Fracture material has no ability to support any negative pressure, while its ability to support shear is defined by Eq. (27).

2.4.4 Erosion Model

Within the finite-element computational framework, numerical difficulties may arise from excessive distortion of the elements. To overcome these difficulties, an erosion algorithm, which at a predefined level of strain removes the excessively distorted elements while transferring the momentum associated with the removed nodes to the remaining nodes. Following our prior work [27], the erosion criterion is defined by prescribing a critical value for the instantaneous geometrical equivalent strain.

2.5. Results and Discussion

2.5.1 Molecular-level Analysis of High-pressure Densification of Glass

In this section, a brief summary of the molecular-level calculations of glass response to high pressure is provided. While this portion of the work yielded numerous results, only the ones directly related to the potential role of high-pressure irreversible densification in improving impact/penetration resistance of glass are presented and discussed in greater detail. Other results are discussed only qualitatively.

Molecular-level Topology

A detailed examination of the molecular-level topology after subjecting the unit-cell to high pressures revealed distinct differences depending on whether the maximum pressure was below or above ca. 4GPa.

Pressures below ~4GPa: Molecular modeling of glass pressurization/depressurization revealed that when glass is exposed to pressures not exceeding ca. 4GPa, no detectable irreversible changes generally take place in its molecular topology. Closer examination of the atomic structure at different pressure levels between 0GPa and 4GPa revealed:

(a) The presence of "active regions" within which atoms may occasionally undergo large displacements/jumps (ca. 0.1nm). These atomic displacements (the results not shown for brevity) were found to involve coordinated motion of at least a dozen atoms and to be accompanied by abrupt changes in the average potential energy;

(b) In most cases, atomic rearrangement described in (a) appears to be associated with low-frequency transition of the active regions between two distinct "equilibrium" states (of comparable potential energy). These findings are in complete agreement with those found by

Trachenko and Dove [7] which termed this phenomenon as Double Well Potential (DWP) and the associated low-frequency transition/vibrational mode as the “floppy mode”; and

(c) While pressurization up to 4GPa did not yield any permanent changes in the molecular topology, the locations of the active regions were found to change with pressure. That is, the regions active at one pressure level may become inactive at another pressure level while, at the same time other previously inactive regions would become active.

Pressures above ~4GPa: When the computational cell is subjected to pressure exceeding ca. 4GPa and subsequently depressurized to zero pressure, permanent changes in the glass molecular topology were normally observed. These molecular topology changes were accompanied by a permanent density increase on the order of 3–7%. An example of typical results obtained in this portion of the work is given in Figures 2-4(a)-(d), where oxygen atoms/anions are displayed in red and silicon atoms are shown in gray (as well green, pink and yellow highlighting), while sodium cations are omitted for clarity. To aid in visualization/interpretation of the topological changes experienced by glass during high pressure loading/unloading cycles, only a 30-40 atom exemplary region of computational cell was monitored in Figures 2-4(a)-(d). The molecular level topologies displayed in these figures pertain respectively to: (a) high-pressure state, Figure 2-4(a); (b) high pressure state after a prolonged (20ps) relaxation period, Figure 2-4(b); (c) ambient pressure state resulting from depressurization of state (a), Figure 2-4(c); and (d) ambient pressure state resulting from depressurization of state (b), Figure 2-4(d). It should be noted that the results displayed in Figure 2-4(c) are essentially identical to those in the initial configuration prior to loading. A closer examination of the molecular-level topology results displayed in these figures revealed that:

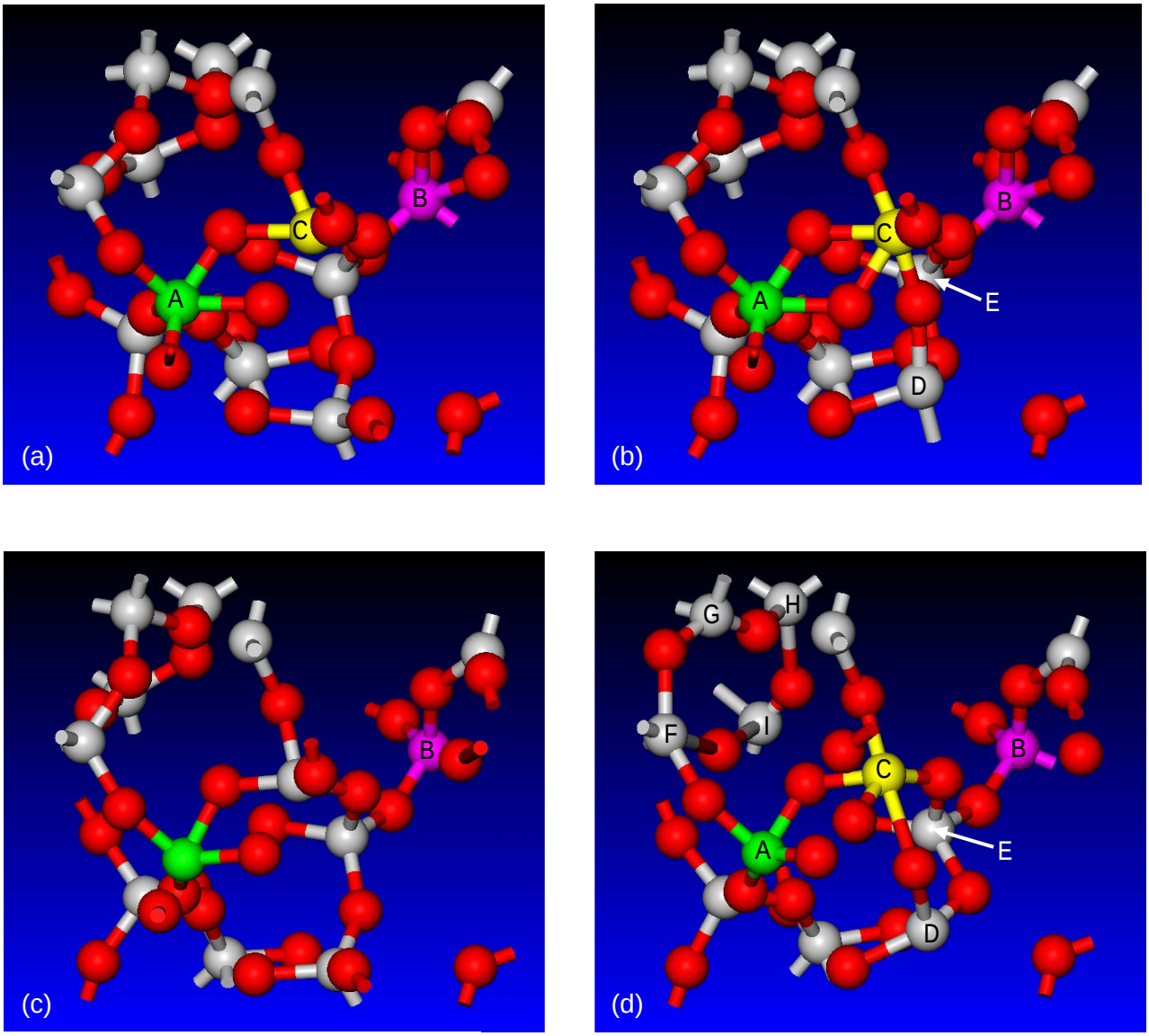

Figure 2-4 The molecular level topologies pertaining to: (a) high-pressure state; (b) high pressure state after a prolonged (20ps) relaxation period; (c) ambient pressure state resulting from depressurization of state (a); and (d) ambient pressure state resulting from depressurization of state (b). See text for explanation.

(a) Pressurization alters not only molecular-level topology, but also changes the bonding structure and increases the average coordination number (of mainly Si atoms). This can be seen by comparing the results displayed in Figures 2-4(a) and (c). It should be noted here, that the results displayed in Figure 2-4(c) are used in place of the initial molecular-level topology results. In these figures, it is seen that silicon atoms labeled A and B change their fourfold coordination to fivefold coordination upon pressurization.

(b) As implied earlier, if the depressurization is carried out without allowing the material to relax at high pressures, the molecular level configuration obtained at the ambient pressure is effectively identical to the initial configuration, Figure 2-4(c). Thus, in the resultant ambient-pressure configuration, most silicon atoms regain their fourfold coordination;

(c) Increased duration of the exposure of glass to high pressure, results in continued changes in the molecular-level topology and bond structure. This can be seen by comparing the results displayed in Figures 2-4(a) and (b). These figures show that relaxation of glass leads to the C-label silicon atom acquiring a fivefold coordination while, at the same time smaller size Si-O rings are being formed. For example, a twofold ring is formed involving the A and C silicon atoms, while a threefold ring involving the C, D and E-labeled Si atoms also appears, Figure 2-4(b). These changes in the molecular-level topology of glass are a manifestation of its relaxation to a material state that is energetically-preferred at high pressures; and

(d) Upon depressurization of glass which was relaxed at high pressures, some changes in the molecular-level topology and the bonding structure are observed. However, the initial material state is not restored. That is, the material has undergone permanent changes in its molecular level topology, bond structure, and density. This can be seen by comparing results displayed in Figures 2-4(c) and (d). These figures show that while A and B-label silicon atoms

regain their fourfold coordination upon depressurization to ambient pressure, the C-labeled silicon atom retains its fivefold coordination, Figures 2-4(b) and (d). Thus, the average coordination number of silicon atoms in the relaxed-then-depressurized state, Figure 2-4(d), is higher than that in the initial configuration, Figure 2-4(c). Furthermore, while the aforementioned twofold Si-O ring was broken upon depressurization, the threefold ring involving the C, D and E-labeled silicon atoms survived this process. In addition, a new fourfold ring involving the Si atoms labeled F, G, H and I was formed. The threefold and fourfold rings were not present in the initial molecular-level configuration, Figure 2-4(c).

Pressure vs. Degree-of-compression Relation

An example of the typical pressure, P vs. degree-of-compression, μ results obtained in the present molecular-level analysis of high-pressure irreversible densification of glass is displayed in Figure 2-5. The results in Figure 2-5 show four loading pressurization/depressurization cycles. The first cycle does not result in any irreversible densification of glass since the maximum pressure attained is not high enough. The second and third cycles yield irreversible densification and reveal that this process is associated with a nearly constant ca. 4GPa pressure level. During the last cycle, irreversible densification is completed so that glass behaves as a perfectly elastic material when subjected to any further loading.

To summarize, the examination of the results displayed in Figure 2-5 revealed the following three important findings: (a) irreversible densification begins at a pressure level of ~4GPa and proceeds to full densification at a nominally constant pressure; (b) irreversible densification is associated with a density increase of ca. 5%; and (c) the average rate of change of pressure with density (which scales with the material bulk modulus) is not significantly different (and will be assumed equal) in the pre- and post-densification glass states.

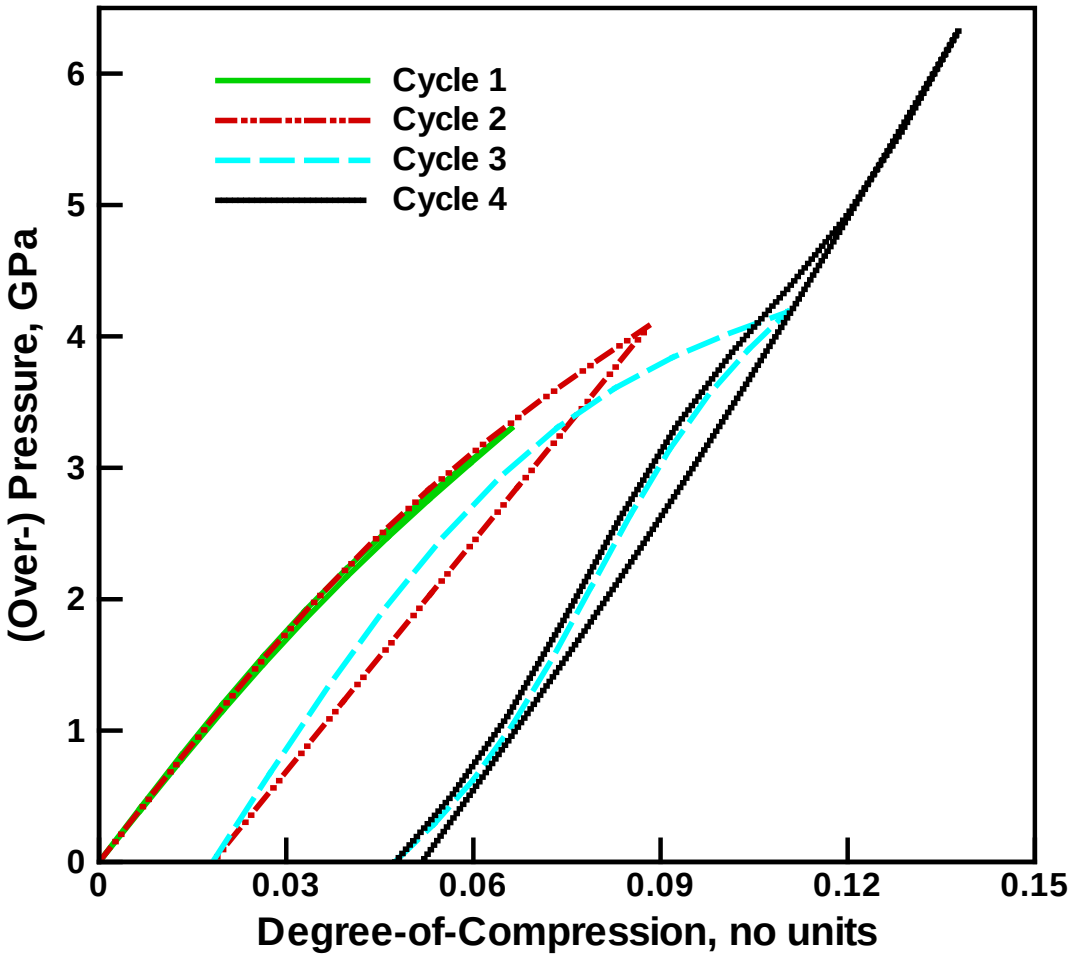

Figure 2-5 Typical pressure vs. degree-of-compression results obtained in the present molecular-level analysis of repeated pressurization/depressurization simulations. In each loading cycle, pressurization was carried out to a higher peak pressure followed by a complete depressurization (i.e. to the atmospheric pressure).

It should be noted that the aforementioned findings (a) and (c) were found not to be very sensitive to the random selection of the initial molecular-level configuration of glass. On the other hand, the extent of irreversible densification was found to vary in a 3-7% range depending on the choice of this configuration.

Densification-induced Material Strengthening

As mentioned earlier, molecular level simple-shear tests were carried out in order to assess the extent of irreversible-densification induced strengthening of glass. Toward that end, shearing of the computational cell was carried out in small increments followed by energy minimization with respect to the atomic positions. An example of the typical molecular-level topology evolution accompanying these tests is displayed in Figures 2-6(a)-(d). To help prevent the computational crystal from settling into a nearby metastable higher-energy configuration, a 10,000-step 300K NVT molecular dynamics (equilibration) run was introduced between the cell shearing and the energy minimization steps. This procedure yielded a plot of the potential energy increase (relative to that in the initial optimized computational cell) versus the shear angle of the computational cell. The shear angle gradient of the potential energy increase divided by the constant unit cell volume is then used to define the material shear strength. This procedure revealed that the shear strength of glass in the irreversibly-compacted state is higher by a factor of ca. 1.5 relative to the strength of glass in the initial state.

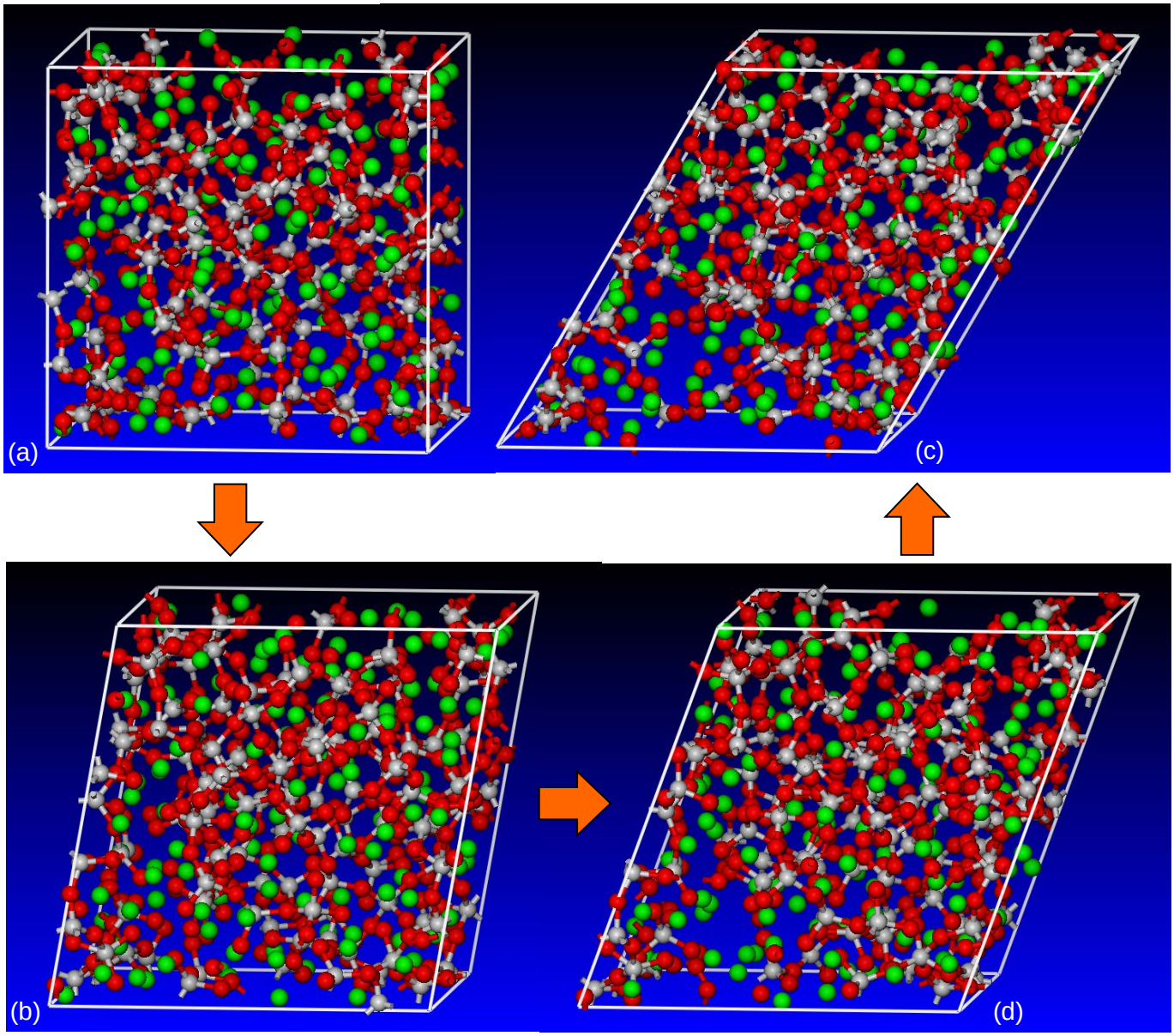

Figure 2-6 An example of molecular-level topology evolution accompanying simple-shear mechanical tests. The tests were used to assess the extent of irreversible-densification induced strengthening of glass.

2.5.2 JH2 Equation of State and Strength-model Modifications

The molecular-level modeling results attained in the previous section were used to modify the original JH2 EOS and the strength model (as presented in Section III). A brief description of these modifications is given in the remainder of this section.

Modifications to the Equation of State

An examination of the polynomial EOS for glass as implemented in the ANSYS/Autodyn material library revealed that the extent of non-linearity is quite small, and hence, the P vs. μ relationship was simplified using a linear EOS. In accordance with the results obtained in the previous section, the following additional simplifications/assumptions were made: (a) the bulk modulus was assumed to take the same (constant) value in both the initial and compacted state of glass, as well as in all intermediate glass states; and (b) irreversible densification of glass is assumed to take place at a constant level of pressure. In accordance with the molecular-level computational results presented in the previous section, this level of pressure was set to a value of 4GPa.

A schematic of the changes made in the P vs. μ relationship is given in Figure 2-7. The aforementioned modifications in the JH2 EOS were implemented in the "MDEOS_USER_1.f90" material user subroutine which is then linked with ANSYS/Autodyn object code to form a new executable.

Modifications of the Strength Model

Irreversible densification of glass is assumed to increase its strength, both in the damage-free and the fractured states. This assumption is based on the following argument: in the case of the damage-free glass state, irreversible densification is assumed to repair molecular-level void-like regions. In the case of the fractured glass state, irreversible densification is assumed to act as

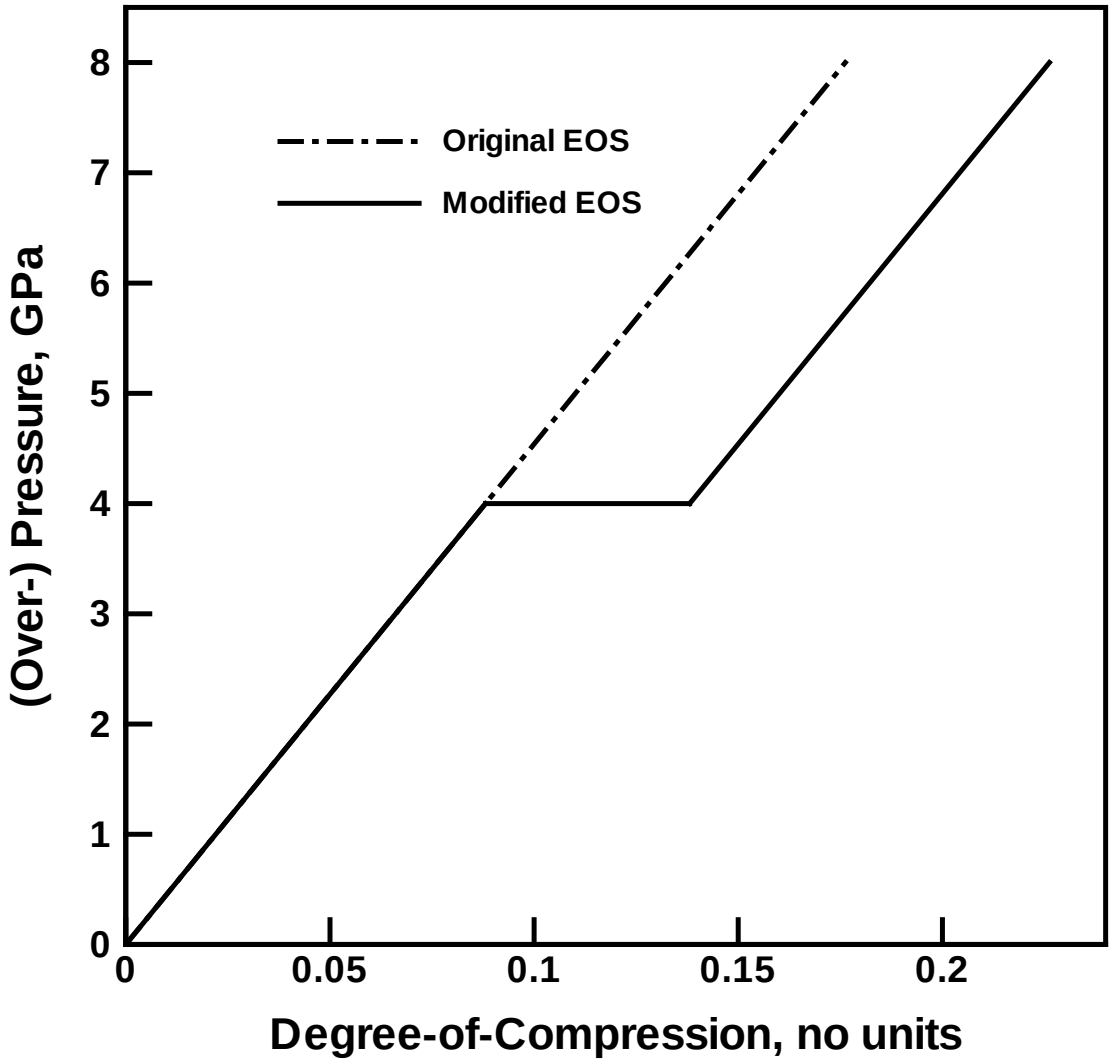

Figure 2-7 A schematic the modifications made in the JH2 (Over-pressure, *P* vs. Degree-of-Compression, μ) Equation of State in order to account for the effect of high-pressure irreversible densification.

a potent fragment-deformation mechanism resulting in mutually more-conformal fragments. The resulting increase in inter-fragment contact surface areas would then give rise to an increase in the friction-controlled strength of fractured glass. An examination of Eqs. (26)-(27) revealed that the parameters A and B control glass strength in the two states, respectively. Following the aforementioned molecular-level findings regarding densification-induced strengthening of the glass, parameters A and B are increased by a factor of 1.5 for the fully densified glass material. At the intermediate levels of glass densification, parameters A and B are assumed to be linearly related to the degree of irreversible densification. The aforementioned modifications in the JH2 strength model were implemented in the "MDSTR_USER_1.f90" material user subroutine which is then linked with ANSYS/Autodyn object code to form a new executable.

2.5.3 Effect of High-pressure Irreversible-densification on Ballistic-impact Resistance of Glass

In the previous section, the molecular-level computational results regarding high-pressure irreversible-densification of glass were used to modify the EOS and the strength relations within the JH2 continuum model for this material. In this section, a simple transverse impact of a monolithic glass plate by a solid right-circular cylinder (FSP) is analyzed computationally in order to assess if the aforementioned modifications in the JH2 model have any significant effect on the temporal evolution and spatial distribution of damage within the glass plate during impact and on the overall glass-plate penetration resistance.

Problem Formulation

A schematic of a circular disk-shaped glass-plate (25.0mm-thick, 75.0mm-radius) impacted by an FSP (12.7mm-diameter, 12.7mm-length) problem is provided in Figure 2-8(a). Due to the attendant symmetry of the problem, an axisymmetric 2-D formulation was employed. An example of the finite-element mesh based on the first-order four-node finite elements is displayed in Figure 2-8(b). It is seen that a finer mesh is used in the FSP and in the region of the glass plate which is most-severely affected during impact/penetration of the plate by the FSP.

The FSP is assumed to be made of AISI/SAE 4340 steel and this material is modeled using a linear EOS, the Johnson-Cook strength model, the Johnson-Cook failure model and an erosion model based on the equivalent geometrical (i.e. elastic + plastic + crack) instantaneous strain. The details regarding formulation and parameterization of this model can be found in our previous work [28].

All the calculations carried out in the present work were done using ANSYS/Autodyn, a general purpose non-linear dynamics modeling and simulation software [24]. A transient non-linear dynamics problem is analyzed within ANSYS/Autodyn by solving simultaneously the governing partial differential equations for the conservation of momentum, mass and energy

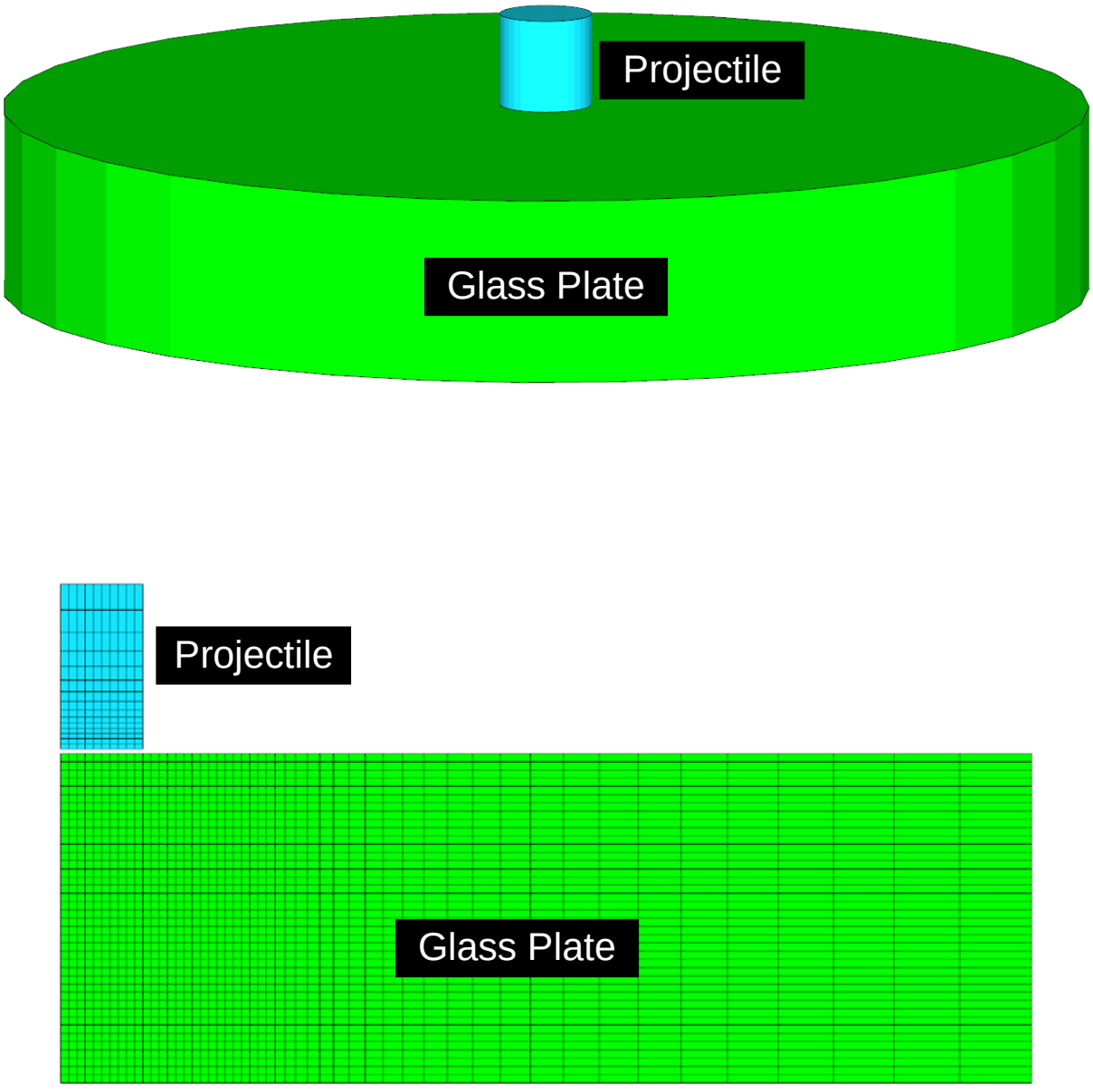

Figure 2-8 (a) A schematic of the glass plate impacted by a right-circular solid cylindrical projectile; and (b) an example of the computational mesh, based on the first-order four-node finite elements, used to model the projectile and the glass plate.

along with the material-model equations and the equations defining the initial and the boundary conditions. The equations mentioned above are solved numerically using a second-order accurate explicit scheme and one of the two (Lagrange or Euler) basic mathematical approaches/processors. The key difference between the two processors is that within the Lagrange processor the numerical grid is attached to and moves along with the material during calculation while within the Euler processor, the numerical grid is fixed in space and the material moves through it. In the present work, both the FSP and the glass plate are modeled using the Lagrange processor. In our recent work [28], a brief discussion was given of how the governing differential equations and the material-model relations define a self-consistent system of equations for the dependent variables (nodal displacements, nodal velocities, material-element densities and material-element internal energy densities). In the same reference, a brief overview was provided of the contact/interaction and erosion algorithms implemented in ANSYS/Autodyn.

The initial conditions are defined is such a way that the FSP is assigned a downward velocity while the glass plate is assumed to be stationary. To reduce the effect of reflection of the shock waves at the (outer) hoop surface of the glass plate, the so called "transmit" boundary conditions were applied to all the nodes residing on this surface. The transmit boundary conditions enable propagation of the stress waves across the hoop surface without reflection [28].

Glass-plate Impact Computational Results

An example of the results pertaining to the temporal evolution and spatial distribution of deformation and damage within the glass-plate and the FSP is displayed in Figures 2-9(a)-(d). Various deformation/failure models are color coded to improve clarity of the results. The results displayed in Figures 2-9(a)-(d) show that shear-induced damage/failure is found mainly in the region underneath the FSP, tensile failure occurs at the glass-plate back-face (and is caused by reflection of the compressive stress wave at this face), and the FSP undergoes extensive plastic

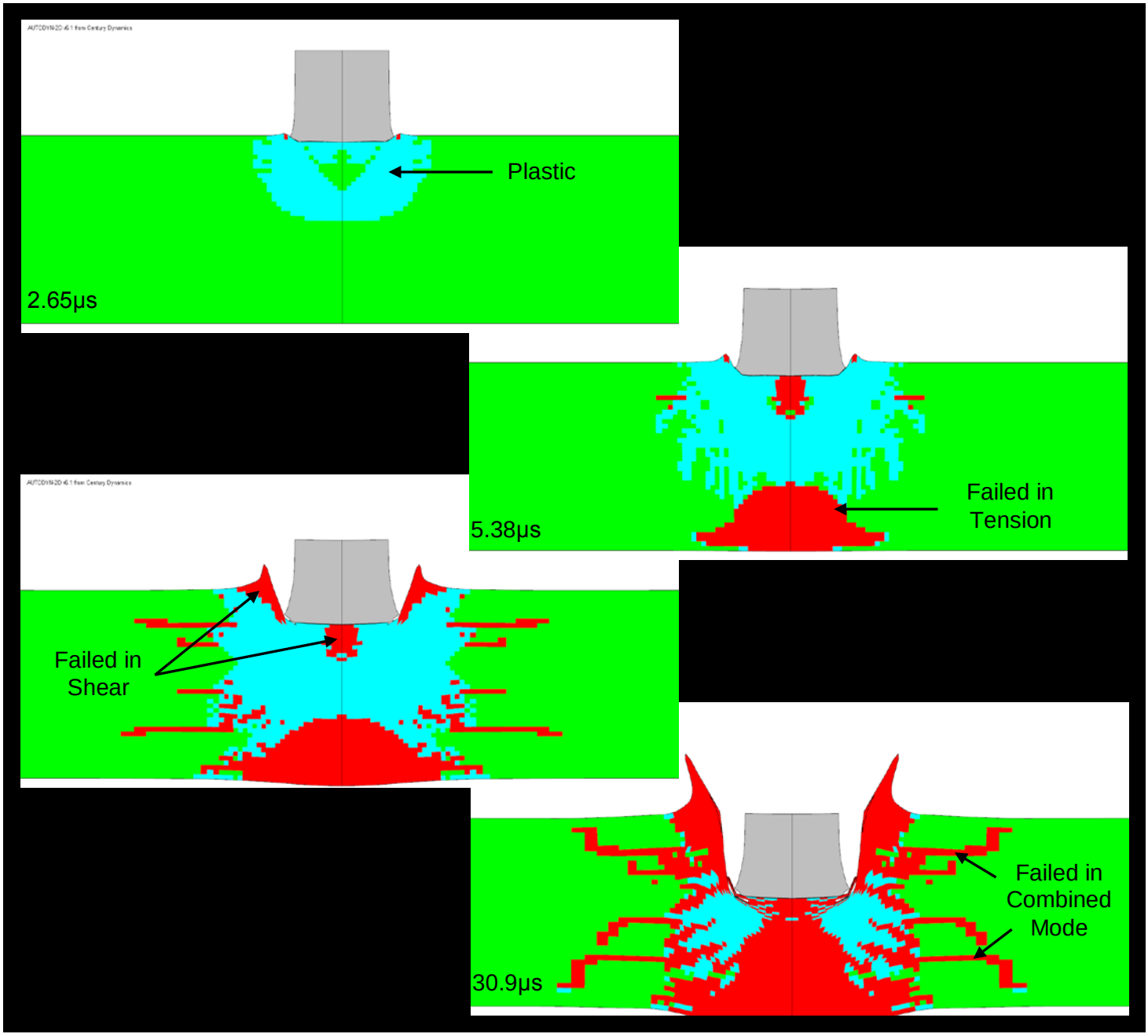

Figure 2-9 An example of the results pertaining to the temporal evolution and spatial distribution of deformation and damage within the glass-plate and the FSP.

deformation (but little or no failure). These findings are fairly common and, hence, will not be discussed any further. It should be noted, however, that the results displayed in Figures 2-9(a)-(d) pertain to an initial FSP velocity of 600m/s and the original (unmodified) JH2 glass-material model.

When the JH2 material model was modified to include the effect of high-pressure irreversible-densification and the FSP initial velocity was maintained at 600m/s, an identical temporal evolution and spatial distribution of the material deformation and failure was found as those in Figures 9(a)-(d). This finding was readily rationalized by establishing that the pressure within the glass-plate never reached the level of 4GPa required for the irreversible-densification to commence.

When the FSP velocity was increased to 1000m/s, the effect of irreversible-densification was observed. An example of this effect is given in Figures 10(a)-(b), in which distribution of deformation and damage within the glass-plate and the FSP are given for the cases of original and modified JH2 glass material models, respectively. The results displayed in these figures show that the extent of damage in the FSP increased, while the extent of damage in the glass-plate is reduced for the case of the modified JH2 material model. Also, the FSP exit velocity was found to be reduced from 469.1m/s to 460.2m/s as a result of glass material model modifications. This is a relatively small decrease (ca. 2%) in the FSP residual velocity which may suggest that the irreversible compaction of glass may not be a potent ballistic-resistance enhancing mechanism in glass.

To further explore the effect of irreversible densification, a parametric study was set up in which the key parameters of this process were varied within physically realistic limits. Specifically, the pressure at which densification starts was varied in a range 1-10GPa range,

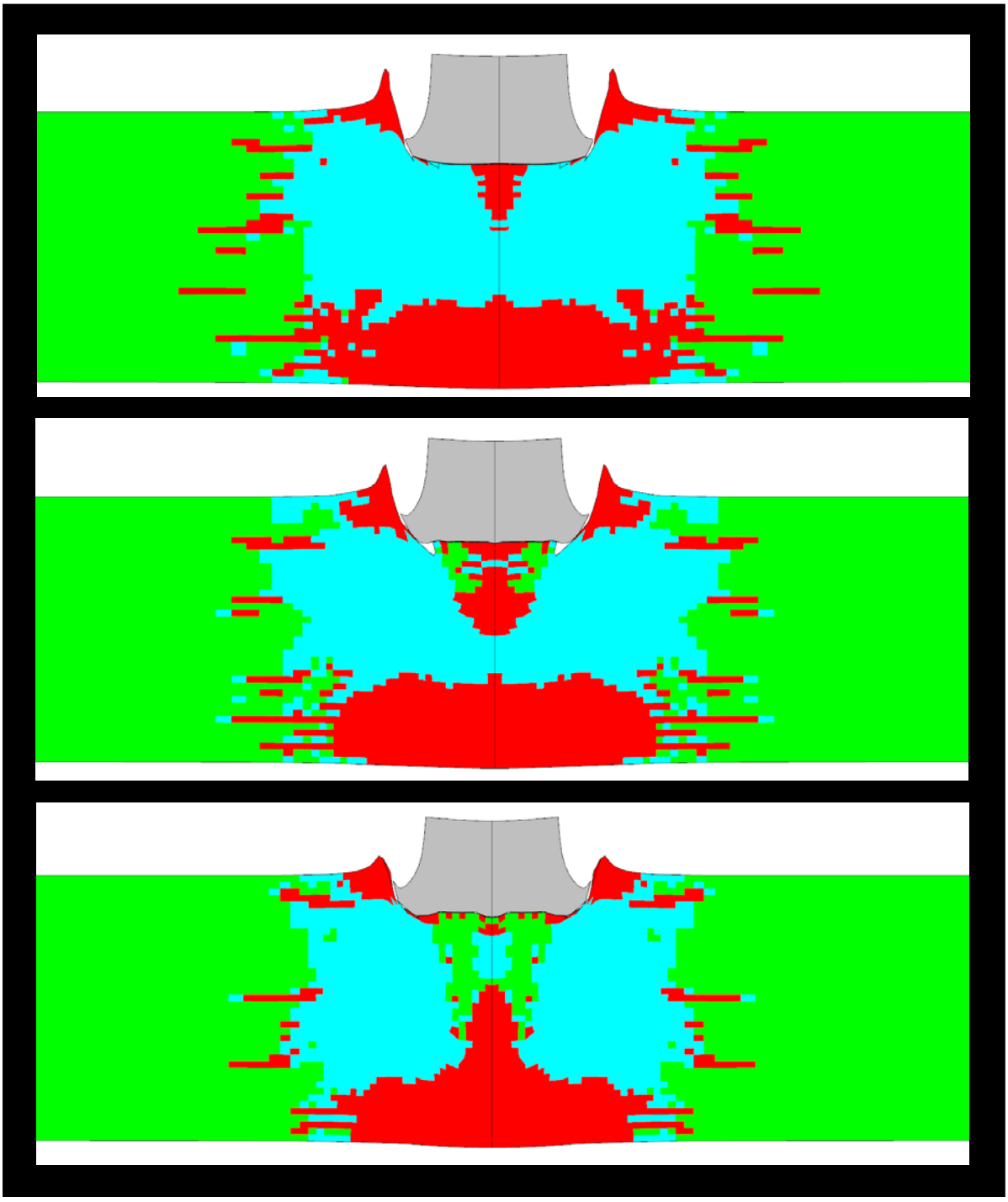

Figure 2-10 The effect of the JH2 material-model modifications on the spatial distribution of damage within a soda-lime glass plate impacted with a 12.7mm-diameter/ 12.7mm-height right circular solid cylinder at an initial velocity of 1000m/s: (a) the original model; (b) the model modified using molecular-level finding; and (c) the modified using an optimal set of high-pressure irreversible-densification parameters.

density increase between 5 and 15% and the densification-induced strengthening extent (i.e. the multiplier of ***A*** and ***B*** parameters) in a 1.0-2.0 range. This study revealed that, at an FSP velocity of 1000m/s, the FSP exit velocity can be reduced from 469.1m/s to 346.4m/s (a 26% reduction). The optimal set of irreversible-densification parameters was identified as: densification pressure 1GPa, density increase 5% and a strengthening extent of 2.0. Figure 10(c) reveals spatial distribution of deformation/damage for the modified JH2 glass model and the optimal set of irreversible densification parameters. It is seen that there is a significant reduction in damage to the glass material directly under the projectile due to the increased strength of the densified glass. This reduction in failed material under the projectile promotes an increase in the extent of plastic deformation experienced by the projectile which leads to spreading of its material over a larger area. These observed effects combine to allow for a significant decrease in the kinetic energy of the projectile with respect to the non-optimized glass material case.

Additional simulations were next carried out in order to establish if irreversible-compaction of glass (if associated with the aforementioned optimal set of parameters) can improve the ballistic-resistance of glass at lower FSP velocities. It was found that at an FSP initial velocity of 600m/s, the FSP residual velocity was reduced from 240.4m/s to 154.2m/s. Thus, if the irreversible-densification parameters of glass can be set to their optimal values, then the ballistic penetration resistance can be improved for a range of FSP impact velocities.

Materials-by-design Approach

In summary, the results obtained in the present work show that high-pressure irreversible-densification of glass can become a potent ballistic-resistance enhancing mechanism provided (via chemical modifications, and various thermo-mechanical and chemical treatments) the densification parameters can be set to or near optimal values. In our ongoing work, molecular-

level modeling is being extensively used to help better define such glass-modifying strategies/procedures. Specifically, within the molecular-level modeling framework, the effect of the glass chemistry and its random-network structure (as characterized by a set of random-network microstructural parameters [29,30,33]) on the irreversible-densification characteristics (i.e. the onset pressure and the extent of density change) is being examined. In addition, a link is being established between the molecular-level modeling parameters and the JH2 continuum-level material parameters. Table 1 summarizes the JH2 model parameters and lists their typical values for the case of a "***non-transforming***" soda-lime glass. In the present work, the Equation of State is modified to account for the irreversible densification transition and two strength parameters (parameters A and B) were modified. In our on-going work, an attempt is being made to identify additional JH2-model parameters which require modifications as the soda-lime glass chemistry and the random-network structure are being modified. It is hoped that this will become a fruitful exercise of the so-called "***materials-by-design***" concept in which component-level experimental and computational investigations are carried out in order to identify the envelope of optimal material properties. This is then followed by an extensive experimental/computational procedure aimed at designing and synthesizing the materials with the targeted set of properties/performance attributes.

2.5. Summary and Conclusions

Based on the results obtained in the present work, the following main conclusions can be made:

1. Molecular-level modeling of soda-lime glass revealed the occurrence of an irreversible-densification process when the pressure exceeds ca. 4GPa. Close examination of molecular-level topology revealed that this process is associated with an increase in the average coordination number of the silicon atoms, and the creation of two to fourfold (smaller, high packing-density) Si-O rings.

2. Modifications of the continuum-level material model for glass to include the effect of irreversible-densification resulted in minor improvements in the ballistic-penetration resistance of glass and only for high projectile initial velocities.

3. A parametric study involving variations of the key irreversible-densification parameters within physically realistic limits revealed that the optimal combination of these parameters can result in substantial improvements in the ballistic-resistance of glass over a wide range of projectile velocities.

4. It is suggested that various chemical-modification and thermo-mechanical treatment strategies should be employed in order to attain this optimal set of irreversible-densification parameters. This is an example of the materials-by-design concept within which an optimal combination of material parameters is identified in order to maximize component-level performance.

2.6. References

1. E. Strassburger, P. Patel, W. McCauley and D. W. Templeton, "*Visualization of Wave Propagation and Impact Damage in a Polycrystalline Transparent Ceramic- AlON*," Proceedings of the 22nd International Symposium on Ballistics, November 2005, Vancouver, Canada.
2. AMPTIAC Quarterly: *Army Materials Research*: *Transforming Land Combat Through New Technologies*, 8, no.4, 2004.
3. E. Strassburger, P. Patel, J. W. McCauley, C. Kovalchick, K. T. Ramesh and D. W. Templeton, "*High-Speed transmission Shadowgraphic and Dynamic Photoelasticity Study of Stress Wave and Impact Damage Propagation in Transparent Materials and Laminates Using The Edge-on Impact Method*," Proceedings of the 23rd International Symposium on Ballistics, Spain, April 2007.
4. D. Z. Sun, F. Andreiux, A. Ockewitz, "*Modeling of the Failure Behavior of Windscreens and Component Tests*," 4th LS-DYNA Users' Conference, Bamberg, Germany, 2005.
5. Woodcock, L. V., Angell, C. A. and Cheeseman, P., "*Molecular dynamics studies of the vitreous state: Simple ionic systems and silica*," The Journal Chemical Physics, 65: 1565–1577, 1976.
6. R. G. D. Valle, E. Venuti, "*High-pressure Densification of Silica Glass: A Molecular-dynamics Simulation*," Physical Review B, 54: 3809–3816, 1996.
7. K. Trachenko, M. T. Dove, "*Densification of Silica Glass under Pressure*," Journal of Physics: Condensed Matter, 14: 7449–7459, 2002.
8. Y. Liang, C. R. Miranda, S. Scandolo, "*Mechanical Strength and Coordinate Defects in Compressed Silica Glass: Molecular Dynamics Simulations*," Physical Review B, 75: 024205, 2007.
9. B. Nghiem, *PhD thesis*, University of Paris 6, France 1998.
10. C. Denoual and F. Hild, "*Dynamic Fragmentation of Brittle Solids: A Multi-scale Model*," European Journal of Mechanics of Solids A, 21: 105–120, 2002.
11. M. Yazdchi, S. Valliappan and W. Zhang, "*A Continuum Model for Dynamic Damage Evolution of Anisotropic Brittle Materials*," International Journal of Numerical Methods in Engineering, 39: 1555–1583, 1996.
12. F. Hild, C. Denoual, P. Forquin and X. Brajer, "*On the Probabilistic and Deterministic Transition Involved in a Fragmentation Process of Brittle Materials*," Computers and Structures, 81: 1241–1253, 2003.
13. M. Grujicic, B. Pandurangan, N. Coutris, B. A. Cheeseman, C. Fountzoulas and P. Patel, "*A Computational Investigation of the Multi-Hit Ballistic-Protection Performance of Laminated Glass-Polycarbonate Transparent Armor Systems*," Journal of Materials Engineering and Performance, 21: 837–848, 2012.

14. M. Grujicic, B. Pandurangan, W. C. Bell, N. Coutris, B. A. Cheeseman, C. Fountzoulas and P. Patel, "*An Improved Mechanical Material Model for Ballistic Soda-Lime Glass*," Journal of Materials Engineering and Performance, 18: 1012–1028, 2009.

15. M. Grujicic, B. Pandurangan, N. Coutris, B. A. Cheeseman, C. Fountzoulas and P. Patel, "*A Simple Ballistic Material Model for Soda-Lime Glass*," International Journal of Impact Engineering, 36: 386–401, 2009.

16. T. J. Holmquist, D. W. Templeton, K. D. Bishnoi, "*Constitutive Modeling of Aluminum Nitride for Large Strain High-strain Rate, and High-pressure Applications*," International Journal of Impact Engineering, 25: 211–231, 2001.

17. G. T. Camacho and M. Ortiz, "*Computational Modeling of Impact Damage in Brittle Materials*," International Journal of Solids and Structures, 33: 2899–2938, 1996.

18. H. Sun, "*COMPASS: An ab Initio Force-Field Optimized for Condensed-Phase Applications Overview with Details on Alkane and Benzene Compounds*," Journal of Physical Chemistry B, 102: 7338–7364, 1998.

19. H. Sun, P. Ren, and J. R. Fried, "*The COMPASS force field: parameterization and validation for phosphazenes*," Computational and Theoretical Polymer Science, 8(1/2): 229–246, 1998.

20. <http://www.accelrys.com/mstudio/ms modeling/discover.html>.

21. <http://www.accelrys.com/mstudio/ms modeling/visualiser.html>.

22. <http://www.accelrys.com/mstudio/ms modeling/amorphouscell.html>.

23. S. Nose, "*A unified formulation of the constant temperature molecular dynamics methods*," The Journal of Chemical Physics, 81: 511–519, 1984.

24. AUTODYN-2D and 3D, *Version 6.1*, *User Documentation*, Century Dynamics Inc., 2006.

25. G. R. Johnson and T. J. Holmquist, "*An Improved Computational Constitutive Model for Brittle Materials*," High Pressure Science and Technology, 1993. (AIP, New York, 1994).

26. T. J. Holmquist, D. W. Templeton, K. D. Bishnoi, "*Constitutive Modeling of Aluminum Nitride for Large Strain High-strain Rate, and High-pressure Applications*," International Journal of Impact Engineering, 25: 211–231, 2001.

27. M. Grujicic, B. Pandurangan, U. Zecevic, K. L. Koudela and B. A. Cheeseman, "*Ballistic Performance of Alumina/S-2 Glass-reinforced Polymer-matrix Composite Hybrid Lightweight Armor against Armor Piercing (AP) and Non-AP Projectiles*," Multidiscipline Modeling in Materials and Structures, 3: 287–312, 2007.

28. M. Grujicic,B. Pandurangan, C. D. Angstadt, K. L. Koudela, and B. A. Cheeseman, "*Ballistic performance optimization of a hybrid carbon nanotube/E-glass reinforced poly-vinyl-ester-epoxy matrix composite armor*," Journal of Material Science, 42: 5347–5349, 2007.

29. M. Grujicic, W. C. Bell, P. S. Glomski, B. Pandurangan, B. A. Cheeseman, C. Fountzoulas, P. Patel, D. W. Templeton and K. D. Bishnoi, "*Multi-length Scale Modeling of High-pressure Induced Phase Transformations in Soda-lime Glass*," Journal of Materials Engineering and Performance, 20: 1144–1156, 2011.

30. M. Grujicic, W.C. Bell, B. Pandurangan, B.A. Cheeseman, C. Fountzoulas, and P. Patel, "*Molecular-Level Simulations of Shock Generation and Propagation in Soda-Lime Glass*," Journal of Materials Engineering and Performance, 21: 1580–1590, 2012.

31. Bless, S. and Chen, T. *Impact damage in layered glass*. Int. J. Fract., 2010, 162(1–2), 151–158.

32. Gazonas, G. A., McCauley, J. W., Batyrev, I. G., Becker, R. C., Patel, P., Rice, B. M., and Weingarten, N. S. *Multiscale modeling of noncrystalline ceramics (glass)*. ARL Technical Report, ARL-MR-0765, Aberdeen Proving Ground, February 2011.

33. M. Grujicic, J. Megusar and T. Erturk, "*Elastic Moduli, Yield Stress and Ductility of Fully-Crystallized Co84Nb10B6 Metallic Glass*," International Journal of Rapid Solidification, 2: 165–173, 1986.

CHAPTER 3: ALL-ATOM MOLECULAR-LEVEL ANALYSIS OF THE BALLISTIC-IMPACT-INDUCED DENSIFICATION AND DEVITRIFICATION OF FUSED SILICA

3.1. Abstract

All-atom molecular-level computations are carried out to infer the dynamic response and material microstructure/topology changes of fused silica subjected to ballistic impact by a hard projectile. The analysis was focused on the investigation of specific aspects of the dynamic response and of the microstructural changes such as the deformation of highly sheared and densified regions, and the conversion of amorphous fused silica to SiO_2 crystalline allotropic modifications (in particular, α-quartz and stishovite). The microstructural changes in question were determined by carrying out a post-processing atom-coordination procedure. This procedure suggested the formation of stishovite (and perhaps α-quartz) within fused silica during ballistic impact. To rationalize the findings obtained, the all-atom molecular-level computational analysis is complemented by a series of quantum-mechanics density functional theory (DFT) computations. The latter computations enable determination of the relative potential energies of the fused silica, α-quartz and stishovite under ambient pressure (i.e. under their natural densities) as well as under imposed (as high as 50 GPa) pressures (i.e. under higher densities) and shear strains. In addition, the transition states associated with various fused-silica devitrification processes were identified. The results obtained are found to be in good agreement with their respective experimental counterparts.

3.2. Introduction

The present work deals with the problem of formation of crystalline phases (specifically α-quartz and stishovite) within a fused-silica (ceramic glass containing a high purity SiO_2) target during a ballistic impact. Hence, the main aspects of the present work include: (a) short- and intermediate-range order microstructure of fused silica; (b) (crystalline) allotropic modifications of SiO_2; and (c) devitrification (i.e. crystallization of glass taking place under the ballistic-impact loading conditions). A brief overview of these aspects of the problem at hand is presented in the remainder of this section.

3.2.1 Short- and Intermediate-Range Order Microstructure of Fused Silica

Ceramic glasses (like fused silica) are amorphous materials. The molecular-level microstructure of these materials involves entities such as a random network of covalently bonded atoms, atomic free volumes, (network-former) bridging and non-bridging oxygen atoms, cations of glass-modifier species, etc. However, despite the absence of a crystalline structure, the microstructure of ceramic glasses is not completely random. Rather, it involves different extents of short- and intermediate-range order spanning over a range of length-scales (from the quantum-mechanical to the continuum-level). To describe the structure of ceramic glasses as determined using various experimental techniques (e.g. neutron-diffraction, nuclear magnetic resonance, small angle X-ray scattering (SAXS), etc.), the so-called "random network model" [1] is typically employed. Such a model represents an amorphous material as a three-dimensional linked network of polyhedra. The character (number of facets) of the polyhedra is controlled by the species-specific coordination of the central (glass-forming) atom (cation). In the case of silicate-based glasses like fused silica and soda-lime glass, the polyhedron-center atoms are all silicon and each silicon atom is surrounded by four oxygen atoms (while each oxygen atom is connected to or bridges two silicon atoms) forming a SiO_4^{4-} tetrahedron. In glasses of different formulations, other types of polyhedra may exist. Since silicon has a tendency to form a continuous network with (bridging) oxygen atoms, SiO_2 is commonly referred to as a "network former". Other potential network formers in glass are boron and germanium oxides.

Numerous oxides and other additives are used to modify the basic silica tetrahedra network of silicate-based glasses in order to tailor their properties to specific applications. When alkali (or alkaline earth) oxides are added to a pure silicate-based glass, in order to accommodate

the excess of oxygen anions which are present due to the alkali (or alkaline earth) oxide dissociation, the continuity of the silica tetrahedra network becomes disrupted. The resulting glass structure contains additional non-bridging (connected to only one silicon atom) oxygen atoms. Charge transfer from the alkali earth metal atoms converts the non-bridging oxygen atoms into singly charged anions. The metallic cations formed in this process tend to hover around the non-bridging oxygen ions to provide local charge neutrality. Since alkali (or alkaline earth) based oxides cause a disruption in the continuous glass network, they are typically referred to as "network modifiers". As mentioned earlier, fused-silica ceramic glass investigated in the present work is chemically-pure SiO_2 (i.e. free of glass modifiers) and, hence, contains a continuous network of Si-O bonds (i.e. it is free of non-bridging oxygen atoms).

Within the random network model, the microstructure of glass is described using several network state parameters. Among these, the most frequently used are:

(a) the so-called R parameter, defined as the average number of oxygen ions per network forming ion which is used to describe the overall connectivity of a given network. In the case of fused silica, in which there are two (bridging) oxygen anions for every network-forming silicon cation, the R value is 2.0. In general, a larger value of the R parameter (brought about by the addition of network modifiers) implies a more open (less connected) weaker amorphous glass network. The effect of network formers on the R parameter is more complicated and depends on the network former coordination number, the strength of its bond with oxygen as well as its concentration;

(b) the so-called "X" parameter which defines the average number of non-bridging (connected to only a single network-forming cation) oxygen atoms per network polyhedron and takes on a zero value in the case of fused silica; and

(c) the so-called “Y” parameter which defines the average number of bridging (connected to two network-forming cations) oxygen atoms per network polyhedron and takes on a value of 4.0 in the case of fused silica.

In addition to the three parameters mentioned above, the “seemingly” random microstructure of ceramic glasses is also described using pair-wise correlation functions bond-length, bond-angle, Voronoi-cell volume, etc. distribution functions. A more detailed description of some of these microstructural parameters will be provided in Section IV, as part of a discussion of the results pertaining to the structure of the as-received and as-impacted fused-silica ballistic targets.

3.2.2 Allotropic Modifications of SiO_2

Previous investigations [e.g. 2–14] established that under high-rate (shockwave or ballistic) loading conditions, fused-silica targets can, at least in the vicinity of the impact region, experience transformation of the amorphous structure into a crystalline one. To help rationalize potential transformations of fused silica into various (crystalline) allotropic modifications of SiO_2, the corresponding temperature-pressure phase diagram is depicted in Figure 3-1. Before the phase diagram is analyzed briefly, three points should be made: (a) the phase diagram is of an equilibrium character and, thus, shows the regions of existence of various crystallographic allotropic modifications of SiO_2 after sufficient amount of time is given to the system to equilibrate (i.e. to acquire the state of minimal free energy); (b) there is no fused-silica region in the phase diagram since this SiO_2 state is of a metastable rather than a stable/equilibrium character; and (c) as far as the silica melt is concerned, it is a high-temperature molten state of SiO_2 and despite its amorphous nature, it is structurally different than fused silica, i.e. it possesses a much lower level of short- and intermediate-range order. While, according to the phase diagram depicted in Figure 3-1, there are six SiO_2 allotropic modifications (α-quartz, β-quartz, coesite, stishovite, β–tridymite and β-cristobalite) only three (α-quartz, coesite, stishovite) appear at room temperature and a temperature slightly higher than room temperature. Consequently, during a ballistic impact into a fused-silica target, these three SiO_2 allotropic modifications are most likely to form (provided such impact produces a local crystallization of the fused silica). Below, a brief description is provided of the main crystallographic features of these three SiO_2 allomorphs:

(i) α-quartz – Structure: Trigonal; Space Group: $P3_221$ (No. 154); Lattice parameters: a=b=4.9137 Å, c=5.4047 Å, $\alpha=\beta=90.0°$, $\gamma=120.0°$, Z=3 (where Z is the number of SiO_2 units

within the unit cell); Mass density: 2.66 g/cm^3. The atomic arrangement within the non-primitive unit cell of α-quartz is depicted in Figure 3-2(a).

(ii) Coesite – Structure: Monoclinic; Space group: C2/c; Lattice parameters: a = 7.1356 Å, b = 12.3692 Å, c = 7.1736 Å; α=90.0°, β = 120.34°, γ=90.0°, Z = 16; Mass density: 2.92 g/cm^3. The atomic arrangement within the non-primitive unit cell of coesite is depicted in Figure 3-2(b).

(iii) Stishovite – Structure: Tetragonal (ditetragonal dipyramidal); Space group: P 4_2/mnm (No. 136) P4_2/mnm {P4_2/m 2_1/n 2/m}; Lattice parameters: a = b = 4.179 Å, c = 2.6649 Å, Z=2; Mass density: 4.29 g/cm^3. The atomic arrangement within the non-primitive unit cell of stishovite is depicted in Figure 3-2(c).

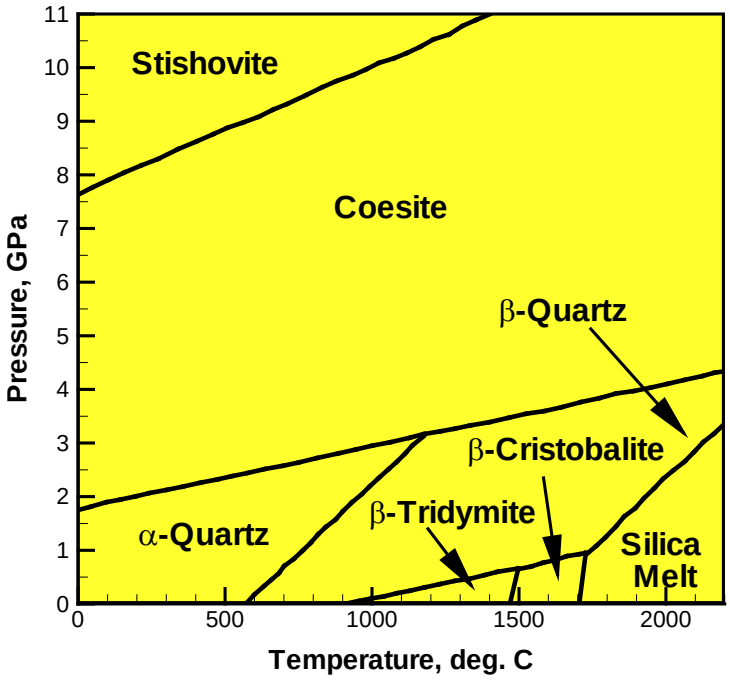

Figure 3-1 Temperature-pressure phase diagram for SiO2.

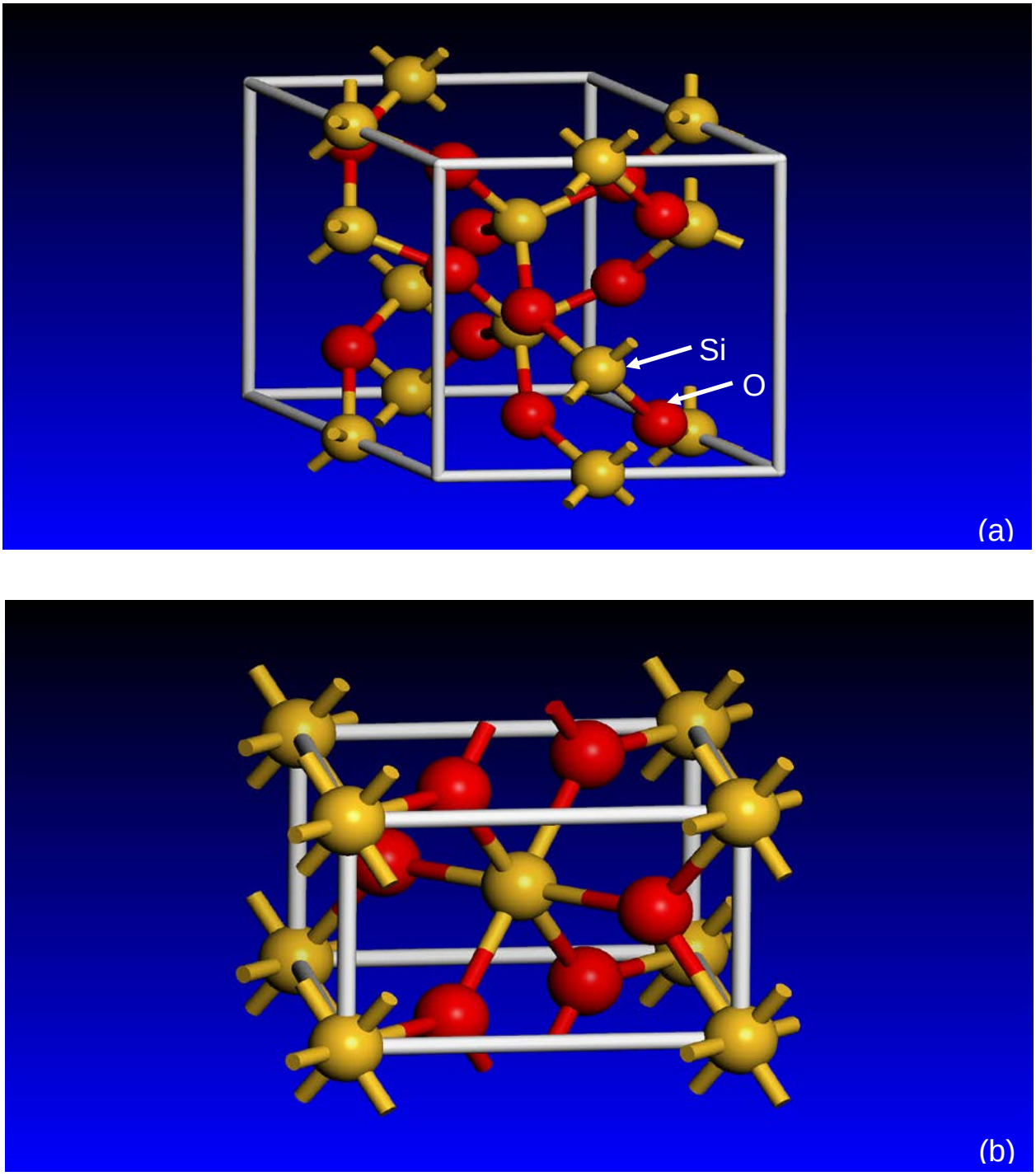

Figure 3-2 The atomic arrangements within the non-primitive unit cells of: (a) α-quartz; (b) stishovite; and (c) coesite.

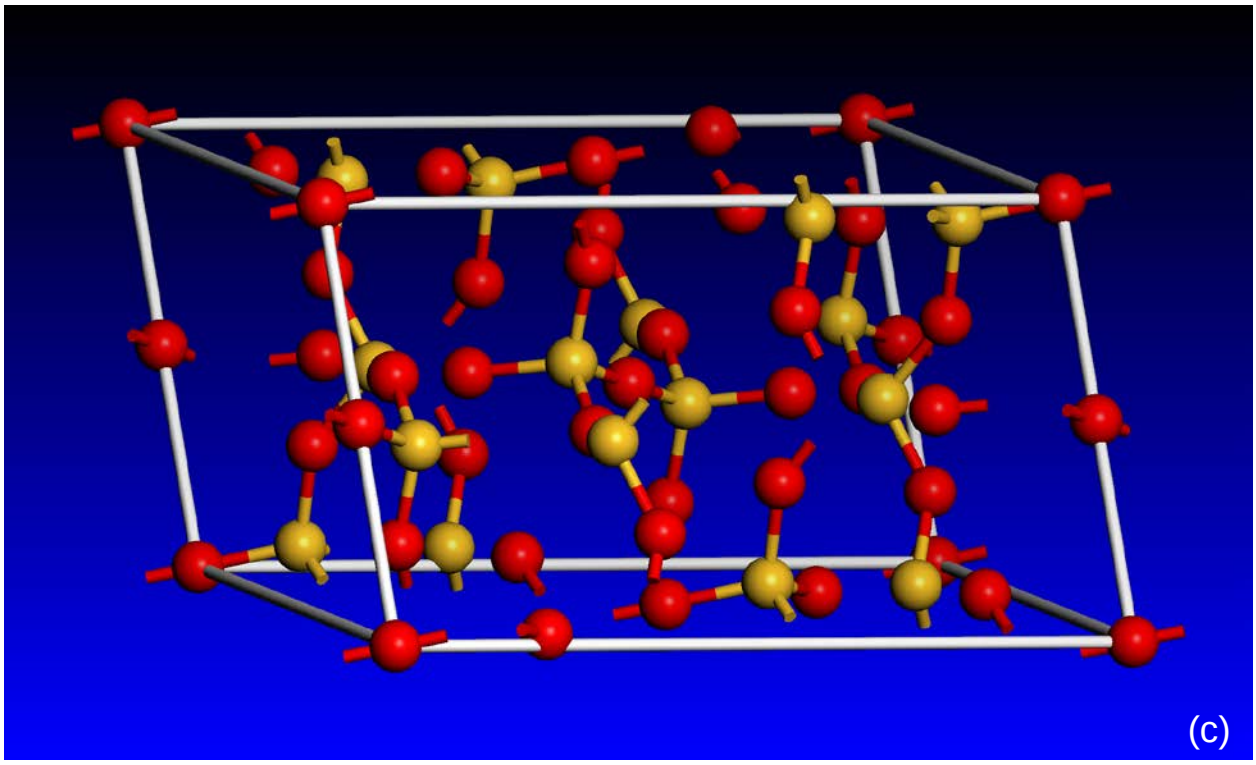

Figure 3-2 continued.

3.2.3 Dynamic-Loading-Induced Crystallization of Glass

A detailed overview of the public-domain literature carried out as part of the present work revealed a number of experimental and computational investigations dealing with the mechanical response of fused silica to dynamic loading. Some of these studies revealed the formation of shear bands within otherwise amorphous glass, others established the formation of crystalline phases (α-quartz and stishovite, but not coesite), while still others demonstrated increased hardness of the material surrounding the impact region without establishing the microstructural cause for this property change.

Chakraborty et al. [15] carried out a series of nano-indentation tests and showed that, as the loading rate increases, the extent of shear band formation in the region surrounding the indentation decreases, while the hardness value increases. No crystal-structure analysis was carried out to determine potential formation of any of the crystalline phases as a result of loading or to provide a rationale for the observed effect of the loading rate.

Tschauner et al. [16] investigated formation of stishovite in soda-lime glass during 57 GPa shock loading experiments and the reversion of this phase during subsequent release/unloading. They demonstrated that upon loading, high-density non-fully-crystallized SiO_2 phase was present in the "shocked" fused-silica. Upon static loading to only 13 GPa, this phase was fully converted into the crystalline stishovite, suggesting that the shock loading was able to devitrify fused silica and form crystalline stishovite.

Salleo et al. [17] demonstrated the formation of a defective form of stishovite in the surface region of fused-silica wafers through irradiation with a high-powered laser. The formation of such a phase and its continuous growth has been found to be the main cause of failure in optics used for high-power photonics.

Mantisi et al. [18] carried out a comprehensive atomic-scale simulation of fused silica under combined pressure/shear loading conditions. The results obtained established permanent/irreversible densification of the fused silica test sample and the change of the silicon and oxygen coordination relative to that present in the as-received fused silica. However, these microstructural changes could not be considered to be the result of glass devitrification/crystallization processes, i.e. the glass remained amorphous. One of the potential reasons for this observation was inadequacy of the interatomic potentials used in the simulation of the fused-silica mechanical behavior.

Kubota et al. [19] used molecular dynamics simulations to infer the atomic-scale structural changes in fused silica induced by shock-compression loading. The results obtained revealed that shock-compressive loading involving stress levels exceeding the Hugoniot Elastic Limit, gives rise to dramatic changes in the structure and topology of the fused-silica network and densifications of in excess of 20%. Coordination analysis of the as-shocked fused silica revealed the formation of under- and over-coordinated Si atoms. While under-coordinated Si atom regions could be interpreted as shock-induced fused-silica flaws, over-coordinated Si atom regions showed some resemblance to the crystalline stishovite. In addition to the coordination changes just described, changes in glass topology (such as increases in the number of the three-fold, four-fold, seven-fold and larger rings) were observed.

3.2.4 Main Objectives

The main objective of the present work is to carry out a series of all-atom molecular-level computational investigations of the ballistic impact by a hard projectile onto a fused-silica target-plate, and to characterize the target-plate material response to such impact. In addition, in order to help rationalize some of the findings regarding the microstructure and topology of the fused-silica following the impact, a series of quantum-mechanical Density Functional Theory (DFT) analyses will be carried out. These analyses will help reveal the relative potential energies of the SiO_2 amorphous state and two SiO_2 crystalline allotropic modifications, i.e. α-quartz and stishovite, and the changes in these energies as a function of the extent of material compression and shear.

3.2.5 Chapter Organization

Details regarding the all-atom molecular-level computational procedure used to simulate the ballistic impact by a hard projectile onto a fused-silica target-plate, are presented in Section 3.3. The quantum-mechanical DFT procedure used to determine the relative potential energies of the SiO_2 amorphous state and the two SiO_2 crystalline allotropic modifications, as well as the associated transition states (to be defined later), is provided in Section 3.4. Key results obtained in the present work are presented and discussed in Section 3.5, while a summary of the main findings and conclusions is provided in Section 3.6.

3.3. MOLECULAR-LEVEL ANALYSIS OF BALLISTIC IMPACT

As mentioned earlier, one of the objectives of the present work is to carry out a series of all-atom molecular-level computational analyses of the problem of a ballistic-impact by a hard projectile onto a fused-silica target-plate. Within the all-atom molecular-level computational methods and tools, every atom and bond is explicitly accounted for and molecular mechanics and dynamics algorithms are used to quantify the state and behavior of the material under investigation. All-atom molecular-level simulation problems typically require the specification of the following: (a) a molecular-level computational model consisting of atoms, ions, functional groups and/or molecules; (b) a set of force-field functions (mathematical expressions describing bonding and non-bonding interactions between the model constituents, e.g. atoms, ions, etc.); and (c) a computational method(s) to be used in the simulation. More details of these three aspects of the molecular-level modeling and simulation of fused silica are provided below.

3.3.1 Computational Model

The computational model used in this portion of the work consists of two distinct sub-domains: (a) the projectile sub-domain; and (b) the target-plate sub-domain. The two sub-domains are shown and labeled in Figure 3-3(a).

The projectile sub-domain is of a right circular solid cylindrical geometry (height over diameter ratio = 1.0, axis aligned with the z-direction). While, at least, the core of ballistic projectiles is typically made of hard and heavy metallic materials (e.g. tungsten), metallic materials could not be used in the construction of the projectile in the present work. The reason for this is the absence of metallic force-field functions (in the pure metallic environment) within the force-field function database used in the present work. Consequently, the projectile was made of another hard material, diamond. Typically, the projectile sub-domain contained 150 covalently-bonded carbon atoms forming a perfect single-crystalline diamond structure.

As far as the target-plate sub-domain is concerned, it is of a rectangular parallelepiped (plate-like) shape, and is made of fused silica. At the molecular level, fused silica is modeled as a discrete-particle based material consisting of silicon (Si) and oxygen (O) atoms mutually bonded via a single covalent bond and forming a connected, non-structured/amorphous network of silica (SiO_4^{4-}) tetrahedra. While fused silica is an amorphous material and does not possess any long-range regularity in its atomic/molecular structure, modeling of bulk behavior of fused silica is typically done at the molecular level by assuming the existence of a larger (amorphous) unit cell. Repetition of this cell in the three orthogonal directions (the process also known as application of the “periodic boundary conditions”) results in the formation of an infinitely-large bulk-type material. This procedure was adopted in the present work. The parallelepiped-shaped target-plate computational sub-domain used in the present (ballistic-impact) analysis contained 9600 particles

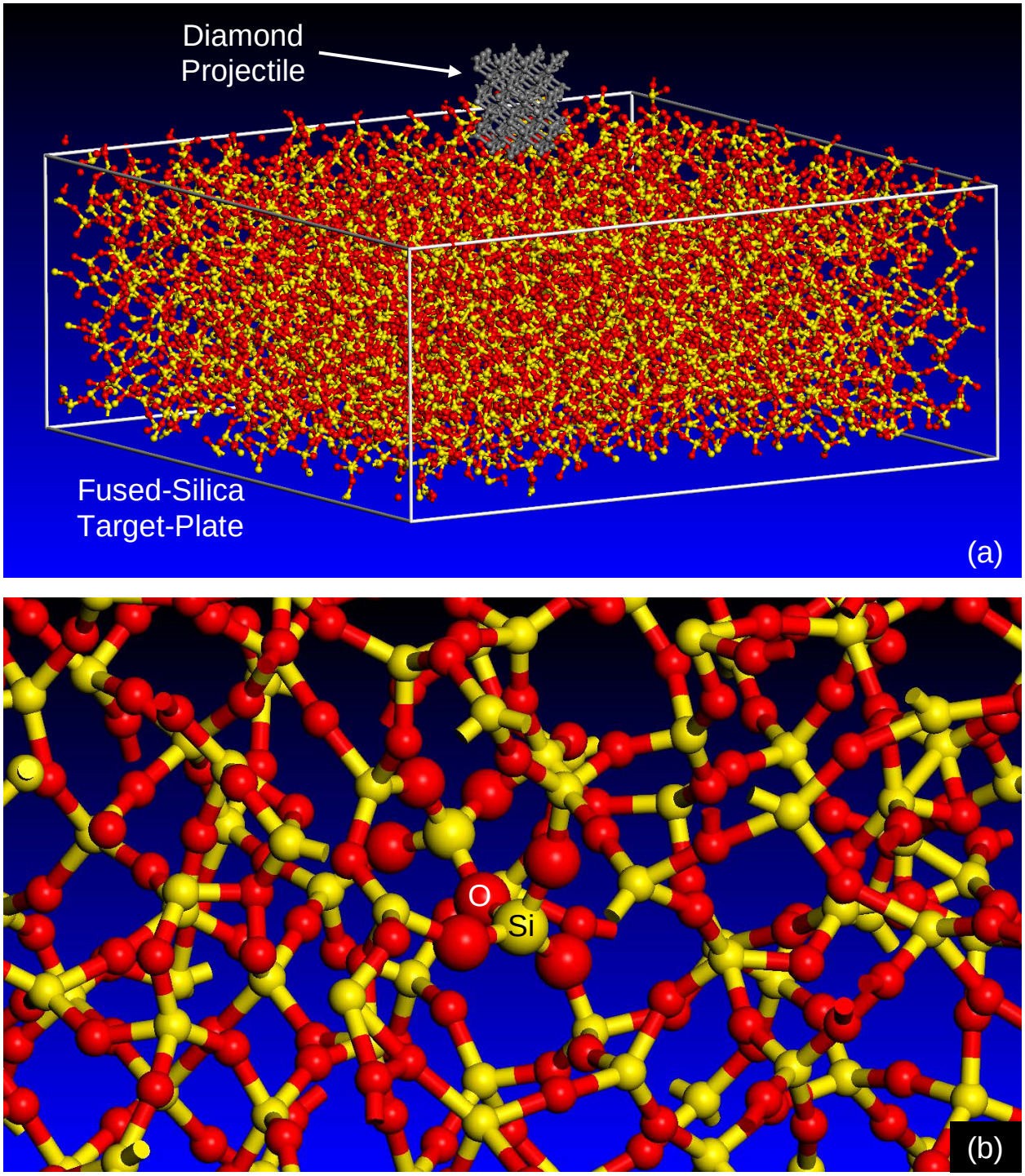

Figure 3-3 (a) The computational model used in this portion of the work, consisting of two distinct sub-domains for the projectile and the target-plate; and (b) close-up of the resulting fused-silica molecular-level random-network microstructure. Larger ball sizes are used in this figure to highlight a pair of SiO_4^{4-} tetrahedra sharing a common oxygen atom.

(3200 Si atoms and 6400 O atoms). The edge-lengths of the computational cell were initially set to a= b~7.9 nm, c~2.9 nm (approximately), yielding a fused-silica initial nominal density of 2.19 g/cm^3. The three edges (a, b and c) of the cell were aligned respectively with the three coordinate axes (x, y and z) (with the target-plate thickness aligned with the z-direction).

To create the ambient temperature/pressure "equilibrium" atomic configuration within the computational cell, the following procedure was implemented within the Visualizer [20] program from Accelrys:

(a) A starting computational cell was first constructed by stacking the appropriate number of α-quartz unit cells in the three orthogonal directions. This was followed by the affine distortion of the computational cell in order to obtain the correct mass density of the fused-silica amorphous state (obtained using the following procedure);

(b) To convert the crystalline material into an amorphous one, a stochastic bond-switching algorithm was then implemented [21] using a Monte Carlo computational procedure. Within this algorithm, two neighboring Si-O pairs were randomly selected from the computational cell and the potential-energy change ΔE resulting from the Si-O bond-switching computed. In the ΔE<0 case, the bond-switching in question was accepted without any additional conditions. On the contrary, in the ΔE>0 case, a Boltzmann probability factor $P_B = \exp\left[-\Delta E/\left(3NkT/2\right)\right]$ (where N is the number of atoms within the computational cell, k is the Boltzmann constant, and T is the absolute temperature) was first calculated and compared with a random number RN drawn from a (0,1) uniform distribution function. The bond switching in question was then adopted only if P_B>RN;

(c) the resulting structure was then subjected to a carefully devised set of NVT (where N(=9600) is the (fixed) number of atoms within the computational cell, V, the computational cell volume (also fixed), and T is a fixed temperature) molecular dynamics simulations. Specifically, the NVT simulations were started at a temperature of 5300 K and carried out in such a way that the temperature was controlled using the following "simulated-annealing" scheme: (i) a particle-velocity scaling algorithm was applied every time step for the first 6000 steps. This enforced strict control of the temperature but produced particle velocities which were inconsistent with the target-temperature Maxwell-Boltzmann distribution function; (ii) within the next 6000 NVT simulation steps, the frequency of particle-velocity scaling was decreased to every 40 time steps while a Nosé-Hoover [22] temperature-control algorithm ("thermostat") was applied between the particle-velocity scaling steps. A brief description of the Nosé-Hoover thermostat could be found in our prior work [23]; and (iii) during the final 8000 steps, the temperature was controlled using only the Nosé-Hoover thermostat. This procedure ensured an efficient temperature control while yielding an equilibrium state of the material (i.e. a particle-velocity distribution consistent with the target-temperature Maxwell-Boltzmann distribution function).

Upon establishing the thermodynamic equilibrium at 5300 K, the target temperature was reduced by 500 K and then this procedure was re-applied at progressively (by 500 K) lower temperatures until the final temperature of 300 K was reached. The total system equilibration procedure typically involved simulation times on the order of 500 ps resulting in an average cooling-rate of ~10 K/ps. A close-up of the resulting fused-silica molecular-level random network is displayed in Figure 3-3(b). Larger ball sizes are used in this figure to highlight a pair of SiO_4^{4-} tetrahedra sharing a common oxygen atom.

3.3.2 Force-fields

The behavior of a material system at the molecular-level is governed by the appropriate force-fields which describe, in an approximate manner, the various interactions taking place between the constituent particles, atoms, ions, charge groups, etc. In other words, the knowledge of force-fields enables determination of the potential energy of a system in a given configuration. In addition, gradients of the force field functions quantify the net forces experienced by the particles, the information that is needed in the molecular dynamics simulations.

In general, the potential energy of a system of interacting particles can be expressed as a sum of the valence (or bond), $E_{valence}$, cross-term, $E_{cross\text{-}term}$, and non-bond, $E_{non\text{-}bond}$, interaction energies as:

$$E_{total} = E_{valence} + E_{cross-term} + E_{non-bond} \quad (1)$$

The valence energy generally accounts for the contribution of valence electrons bonding and contains the following components: (a) a bond length/stretching term; (b) a two-bond angle term; (c) a three-bond dihedral/torsion angle term; (d) an inversion (or a four-atom out-of-plane interaction) term; and (e) the so-called "*three-atom Urey-Bradley term*" (i.e. the interaction of two atoms which are bonded to a common atom).

The cross-term interacting energy accounts for the cross-interactions between the aforementioned valence-energy components and includes terms like: (a) stretch-stretch interactions between two adjacent bonds; (b) stretch-bend interactions between a two-bond angle and one of its bonds; (c) bend-bend interactions between two valence angles associated with a common vertex atom; (d) stretch-torsion interactions between a dihedral angle and one of its end bonds; (e) stretch-torsion interactions between a dihedral angle and its middle bond; (f) bend-

torsion interactions between a dihedral angle and one of its valence angles; and (g) bend-bend-torsion interactions between a dihedral angle and its two valence angles.

The non-bond interaction term accounts for the interactions between non-bonded atoms and includes the van der Waals energy and the Coulomb electrostatic energy.

In the present work, the so-called "*COMPASS*" (Condensed-phase Optimized Molecular Potentials for Atomistic Simulation Studies) force field is used [24, 25]. This highly accurate force field is of an ab-initio type since most of its parameters were determined by matching the predictions made by the ab-initio quantum mechanics calculations to the condensed-matter experimental data. A summary of the COMPASS force-field functions can be found in our previous work [26].

3.3.3. Computational Method(s)

All the all-atom molecular-level calculations were carried out within the present work using Discover [22] (an atomic simulation program from Accelrys). Both equilibrium and non-equilibrium molecular-dynamics (MD) analyses were employed in the present work. Within the molecular dynamics method, negative gradient of the potential energy evaluated at the location of each atom is first used to compute forces acting on each atom. Then, the associated Newton's equations of motion (three equations for each atom) are integrated numerically over a femtosecond-long time interval. This procedure is repeated over a pico-to-nanosecond-long simulation time in order to determine the temporal evolution of the material molecular-level configuration. Equilibrium MD was used in the aforementioned Monte Carlo based bond-switching procedure to generate amorphous state from the crystalline state in SiO_2. Non-equilibrium MD was used during the simulation of the ballistic impact by a hard projectile onto a fused-silica target-plate.

Within the equilibrium MD method, the system under consideration is coupled to an (external) environment (e.g. constant-pressure piston, constant-temperature reservoir, etc.) which ensures that the system remains in equilibrium (i.e. the system is not subjected to any thermodynamic fluxes). In the present work, *NVT*, *NPT* (*P* is pressure) and *NVE* (*E* is the total energy) equilibrium MD simulations were used. Equilibrium MD calculations enable determination of the (equilibrium) thermodynamic properties of a material system through the use of time averages of the state variables sampled along the calculated system trajectories.

Within non-equilibrium MD, the system is subjected to large mechanical and/or thermal perturbations (momentum transfer from the moving projectile to the initially stationary target-plate, in the present case). As a consequence, the system experiences large fluxes of its thermodynamic quantities (mass, momentum and energy, in the present case). Since Discover was initially designed to carry out equilibrium MD simulations, a procedure had to be devised to deactivate "*equilibration*" portions of this algorithm so that non-equilibrium MD calculations can be carried out. This procedure was implemented using a Discover input file [20]. This file is written using the Basic Tool Command Language (BTCL) which enabled the use of a scripting engine that provides very precise control of simulation tasks (e.g. specification of the projectile constant incident velocity, deactivation of the thermal-equilibration algorithm, etc.)

3.3.4. Computational Method(s)

The problem addressed in the present work involves all-atom molecular-level computational modeling of the ballistic impact by a hard projectile onto a fused-silica target-plate, and the coordination/topology analysis of the as-impacted fused silica. The projectile is of a solid right circular cylindrical shape, and impacts the target-plate normally (i.e. at a 0° obliquity angle through-the-thickness direction). The projectile is driven at a constant velocity and the target-plate is confined only along its bottom rim.

3.4. QUANTUM-MECHANICAL ANALYSIS OF GLASS DEVITRIFICATION

In order to rationalize the molecular-level computational results pertaining to the ballistic impact of a projectile onto the fused-silica target plate, and the potentially accompanying changes in the glass microstructure, a quantum-mechanical DFT analysis of the fused-silica devitrification process is carried out in the present work. The main purpose of this analysis was the establishment of: (a) the energy difference between the as-received glass material state and the crystalline α-quartz and stishovite SiO_2 states; (b) determination of the transition-state energy barriers associated with the two (glass $\rightarrow$ α-quartz or glass $\rightarrow$ stishovite) fused-silica devitrification processes. The transition state is the material state along the devitrification pathway which is associated with the maximum potential energy; and (c) the effect of high pressure and shear stresses on the energetics of the initial, transition and final states.

3.4.1 Computational Models

As mentioned earlier, coesite does not typically form under ballistic-loading conditions and, hence, will not be the subject of the present DFT investigation. Consequently, only two glass devitrification product states, α-quartz and stishovite, will be investigated. The respective computational cells are shown in Figures 3-2(a) and (c). Since fused silica possesses an amorphous structure, without long-range order, a substantially larger computational cell had to be used for this (initial) state of SiO_2, in order to more accurately determine its average potential energy. An example of such a computational cell is given in Figure 3-3(a), the target-plate computational sub-domain.

In the portion of the analysis dealing with determination of the transition state, the initial and final states of the material have to contain the same number of atoms and species. For that reason, fused-silica computational cells containing six Si and twelve O atoms (the numbers match those seen in Figure 3-2(a)) are used to investigate fused-silica $\rightarrow$ α-quartz transition state. Likewise, fused-silica computational cells containing two Si and four O atoms (the numbers match those seen in Figure 3-2(c)) are used to investigate fused-silica $\rightarrow$ stishovite transition state. In order to account for the statistical effects associated with the extraction of such small fused-silica computational cells from a larger computational cell, ten small fused-silica computational cells (not shown for brevity) are generated for each of the two transition state analyses and the results obtained are averaged out.

3.4.2 Computational Method

All calculations in the present work are carried out using the *ab-initio* density-functional theory code DMol^3 developed by Accelrys Inc. [28]. In this code each electronic wave function is expanded in a localized atom-centered basis set with each basis function defined numerically on a dense radial grid. No pseudopotential approximation is used for the near-core electrons. Instead, all-electron calculations are performed with a double numerical polarized (DNP) basis set, the most complete basis set available in the DMol^3 code. This basis set is equivalent to the commonly used analytical 6-31g** basis set, a split-valence basis set with polarization functions *p* to H and *d* to C, and the halogens [29].

To improve the computational speed, the local-density approximation (LDA) [30] for the exchange-correlation potential is often used within the DFT formulation, which assumes that the electron-charge density varies slowly on the atomic length scale. However, the LDA method is found not to have the correct asymptotic behavior and generally overestimates the magnitude of the chemical-bond energy. To overcome this overbinding phenomenon, one of the existing density gradient expansion schemes (also referred to as Generalized Gradient Approximations, GGA), which includes the effect of charge-density inhomogeneity, needs to be utilized. Following Grujicic et al. [31,32], the Perdew-Burke-Ernzerhof (PBE) gradient-corrected functional [33] is used in the present work. A standard value of 5.5 Å is assigned to the finite basis-set cutoff radius.

3.4.3 Determination of the Transition States

In general, the transition state lies on a Minimum Energy Pathway connecting the initial and final states' potential-energy minima, where the pathway and the two minima all reside on the associated potential energy hypersurface. The defining feature of the transition state is that it is associated with a minimum potential energy in all the directions but one (in which the potential energy experiences a maximum). In the case of a system with two degrees of freedom, the transition state corresponds to a saddle point, as depicted in Figure 3-4. Moving the system under consideration from the transition state point (in either direction) along the steepest-descent path leads to the initial/final states.

There are several algorithms which are commonly used for determination of the transition state. The three most frequently used include: (a) linear synchronous transit (LST) [35], used in the present work; (b) quadratic synchronous transit (QST) [35]; and (c) nudged elastic band [34].

The LST method constructs the initial-state → final-state transition pathway by connecting each atom in its initial and final states using a straight-line pathway, and by constructing the intermediate configurations by linearly and synchronously interpolating the atomic positions along the pathway of each atom. In other words, the structure of the intermediate states is a rule of mixtures of the initial structure and the final structure, with a weighting factor for the product state $f = (0,1)$. The potential energy is next determined for all the intermediate states, and the one associated with the largest potential energy is taken as a first approximation of the system transition state. The location of the transition state is further improved by carrying out a constrained optimization of its first approximation.

.

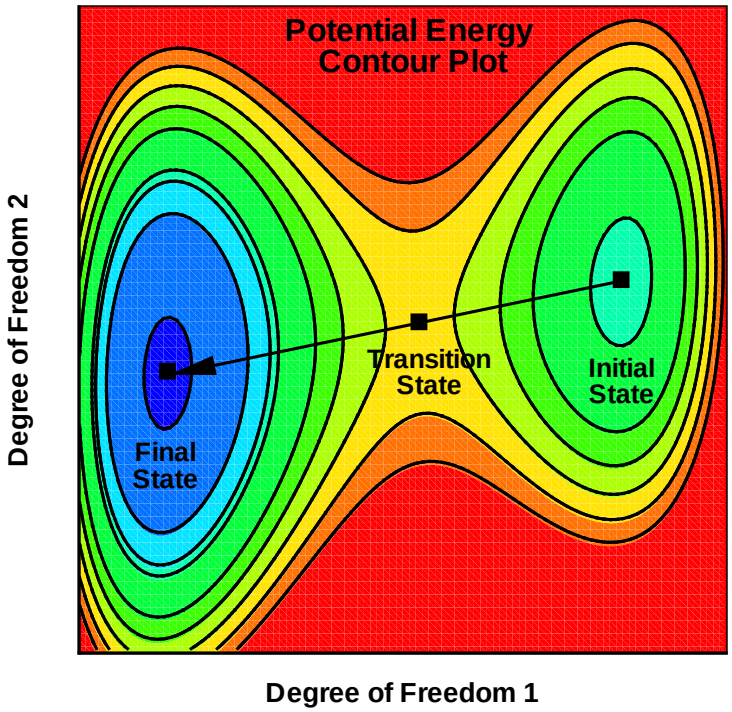

Figure 3-4 The initial-to-final state transition in a two-degree-of-freedom system and identification of the corresponding transition state (the saddle point).

3.5. Results and Discussion

3.5.1 Validation of the As-Received Fused-Silica Material State

In this section, an attempt is made to validate the fused-silica room-temperature/ ambient-pressure structure obtained through application of the previously-described bond-switching and simulated-annealing computational procedures. In particular, the material mass density, the partial radial distribution functions for the three (Si-Si, Si-O and O-O) atomic pairs and distributions of the Si-atom and O-atom coordination numbers are calculated and compared with their experimental counterparts.

To compute the material mass density, the partial radial distribution functions and atomic coordination combinations, *NPT* equilibrium molecular dynamics simulations were run at the room temperature and the ambient pressure. Simulations were carried out for over 10000 (0.1 fs-long) time steps while maintaining the temperature using the Nosé-Hoover thermostat and scaling the particle velocities every ten time steps. Pressure was controlled using a Berendsen barostat [36]. A brief overview of this barostat is provided in our prior work [37].

Mass Density: The average mass density of fused silica computed from the computational-cell average volume and the cell mass has been found to be about 1.0% greater than its commonly cited experimental counterpart of 2.19 g/cm^3. This computation/experiment agreement has been deemed to be reasonably good.

Radial Distribution Functions: The partial radial distribution (often also referred to as the partial pair correlation) function provides a measure of the probability that, given the presence of an atom of type α at the origin of an arbitrary reference frame, there will be an atom of type β within a spherical shell of infinitesimal thickness *dr* at a distance *r* from the reference atom.

Alternatively, this function can be considered as a function which defines a ratio of the probability of finding an α–β atomic pair with the separation distance r, and the average probability of finding an α–β atomic pair at the same distance. In amorphous materials like fused silica, the partial pair correlation functions are quite important since they: (a) provide an insight into the short-range order of the system; (b) can be used in the assessment of continuum-level thermodynamic material properties; and (c) provide a way of validating the molecular-level calculations since these quantities can also be determined experimentally using X-ray diffraction.

The computed partial radial distribution functions for the as-received/initial state of fused silica, Figure 3-5(a), are compared with their counterparts based on the shell model molecular dynamics calculations [38], Figure 3-5(b). This comparison reveals that the present computational results are qualitatively similar to the ones reported in Ref. [39-41]. As far as the quantitative agreement between the two sets of results is concerned, it could be characterized as being fair to good.

Si- and O-atom Coordinations: Since fused silica does not contain any network modifiers and Si is the only network-forming element, each Si atom is expected to be bonded to four O atoms while each O atom is expected to be bonded to two Si atoms. This is confirmed through post-processing of the molecular dynamics results, as shown in Figures 3-6(a)-(b) (the data labeled "Initial State"). The results shown in Figure 3-6(a) pertain to the Si-atom coordination while those displayed in Figure 3-6(b) refer to the O-atom coordination.

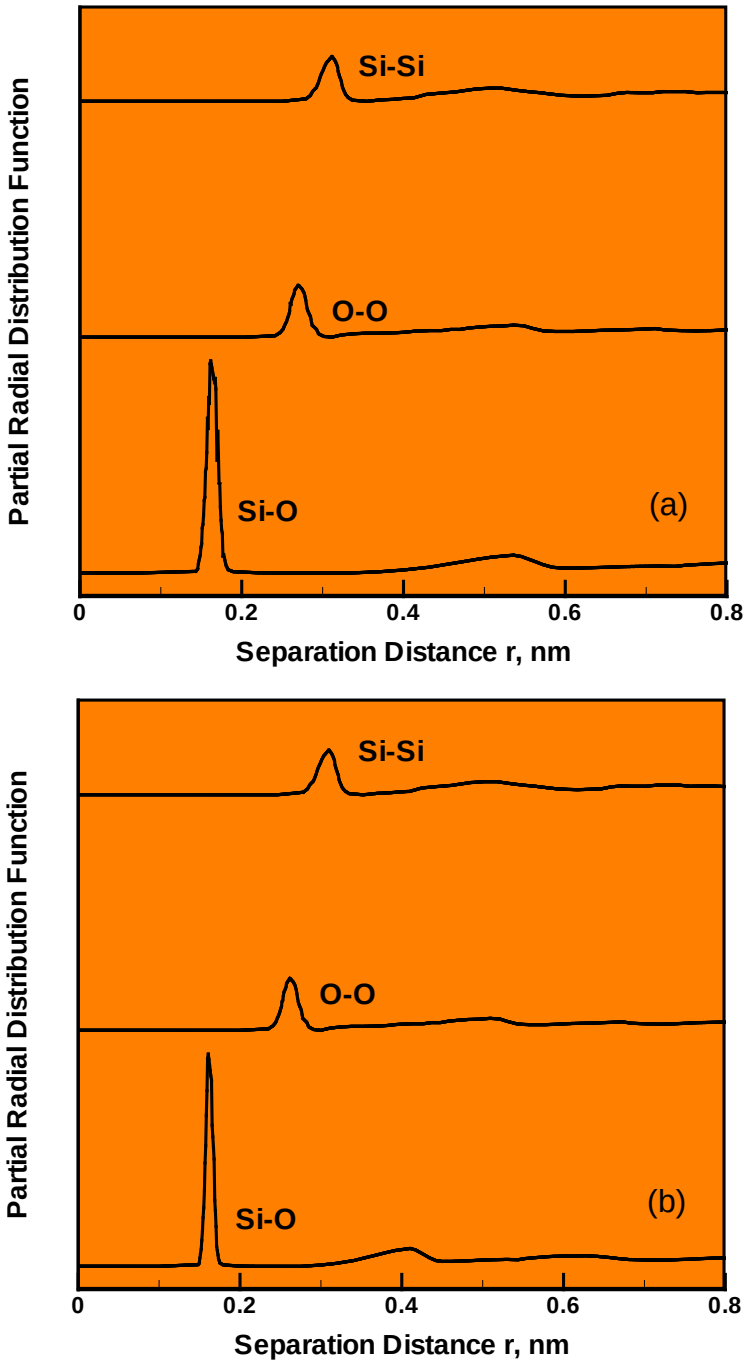

Figure 3-5 A comparison between the fused-silica Si-Si, O-O, and Si-O partial radial distribution functions computed in (a) the as-received/initial state, determined in the present work; and (b) the equilibrium initial state as reported in Tilocca et al. [32].

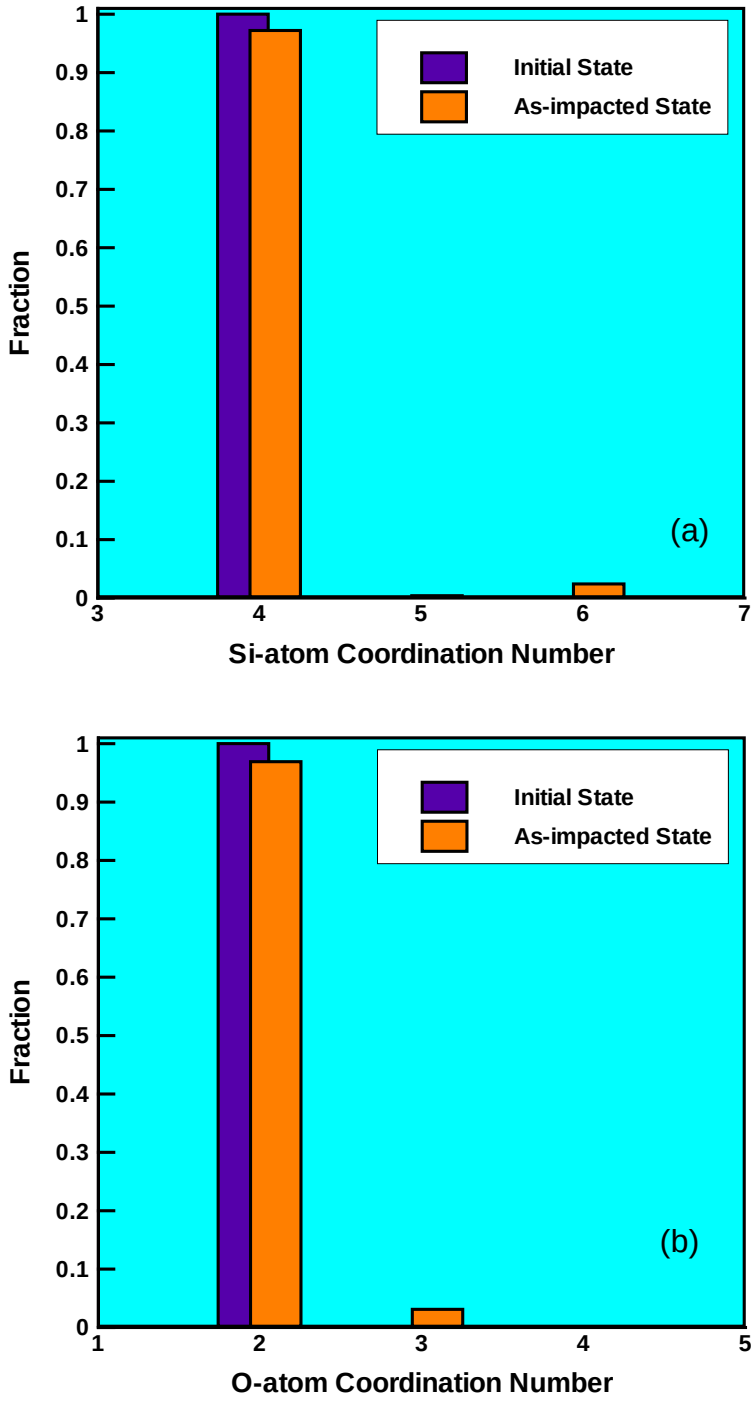

Figure 3-6 Fractional distribution of the: (a) Si-atom; and (b) O-atom coordination numbers in the initial and the as-impacted states of fused silica.

3.5.2 Analysis of the Ballistic Impact

Temporal evolution of the computational domain at four (0.5 ps, 1.5 ps, 2.5 ps, and 3.5 ps) times following the initial contact between the diamond solid right-circular cylindrical projectile moving at a high velocity and the fused-silica target plate is depicted in Figures 3-7(a)–(d), respectively. For improved clarity, the symbols for the target-plate atoms made smaller. Examination of the results displayed in Figures 3-7(a)–(d) reveals that the target-plate material in the close vicinity of the projectile experiences major changes. However, the nature of these changes, i.e. the accompanying alterations in the material microstructure and topology, are difficult to infer from the results displayed in Figures 3-7(a)–(d). To overcome this problem, a few selected results revealing the as-impacted fused-silica local microstructure in the region adjacent to the projectile are presented and discussed below.

Figure 3-8 shows a thin slice of the fused-silica target plate, having the faces parallel to the x-z plane, centered on the hole created by the projectile after penetrating the target by about half of its thickness. Examination of the fused-silica microstructure within this slice revealed the presence of numerous six-folded Si and three-folded O atoms (the Si and O coordinations characteristic of stishovite and not of fused silica). In Figure 3-8, two six-coordinated Si and two three-coordinated O atoms are highlighted by assigning a larger sphere radius to the atoms involved. In addition, six-folded Si atoms and three-folded O atoms are tagged with circular symbols. In addition to the highlighted atomic configurations, many more instances of six-coordinated Si and three-coordinated O are found in the region surrounding the penetration hole. Since, as mentioned earlier, the initial state of fused-silica only contained four-folded Si and two-folded O atoms, this finding suggests that ballistic impact can lead, at least locally, to the conversion of amorphous SiO_2 into the crystalline (but highly deformed) stishovite structure.

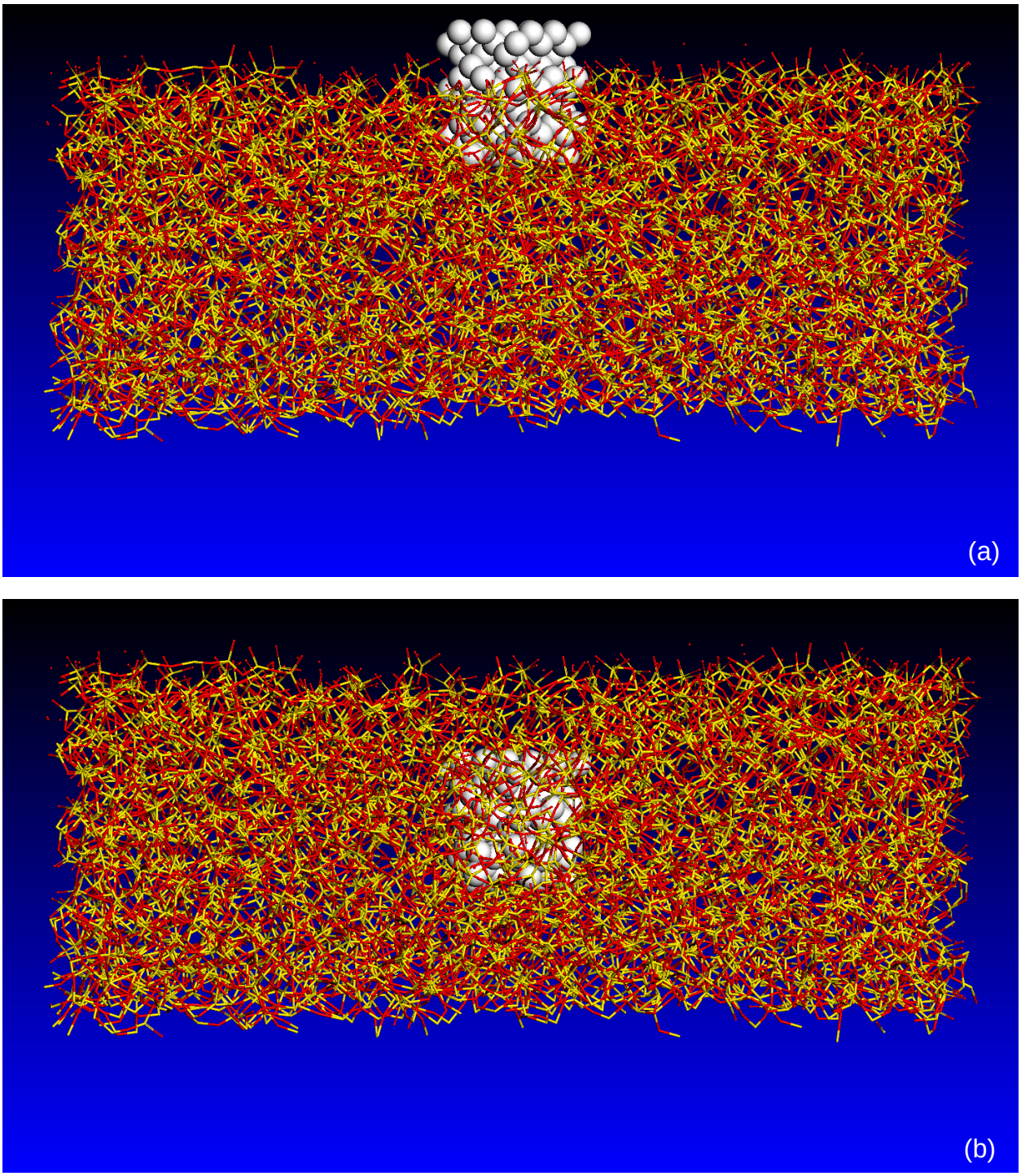

Figure 3-7 Temporal evolution of the computational domain at four times: (a) 0.5 ps; (b) 1.5 ps; (c) 2.5 ps; and (d) 3.5 ps, following the initial contact between the diamond solid right-circular cylindrical projectile moving at a high velocity and the fused-silica target plate.

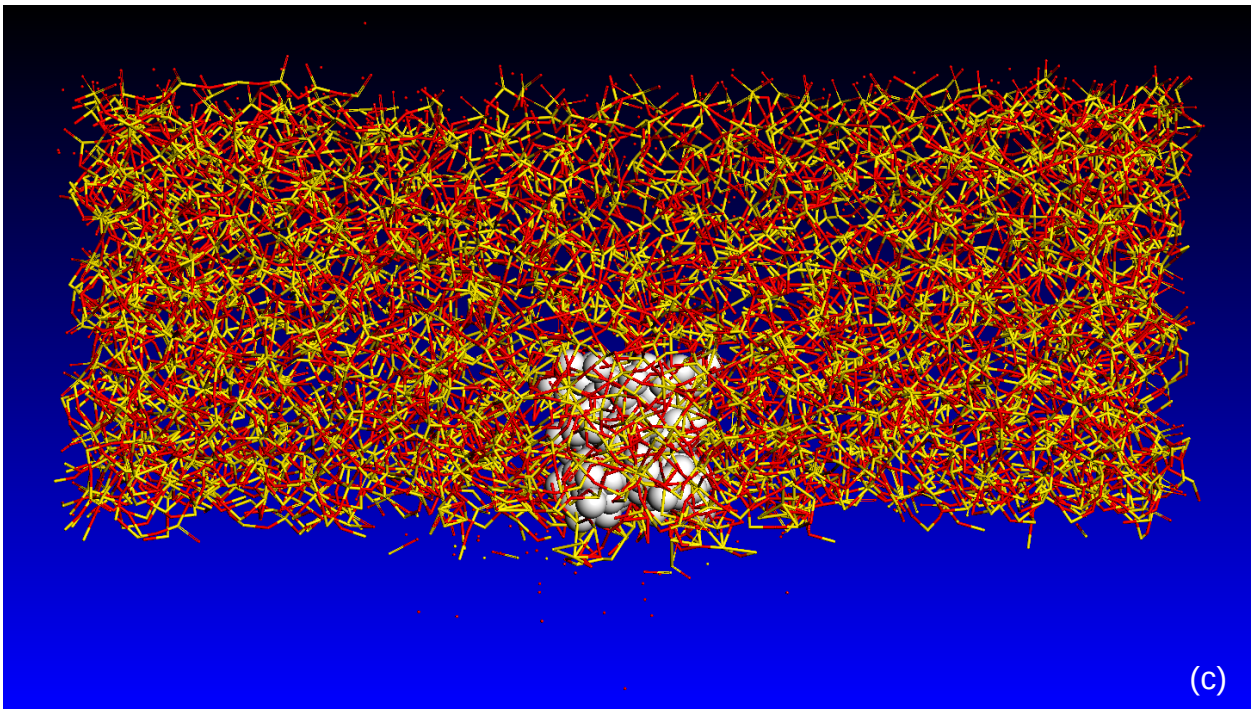

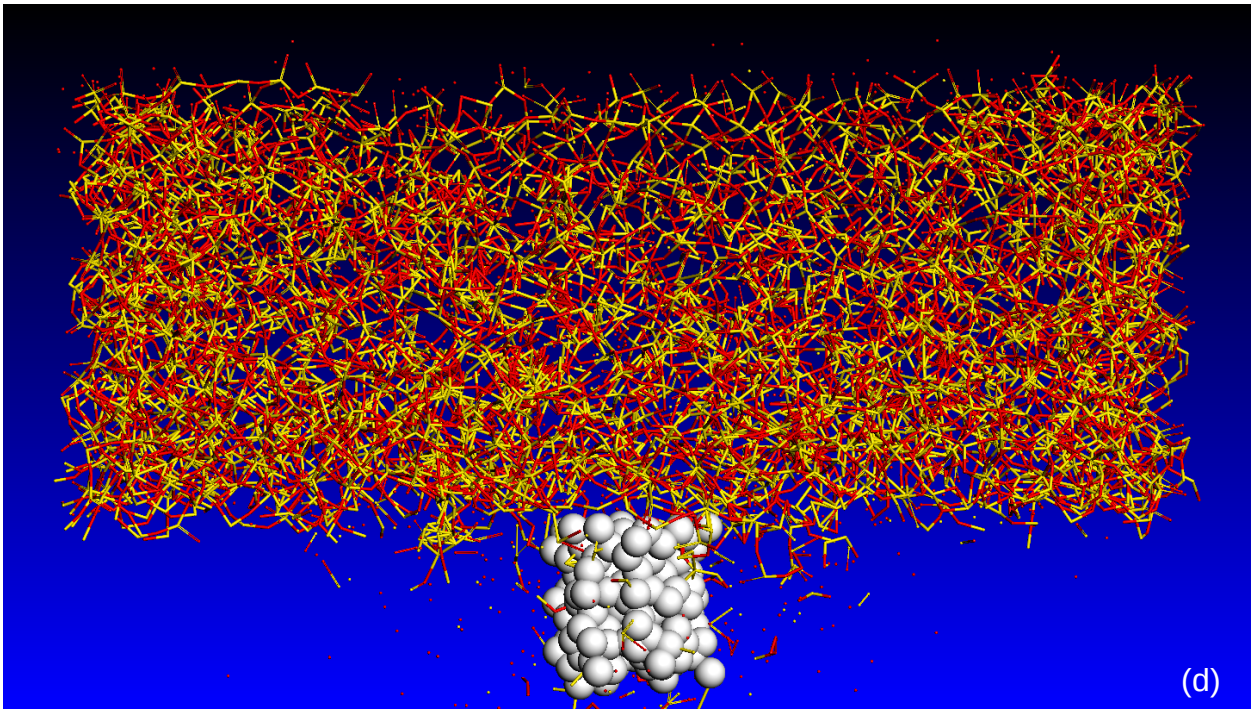

Figure 3-7 Continued.

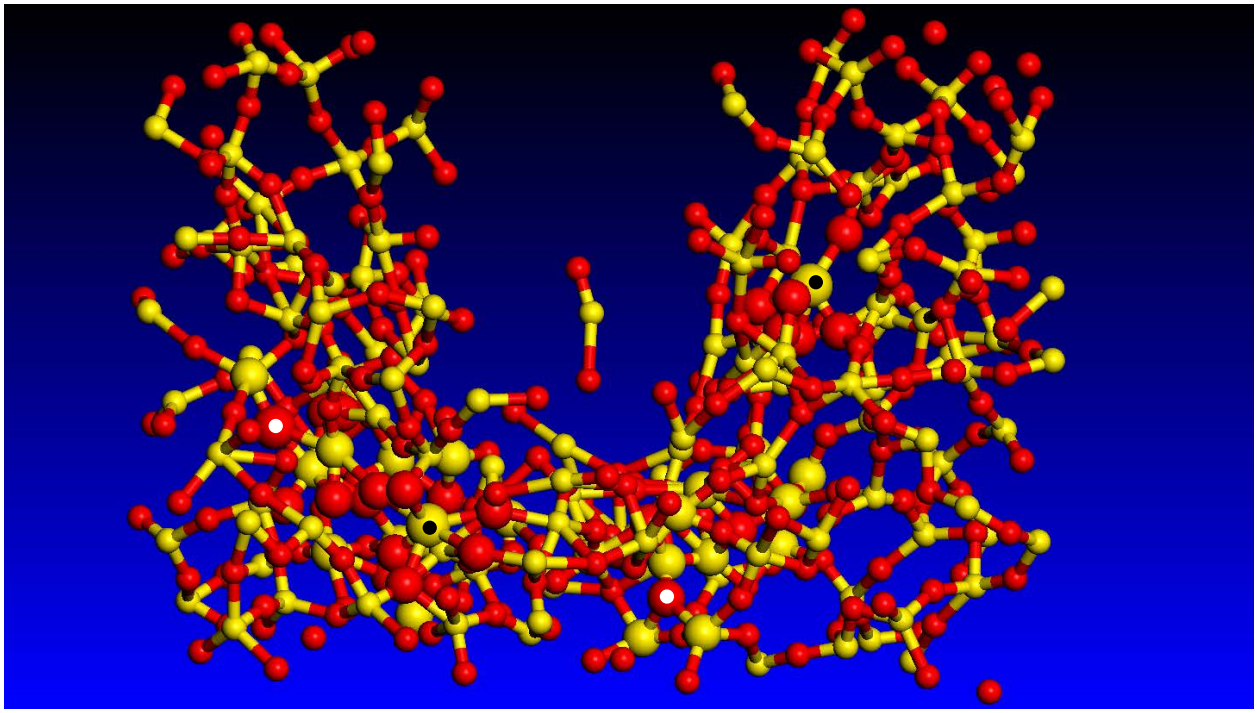

Figure 3-8 Local stishovite-like microstructure showing two six-folded Si and two three-folded O atoms. For clarity, a larger sphere radius is assigned to the atoms involved. In addition, six-folded Si atoms and three-folded O atoms are tagged with circular symbols.

Additional changes observed in the as-impacted fused silica pertain to the distribution of the smallest Si-O rings. To quantify the size-distribution of the smallest Si-O rings in both the initial and the as-impacted fused-silica states, a computational method was developed. This method solves the class of so-called "shortest path problems" and is a simple modification of the Dijkstra's algorithm [42, 43]. The main modifications in this algorithm are associated with the fact that, in the present case, the starting point and the destination point of the path are identical. The smallest-ring size-distribution results for the initial and as-impacted fused-silica states are displayed in Figures 3-9(a)–(b), respectively. Examination of these results reveals that ballistic impact alters the ring structure within fused silica. Specifically, while no five-membered rings were present in the initial state of fused silica, such rings are found in the as-impacted state of the same material. Additional changes observed pertain to the topology of the six-membered rings. That is, while in the initial state of fused silica these rings resemble the corresponding rings found in cristobalite (another allotropic modification of SiO_2), Figure 3-10(a), in the as-impacted fused silica the topology of the six-membered rings was found to resemble more that found in α-quartz, Figure 3-10(b).

Three partial radial distribution functions for the fused-silica target-plate after the diamond impactor has penetrated halfway through the target-plate thickness are depicted in Figure 3-11(a). A comparison of these results with their as-received fused-silica counterparts, Figure 3-5(a), reveals that the ballistic impact causes distinct changes in the short-range order and atomic coordination within this material. To help rationalize these changes, the same partial radial distribution functions are calculated for α-quartz, Figure 3-11(b), and stishovite, Figure 3-11(c). A comparison of the results displayed in Figures 3-5(a) and 3-11(a)–(c) further confirms that the ballistic impact-induced changes in the pair correlation functions are associated with the

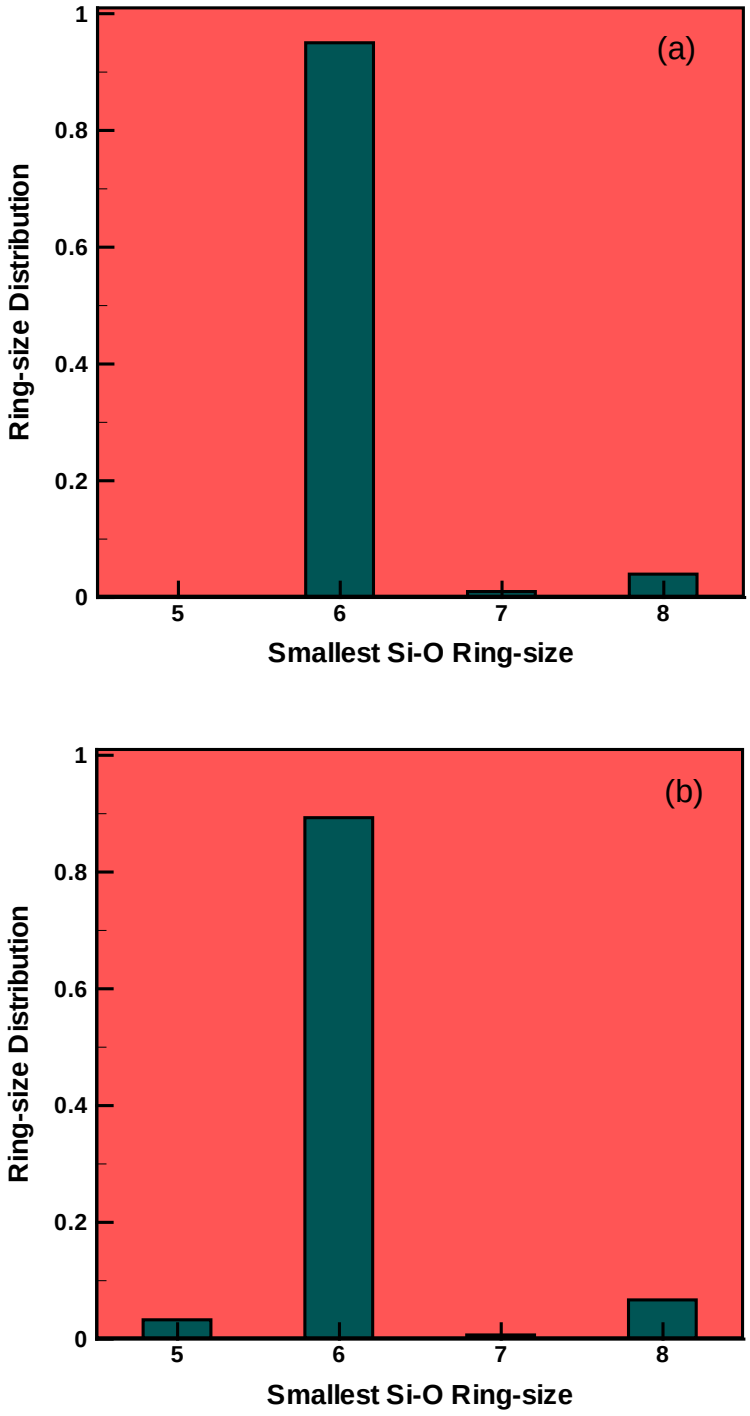

Figure 3-9 Size distribution function for the smallest Si-O rings in the fused-silica: (a) initial state; and (b) as-impacted state.

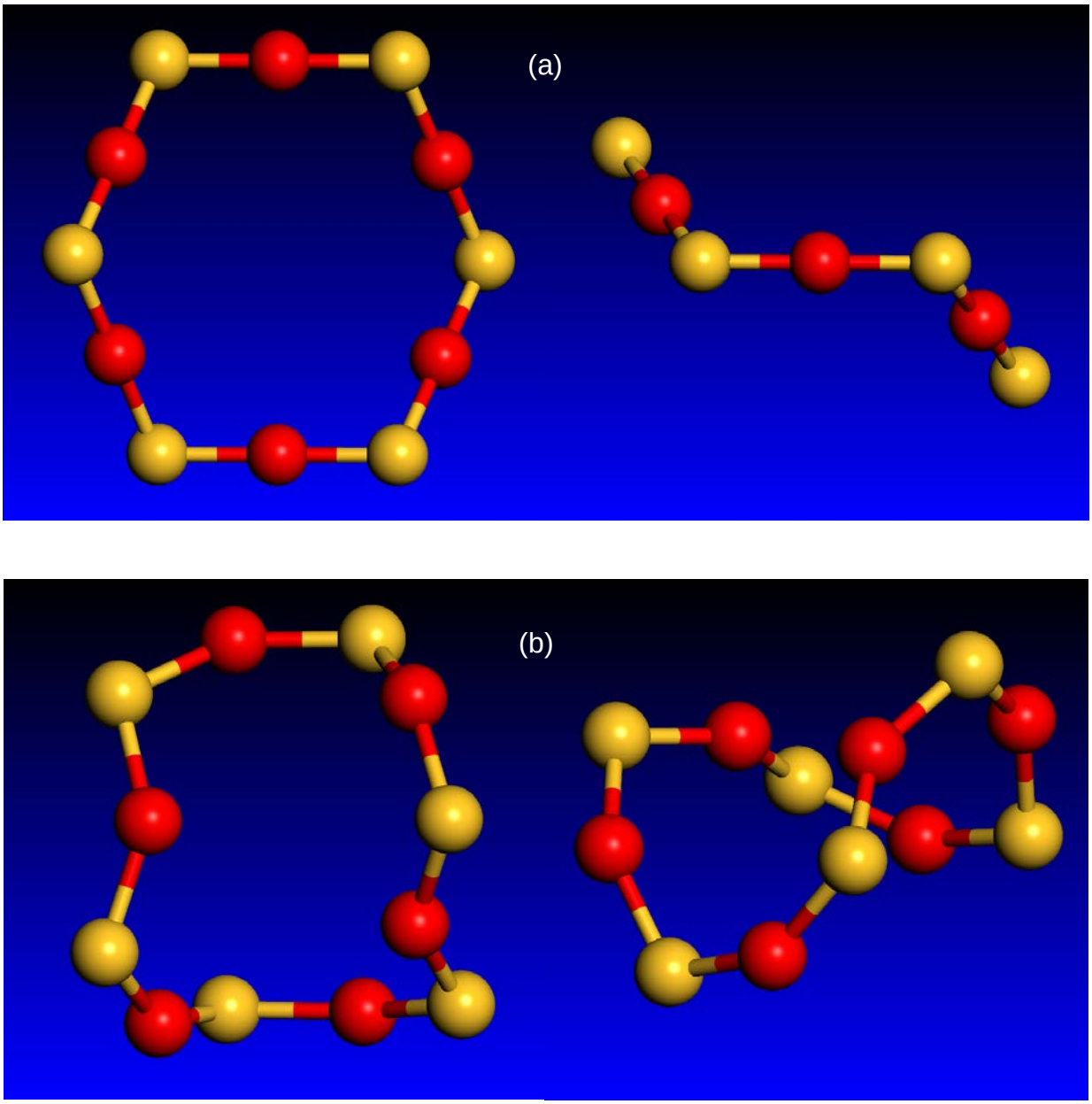

Figure 3-10 Two views of the atomic structure of six-membered Si-O rings in (a) cristobalite; and (b) α–quartz.

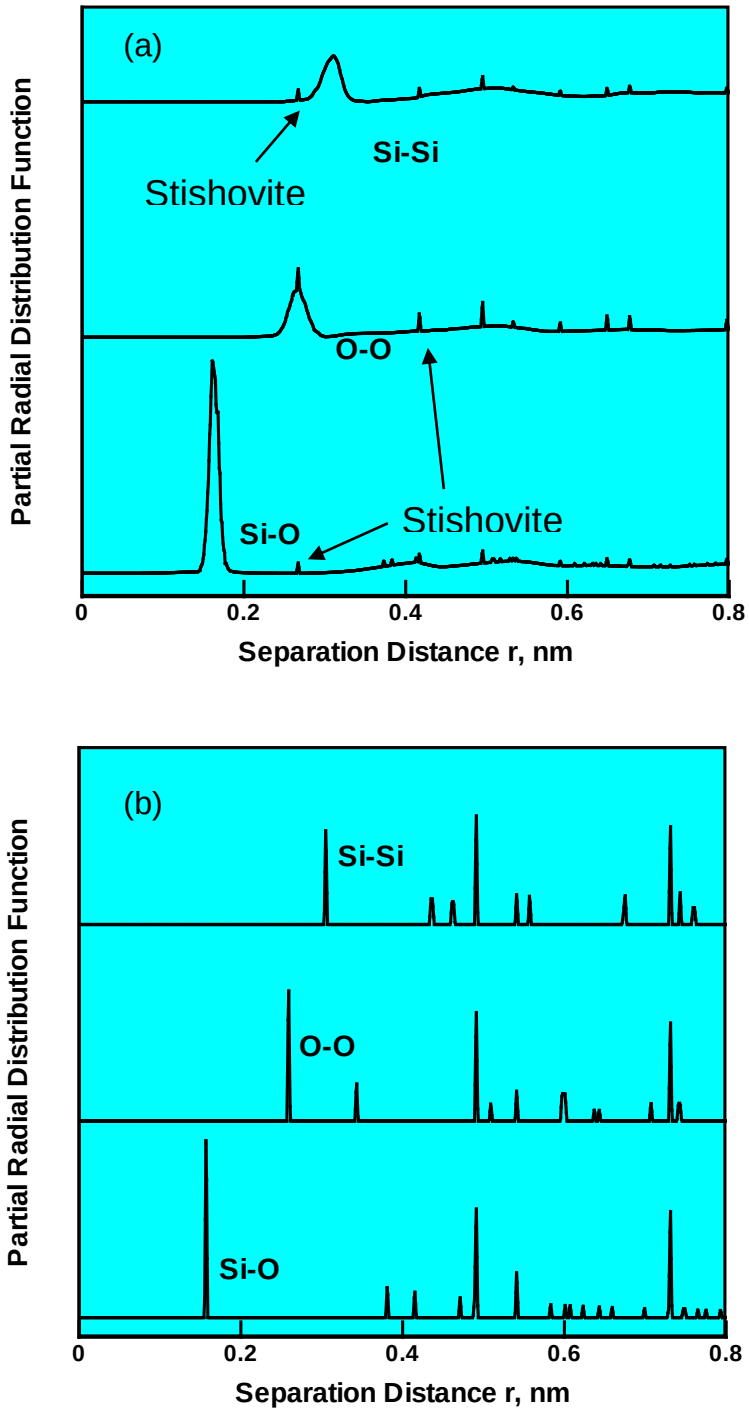

Figure 3-11 Three partial radial distribution functions for: (a) the fused-silica region adjacent to the projectile, after the diamond impactor has penetrated approximately halfway through the target-plate thickness; (b) α-quartz; and (c) stishovite.

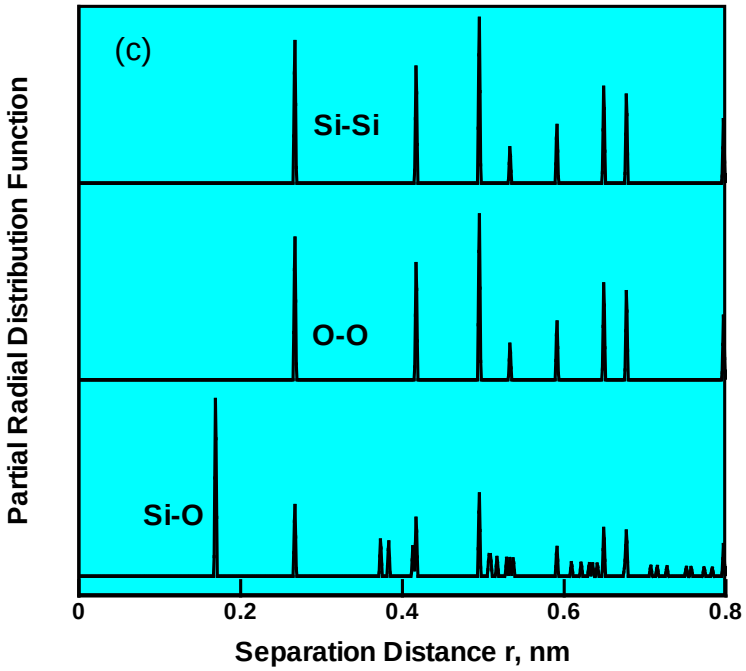

Figure 3-11 continued.

devitrification of fused-silica, and the formation of α-quartz and stishovite. In other words, differences in the partial pair correlation functions in the as-impacted fused silica relative to those in the as-received fused silica appear to be caused by the presence of Si-Si, Si-O and O-O atomic pairs with an atomic environment similar to those found in stishovite (and α-quartz).

To further demonstrate the conversion of fused-silica to stishovite as a result of the ballistic impact, Si- and O-atom coordinations in the fused-silica region surrounding the penetration hole are determined. The results of this procedure, labeled "As-impacted State," are shown in Figures 3-6(a)–(b). Examination of the results displayed in these figures reveals the presence of six-coordinated Si and three-coordinated O atoms, the atomic coordination which characterizes the stishovite crystal structure.

3.5.3 Relative Stability of Fused Silica, α-Quartz and Stishovite

To further help rationalize the changes in the partial pair correlation functions induced by the ballistic impact, the quantum-mechanical DFT calculation results pertaining to the relative stability of fused silica, α-quartz and stishovite, as well as of the energy barriers associated with the fused-silica → α-quartz and fused-silica → stishovite transition states, are presented and discussed in this section. The relative room-temperature potential energies of the fused silica, α-quartz and stishovite as a function of pressure are presented in Figure 3-12(a). Examination of the results displayed in this figure reveals that, at the ambient pressure, α-quartz is the most stable form of SiO_2, followed by fused silica and then by stishovite. At a pressure of 50 GPa, on the other hand, the relative positions of α-quartz and fused silica, with respect to thermodynamic stability, have been exchanged.

In Figure 3-12(b), the relative room-temperature potential energies of the fused silica, α-quartz and stishovite as a function of pressure, in the presence of 5% shear, are presented. A comparison of the results displayed in Figures 3-12(a)–(b) reveals that, the application of 5% shear strain did not change the relative stability of fused silica, α-quartz and stishovite at the ambient pressure. In sharp contrast, at 50 GPa pressure, the application of 5% shear has been found to make the stishovite the most stable phase, followed by α-quartz and then fused silica. This finding suggests that, in the presence of shear, fused silica is more likely to undergo a devitrification conversion into stishovite and, to a lower extent, into α-quartz. This finding is important since the fused-silica region surrounding the projectile is generally subjected to high shear, in addition to high pressures. This explains why in Figure 3-8, this region was found to undergo an extensive fused-silica → stishovite conversion.

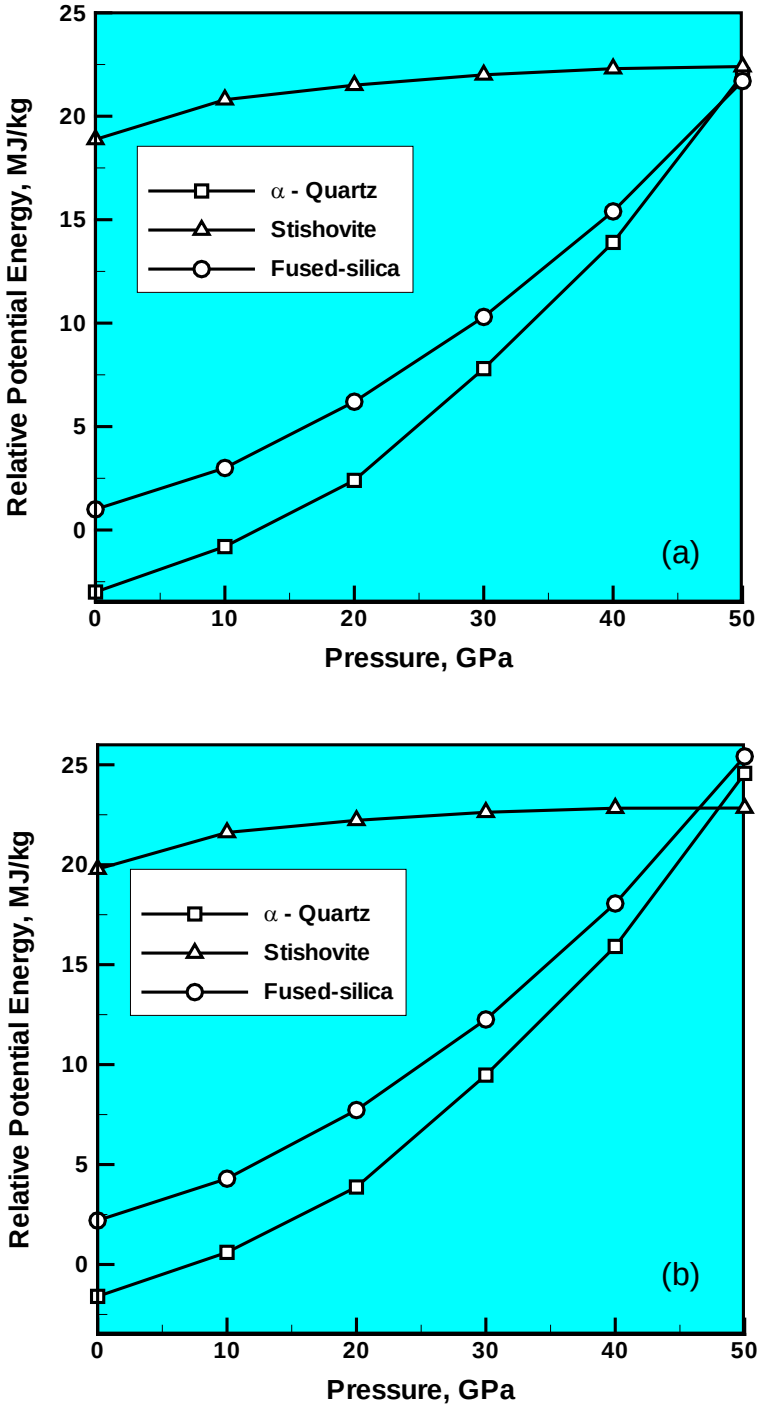

Figure 3-12 Relative room-temperature potential energies of fused silica, α-quartz and stishovite, as a function of pressure, in the: (a) absence; and (b) presence of 5% shear.

The likelihood for the aforementioned devitrification processes are affected not only by the relative stabilities of fused silica, α-quartz and stishovite, but also by the size of the energy barrier associated with the respective transition state. Variations in the fused-silica → α-quartz and fused-silica → stishovite transition-state energy barriers with pressure, in the absence and the presence of 5% shear, are shown respectively in Figures 3-13(a)–(b). Examination of the results displayed in these figures, at a pressure of 50 GPa, reveals that the energy barrier for fused-silica devitrification, in the absence of shear, is slightly higher for the fused-silica → stishovite conversion. On the other hand, the energy barrier for fused-silica devitrification, in the presence of shear, is slightly higher for the fused-silica → α-quartz conversion. These findings suggest that, in the presence of shear, and at pressures as high as 50 GPa, fused silica is more likely to convert to stishovite than α-quartz.

Figure 3-14 shows the conversion of an initially amorphous SiO_2 structure into a stishovite-like structure under the influence of high pressure and shear. The transition state associated with this conversion is also shown in this figure. For clarity, only a small SiO_2 region consisting of three Si and fifteen O atoms is displayed in Figure 3-14. Due to such a small size of the region, some O atoms appear to be non-bonded. These O atoms are bonded to Si atoms, but the Si atoms that they are bonded to are not shown in this figure. The Si atoms in question are also bonded to some of the bonded O atoms displayed in Figure 3-14. Examination of this figure reveals that, as expected, the fused-silica state contains only four-fold coordinated Si and two-fold coordinated O atoms, while the stishovite state contains six-fold coordinated Si and three-fold coordinated O atoms. The Si and O atom coordination in the transition state involves four-fold and five-fold coordinated Si and two-fold and three-fold coordinated O atoms. To help with the interpretation of the results displayed in Figure 3-14, the same three Si atoms appearing in the

three configurations are denoted using labels “Si 1”, “Si 2” and “Si 3”. It should be recalled that the results presented in Figures 3-13(a)-(b) reveal that the maximum energy associated with the transition state is lowered and, thus, the conversion of the fused-silica → stishovite becomes feasible, under high pressure and shear.

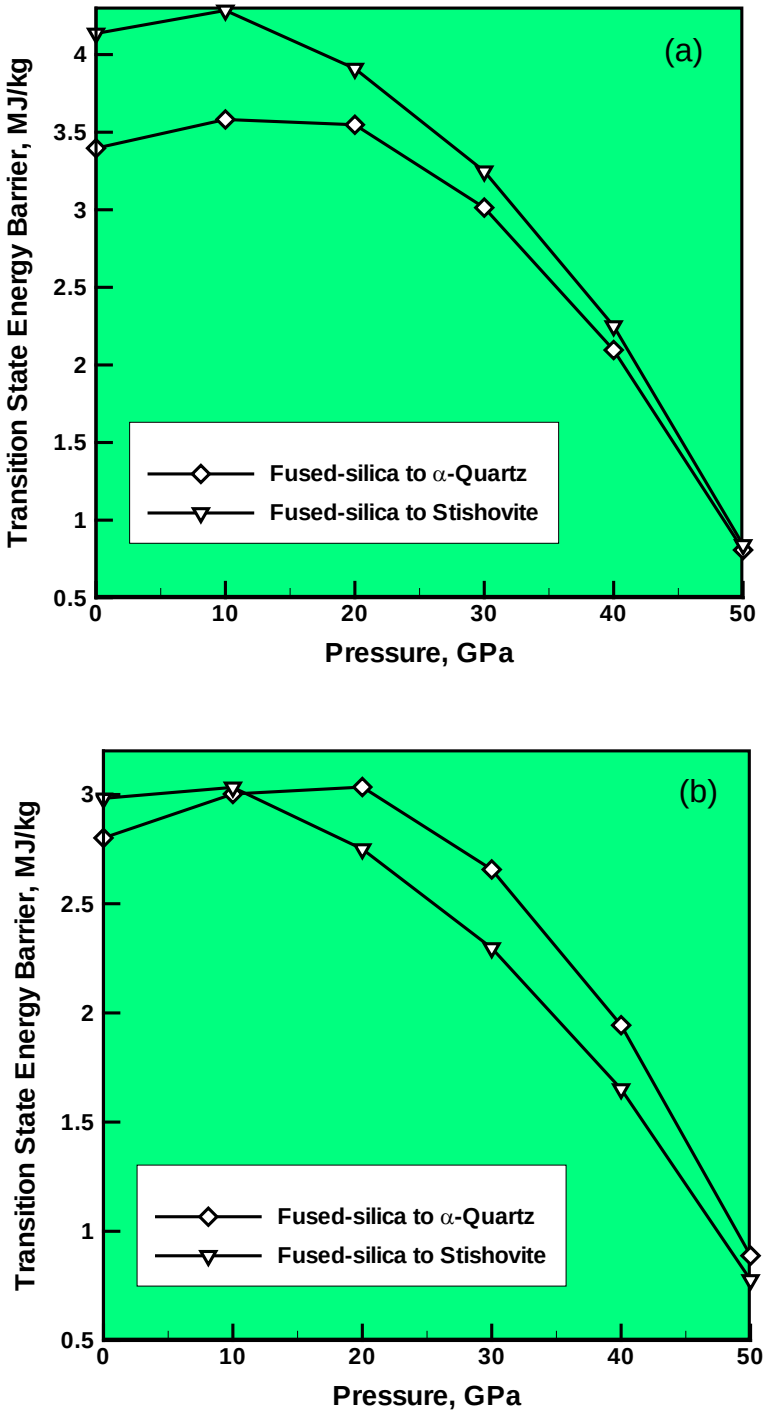

Figure 3-13 Variations in the fused-silica → α-quartz and fused-silica → stishovite transition-state energy barriers with pressure, in the: (a) absence; and (b) presence of 5% shear.

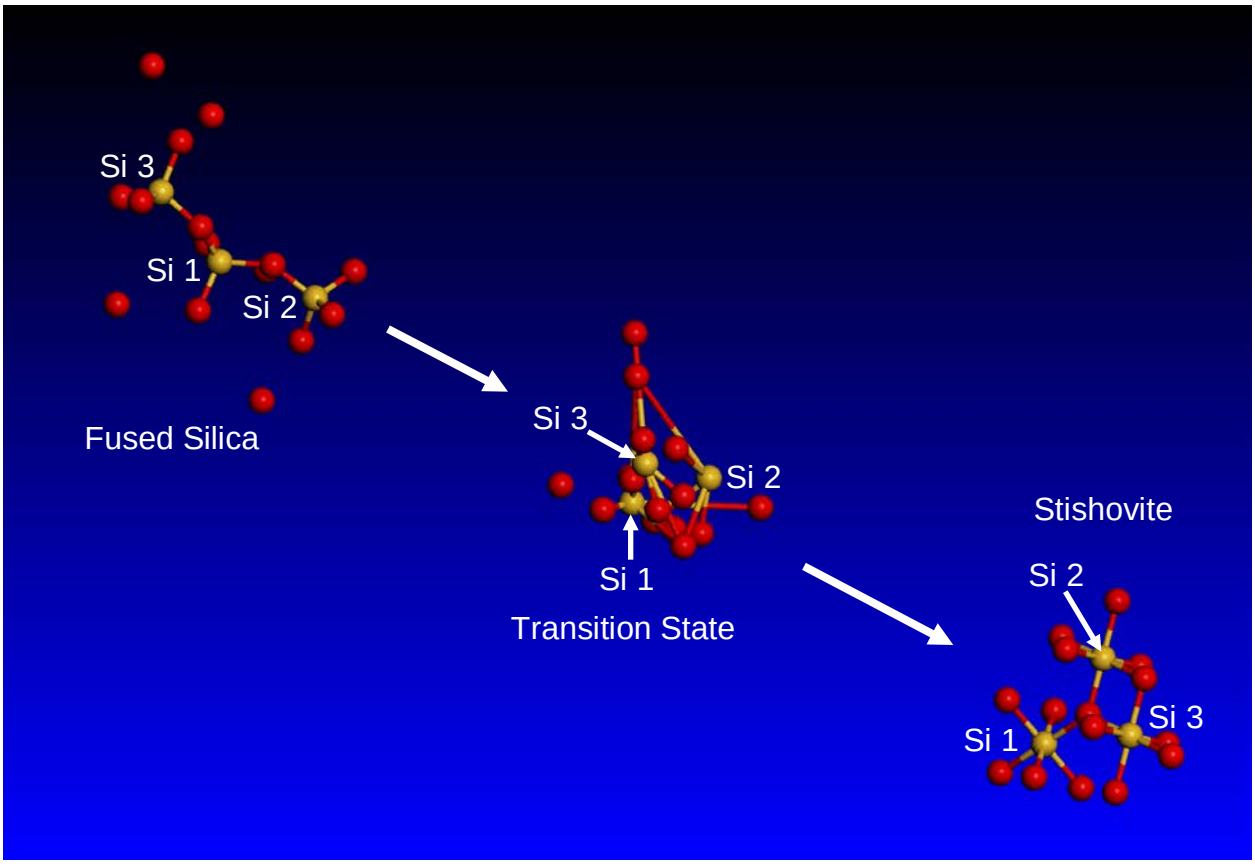

Figure 3-14 Conversion of an initially amorphous SiO_2 structure into a stishovite-like structure under the influence of high pressure and shear. The associated transition state is also shown.

3.6. Summary and Conclusions

Based on the results obtained in the present work, the following summary remarks and main conclusions can be drawn:

1. By determining the Si-Si, Si-O and O-O partial radial distribution functions, and the coordination numbers for Si and O atoms, before and after a ballistic impact experienced by a fused-silica target-plate, potential devitrification of the initial material and its conversion into α-quartz and stishovite are investigated.

2. The investigation is carried out computationally through the use of all-atom non-equilibrium molecular-dynamics simulations.

3. To rationalize the results obtained, quantum-mechanical density functional theory computational analyses are employed. These analyses helped establish the effect of high pressure and shear on the relative stability of the amorphous fused silica, crystalline α-quartz and crystalline stishovite, and on the energy barriers associated with the fused-silica → α-quartz and fused-silica → stishovite conversion reactions.

4. The results obtained demonstrated that under pressures on the order of 50 GPa, and in the presence of shear, stishovite becomes the most stable form of SiO_2 and the energy barrier associated with the fused-silica → stishovite conversion is the smallest. Since the fused-silica target-plate regions beneath and surrounding the hard projectile experience high pressures and shear, formation of stishovite and, to a lower extent, α-quartz from fused silica, as observed in the all-atom molecular-level computational analyses of the ballistic-impact problem, is justified.

3.7. References

1. W. D. Kingery, H. K. Bowen and D. R. Uhlmann, *Introduction to Ceramics*, 2nd ed., John Wiley & Sons: New York, 1976, 91–124.
2. C. S. Alexander, L.C. Chhabildas, W.D. Reinhart, D.W. Templeton, "*Changes to the shock response of quartz due to glass modification*," International Journal of Impact Engineering, 35: 1376–1385, 2008.
3. M. Grujicic, B. Pandurangan, N. Coutris, B. A. Cheeseman, C. Fountzoulas, P. Patel and E. Strassburger, "*A Ballistic Material Model for Starphire®, A Soda-lime Transparent Armor Glass*," Materials Science and Engineering A, 492: 397–411, 2008.
4. M. Grujicic, B. Pandurangan, W. C. Bell, N. Coutris, B. A. Cheeseman, C. Fountzoulas and P. Patel, "*An Improved Mechanical Material Model for Ballistic Soda-Lime Glass*," Journal of Materials Engineering and Performance, 18: 1012–1028, 2009.
5. M. Grujicic, B. Pandurangan, N. Coutris, B. A. Cheeseman, C. Fountzoulas and P. Patel, "*A Simple Ballistic Material Model for Soda-Lime Glass*," International Journal of Impact Engineering, 36: 386–401, 2009.
6. M. Grujicic, W. C. Bell, P. S. Glomski, B. Pandurangan, B. A. Cheeseman, C. Fountzoulas, P. Patel, D. W. Templeton and K. D. Bishnoi, "*Multi-length Scale Modeling of High-pressure Induced Phase Transformations in Soda-lime Glass*," Journal of Materials Engineering and Performance, 20: 1144–1156, 2011.
7. M. Grujicic, W. C. Bell, B. Pandurangan, B. A. Cheeseman, C. Fountzoulas and P. Patel, "*Molecular-Level Simulations of Shock Generation and Propagation in Soda-Lime Glass*," Journal of Materials Engineering and Performance, 21: 1580–1590, 2012.
8. M. Grujicic, W. C. Bell, B. Pandurangan, B. A. Cheeseman, C. Fountzoulas and P. Patel, "*The Effect of High-pressure Densification on Ballistic-penetration Resistance of Soda-lime Glass*," Journal of Materials: Design and Applications, 225: 298–315, 2011.
9. M. Grujicic, B. Pandurangan, Z. Zhang, W. C. Bell, G. A. Gazonas, P. Patel and B. A. Cheeseman, "*Molecular-Level Analysis of Shock-wave Physics and Derivation of the Hugoniot Relations for Fused Silica*," Journal of Materials Engineering and Performance, 21: 823–836, 2012.
10. M. Grujicic, W. C. Bell, B. Pandurangan, B. A. Cheeseman, P. Patel, and P. G. Dehmer, "*Effect of the tin- vs. air-side plate-glass orientation on the impact response and penetration resistance of a laminated transparent-armor structure*," Journal of Materials Design and Applications, vol. 226, pp. 119-143, 2012.
11. M. Grujicic, W. C. Bell, B. Pandurangan, B. A. Cheeseman, P. Patel, and G. A. Gazonas, "*Inclusion of material non-linearity and inelasticity into a continuum-level material model for soda- lime glass*," Materials & Design, vol. 35, pp. 144-155, 2012.
12. M. Grujicic, B. Pandurangan, T. He, B. A. Cheeseman, C.F. Yen, and C. L. Randow, "*Computational investigation of impact energy absorption capability of polyurea*

coatings via deformation-induced glass transition," Materials Science and Engineering A, vol. 527, no. 29-30, pp. 7741-7751, 2010

13. M. Grujicic, R. Yavari, J. Snipes, S. Ramaswami, and R. Barsoum, "*All-atom molecular-level computational simulations of planar longitudinal shockwave interactions with polyurea, soda-lime glass and polyurea/glass interfaces*," Multidiscipline Modeling in Materials and Structures, vol. 10, no. 4, pp. 474-510, 2014
14. M. Grujicic, R. Yavari, J. S. Snipes, S. Ramaswami, and R.Barsoum, "*All-atom molecular-level computational analyses of polyurea/fused-silica interfacial decohesion caused by imping- ing tensile stress-waves*," International Journal of Structural Integrity, vol. 5, no. 4, pp. 339-367, 2014
15. R. Chakraborty, A. Dey and A. K. Mukhopadhyay, "*Loading Rate Effect on Nanohardness of Soda-Lime-Silica Glass*," Metallurgical and Materials Transactions A, 41: 1301 – 1312, 2010.
16. O. Tschauner, S-N Luo, P. D. Asimow and T. J. Ahrens, "*Recovery of stishovite-structure at ambient conditions out of shock-generated amorphous silica*," American Mineralogist, 91: 1857–1862, 2006.
17. Salleo, S. T. Taylor, M. C. Martin, W. R. Panero, R. Jeanloz, T. Sands and F. Y. Génin, "*Laser-driven formation of a high-pressure phase in amorphous silica*," Nature Materials, 2: 796–800, 2003.
18. Mantisi, A. Tanguy, G. Kermouche, and E. Barthel, "*Atomistic response of a model silica glass under shear and pressure*," European Physical Journal B, 85: 304–316, 2012.
19. Kubota, M.-J. Caturla, L. Davila, J. Stolken, B. Sadigh, A. Quong, A. Rubenchik and M. D. Feit, "*Atomistic response of a model silica glass under shear and pressure*," Laser-Induced Damage in Optical Materials 2001, G. J. Exarhos, A. H. Guenther, K. L. Lewis, M. J. Soileau, C. J. Stolz, Editors, Proceedings of SPIE Vol. 4679 (2002), pp. 108–116.
20. http://accelrys.com/products/datasheets/materials-visualizer.pdf, accessed August 20, 2014.
21. Y. H. Tu, J. Tersoff, G. Grinstein, D. Vanderbilt, "*Properties of a Continuous-random-network Model for Amorphous Systems*," Physical Review Letters, 81: 1998, 4899–4902.
22. S. Nosé, "*Constant Temperature Molecular Dynamics Methods*," Progress in Theoretical Physics Supplement, 103: 1–46, 1991.
23. M. Grujicic, G. Cao and R. Singh, "*The Effect of Topological Defects and Oxygen Adsorbates on the Electronic Transport Properties of Single-Walled Carbon Nanotubes*", Applied Surface Science, 211: 166–183, 2003.
24. H. Sun, "*COMPASS: An ab Initio Force-Field Optimized for Condensed-Phase Applications Overview with Details on Alkane and Benzene Compounds*," Journal of Physical Chemistry B, 102: 7338–7364, 1998.
25. H. Sun, P. Ren, and J. R. Fried, "*The COMPASS force field: Parameterization and Validation for Phosphazenes*," Computational and Theoretical Polymer Science, 8: 229–246, 1998.

26. M. Grujicic, Y. P. Sun and K. L. Koudela, "*The Effect of Covalent Functionalization of Carbon Nanotube Reinforcements on the Atomic-level Mechanical Properties of Poly-Vinyl-Ester-Epoxy*," Applied Surface Science, 253: 3009–3021, 2007.

27. http://accelrys.com/products/datasheets/discover.pdf, accessed August 21, 2014.

28. http://accelrys.com/products/datasheets/dmol3.pdf, accessed August 21, 2014.

29. W. J. Hehre, *Ab Initio Molecular Theory*, Wiley: New York, 1986.

30. W. Kohn and L. J. Sham, "*Self-Consistent Equations Including Exchange and Correlation Effects*," Phys. Rev., 140: A1133–1138, 1965.

31. M. Grujicic, G. Cao, A. M. Rao, T. M. Tritt and S. Nayak, "*UV-Light Enhanced Oxidation of Carbon Nanotubes Through Adsorption of Polar Molecules*," Applied Surface Science, 214: 289–303, 2003.

32. M. Grujicic, V. Chenna, R. Yavari, R. Galgalikar, J. S. Snipes, and S. Ramaswami, "*Multi-length scale computational analysis of roller-bearing premature failure in horizontal-axis wind- turbine gear-boxes*," International Journal of Structural Integrity, vol. 5, no. 1, pp. 40-72, 2015

33. J. P. Perdew, K. Burke and M. Ernzerhof, "*Generalized Gradient Approximation Made Simple*," Physical Review Letters, 77: 3865–3868, 1996. Erratum Physical Review Letters, 78: 1396, 1997.

34. G. Henkelman, and H. Jonsson, "*Improved tangent estimate in the nudged elastic band method for finding energy paths and saddle points*," Journal of Chemical Physics, 113: 9978–9985, 2000.

35. T. A. Halgren and W. N. Lipscomb, "*The synchronous-transit method for determining reaction pathways and locating molecular transition states*," Chemical Physics Letters, 49: 225–232, 1977.

36. H. J. C. Berendsen, J. P. M. Postma, W. F. van Gunsteren, A. DiNola and J. R. Haak, "*Molecular Dynamics with Coupling to an External Bath*," Journal of Chemical Physics, 81: 3684–3690, 1984.

37. M. Grujicic, K. M. Chittajallu, G. Cao and W. N. Roy, "*An Atomic Level Analysis of Conductivity and Strength in Poly (Ethylene Oxide) Sulfonic Acid Based Solid Polymer Electrolytes*", Materials Science and Engineering B, 117: 187–197, 2005.

38. A. Tilocca, N. H. de Leeuw and A. N. Cormack, "*Shell-model Molecular Dynamics Calculations of Modified Silicate Glasses*," Physical Reviews B, 73: 104209(14), 2006.

39. M. Grujicic, B. Pandurangan, and N. Coutris, "*A computational investigation of the multi-hit ballistic-protection performance of laminated transparent-armor systems*," Journal of Materials Engineering and Performance, vol. 21, no. 6, pp. 837-848, 2012.

40. M. Grujicic, W. C. Bell, and B. Pandurangan, "*Design and material selection guidelines and strategies for transparent armor systems*," Materials and Design, vol. 34, pp. 808-819, 2012.

41. M. Grujicic, B. Pandurangan, W. C. Bell, B. A. Cheeseman, P. Patel, and G. A. Gazonas, "*Molecular-level analysis of shock- wave physics and derivation of the Hugoniot relations for soda- lime glass*," Journal of Materials Science, vol. 46, no. 22, pp. 7298-7312, 2011.

42. A. Grujicic, M. Grujicic, R. Yavari, J. S. Snipes, and S. Ramaswami, "*Molecular and meso-scale computational analy- ses of microstructure and behavior of actin monomers, trimers and polymers*," International Journal of Biological Sciences and Applications, vol. 1, no. 1, pp. 90-112, 2014.

43. E. W. Dijkstra, "*A Note on Two Problems in Connexion with Graphs*," Numerische Mathematik, 1, 1959, 269-271.

CHAPTER 4: THE EFFECT OF HIGH-PRESSURE DEVITRIFICATION AND DENSIFICATION ON BALLISTIC-PENETRATION RESISTANCE OF FUSED SILICA

4.1. Abstract

Recent experimental and molecular-level computational analyses have indicated that fused silica, when subjected to pressures of several tens of GPa, can experience irreversible devitrification and densification. Such changes in the fused-silica molecular-level structure are associated with absorption and/or dissipation of the strain energy acquired by fused silica during high-pressure compression. This finding may have important practical consequences in applications for fused silica such as windshields and windows of military vehicles, portholes in ships, ground vehicles and spacecraft, etc. In the present work, our prior molecular-level computational results pertaining to the response of fused silica to high pressures (and shear stresses) are used to enrich a continuum-type constitutive model (that is, the so-called Johnson-Holmquist-2, JH2, model) for this material. Since the aforementioned devitrification and permanent-densification processes modify the response of fused silica to the pressure as well as to the deviatoric part of the stress, changes had to be made in both the JH2 equation of state and the strength model. To assess the potential improvements in respect to the ballistic-penetration resistance of this material brought about by the fused-silica devitrification and permanent-densification processes, a series of transient non-linear dynamics finite element analyses of the transverse impact of a fused-silica test plate with a solid right-circular cylindrical steel projectile was conducted. The results obtained revealed that, provided the projectile incident velocity and, hence, the attendant pressure, is sufficiently high, fused silica can undergo impact-induced devitrification, which improves its ballistic penetration resistance.

4.2. Introduction

The present work deals with computational modeling and simulations of the devitrification/crystallization and permanent densification of fused silica (a transparent-armor material) under ballistic-impact conditions, and the associated increase in the fused-silica ballistic limit. Hence, the main aspects of the present work include: (a) current reputation and standing of ceramic glasses like fused-silica as transparent-armor materials; (b) microstructure of fused-silica, main SiO_2 crystalline polymorphs, and glass devitrification/crystallization under high imposed pressures; and (c) prior experimental; and (d) prior computational efforts dealing with the analysis of fused-silica devitrification under high pressures. A brief overview of these aspects of the problem at hand is presented in the remainder of this section.

4.2.1 Ceramic Glasses as Transparent-Armor Materials

Currently, a number of materials and design strategies are employed in transparent, ballistic-impact-resistant vehicle structures (e.g. windshields, door windows, viewports, etc.). Among the most recently introduced transparent materials and technologies, the following have received the most attention: (a) transparent crystalline ceramics (e.g. aluminum-oxinitride spinel, AlON, sapphire [1]); (b) new transparent polymer materials (e.g. transparent nylon [2]); (c) new interlayer technologies (e.g. polyurethane bonding layers [3]); and (d) new laminate structure designs [e.g. 4]. Despite the clear benefits offered by these materials and technologies (e.g. transparent ceramics offer a very attractive combination of high stiffness and high hardness levels, highly ductile transparent polymers provide superior fragment containing capabilities, etc.), ballistic ceramic glass like fused-silica remains an important constituent material in a majority of transparent impact-resistant structures used today. Among the main reasons for the wide-scale use of glass, the following three are most frequently cited: (i) glass-structure fabrication technologies enable the production of curved, large surface-area, transparent structures with thickness approaching several inches; (ii) relatively low material and manufacturing costs; and (iii) compositional modifications, chemical strengthening, and controlled crystallization have been demonstrated to be capable of significantly improving the ballistic properties of glass [e.g. 2].

4.2.2 Fused-Silica, SiO_2 Polymorphs, and High-Pressure Devitrification

Ceramic glasses are amorphous materials. The molecular-level microstructure of these materials involves entities such as a random network of covalently bonded atoms, atomic free volumes, network-forming atoms (e.g. Si), bridging and non-bridging oxygen atoms, cations of glass-modifier species, etc. However, despite the absence of a crystalline structure, the microstructure of ceramic glasses is not completely random. Rather, it involves different extents of short- and intermediate-range order spanning over a range of length-scales (from the quantum-mechanical to the continuum-level). To describe the structure of ceramic glasses as determined using various experimental techniques (e.g. neutron-diffraction, nuclear magnetic resonance, small angle X-ray scattering (SAXS), etc.), the so-called ***random network model*** [5] is typically employed. Such a model represents an amorphous material as a three-dimensional linked network of polyhedra. The character (number of facets) of the polyhedra is controlled by the species-specific coordination of the central (glass-forming) atom (cation). In fused silica, the polyhedron-center atoms are all silicon and each silicon atom is surrounded by four oxygen atoms (while each oxygen atom is connected to or bridges two silicon atoms, i.e. all oxygen atoms are of a bridging type), forming a network of SiO_4^{4-} tetrahedra. Other silicate-based glasses contain network modifiers (alkali or alkaline earth oxides) which compromise the continuity of the network and introduce non-bridging oxygen anions.

Within the random network model, the microstructure of glass is described using several network-state parameters. A detailed description of these parameters, as well as the experimental/computational procedures which are commonly employed to determine these parameters, can be found in our prior work [6]. Previous investigations [e.g. 6–15] established

that under high-rate (shockwave or ballistic) loading conditions, fused-silica targets can, at least in the vicinity of the impact region, experience transformation of the amorphous structure into a crystalline one. To help rationalize potential transformations of fused silica into various (crystalline) polymorphs of SiO_2, the corresponding temperature-pressure phase diagram and the SiO_2 polymorphs were analyzed in our prior work [16]. The analysis established that under ballistic-impact loading conditions and the accompanying adiabatic temperatures, the following three polymorphs have the highest probability of forming during the impact-induced devitrification process:

(i) α-quartz – Structure: Trigonal; Space Group: $P3_221$ (No. 154); Lattice parameters: $a=b$=4.9137 Å, c=5.4047 Å, $\alpha=\beta$=90.0°, γ=120.0°, Z=3 (where Z is the number of SiO_2 units within the unit cell); Mass density: 2.66 g/cm^3. The atomic arrangement within the non-primitive unit cell of α-quartz is depicted in Figure 4-1(a).

(ii) Coesite – Structure: Monoclinic; Space group: C2/c; Lattice parameters: a = 7.1356 Å, b = 12.3692 Å, c = 7.1736 Å; α=90.0°, β = 120.34°, γ=90.0°, Z = 16; Mass density: 2.92 g/cm^3. The atomic arrangement within the non-primitive unit cell of coesite is depicted in Figure 4-1(b).

(iii) Stishovite – Structure: Tetragonal (ditetragonal dipyramidal); Space group: P 4_2/mnm (No. 136) $P4_2/mnm$ {$P4_2/m\ 2_1/n\ 2/m$}; Lattice parameters: $a = b$ = 4.179 Å, c = 2.6649 Å, Z=2; Mass density: 4.29 g/cm^3. The atomic arrangement within the non-primitive unit cell of stishovite is depicted in Figure 4-1(c).

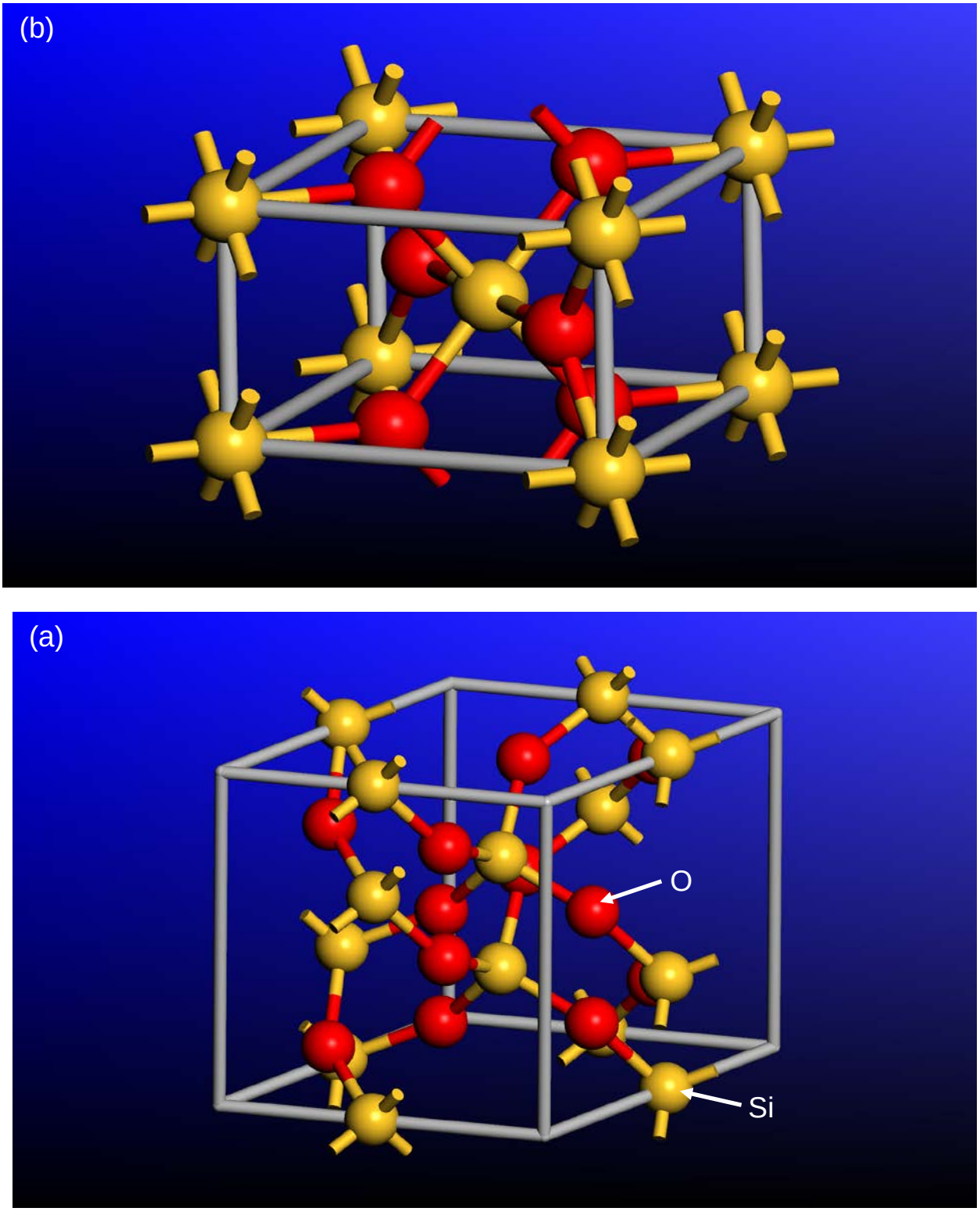

Figure 4-1 The atomic arrangements within the non-primitive unit cells of: (a) α-quartz; (b) stishovite; and (c) coesite.

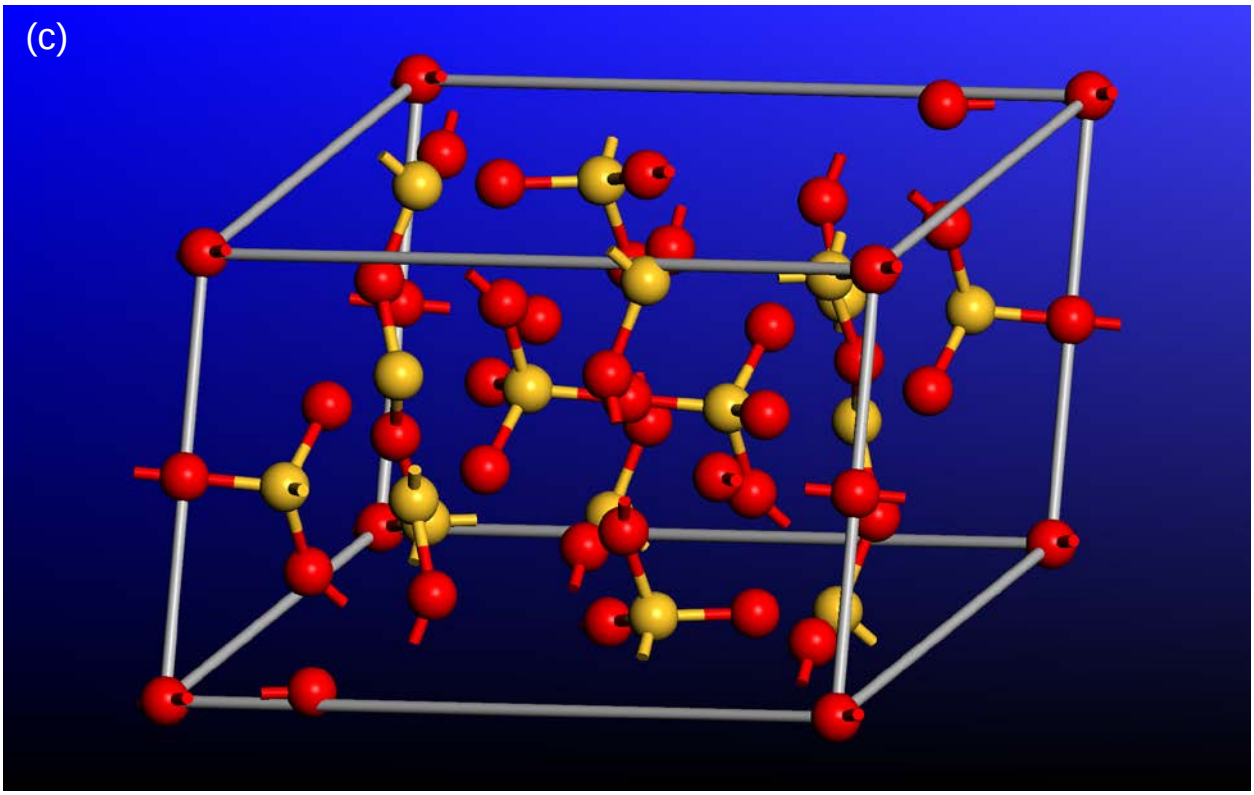

Figure 4-1 continued.

4.2.3 Prior Experimental Work

A detailed overview of the public-domain literature carried out as part of the present work revealed a number of experimental investigations dealing with the mechanical response of fused silica to dynamic loading. Some of these studies revealed the formation of shear bands within otherwise amorphous glass, others established the formation of crystalline phases (α-quartz and stishovite, but not coesite), while still others demonstrated increased hardness of the material surrounding the impact region without establishing the microstructural cause for this property change.

Chakraborty et al. [17] carried out a series of nano-indentation tests and showed that, as the loading rate increases, the extent of shear band formation in the region surrounding the indentation decreases, while the hardness value increases. No crystal-structure analysis was carried out to determine potential formation of any of the crystalline phases as a result of loading or to provide a rationale for the observed effect of the loading rate.

Tschauner et al. [18] investigated formation of stishovite in soda-lime glass during 57 GPa shock loading experiments and the reversion of this phase during subsequent release/unloading. They demonstrated that upon loading, high-density non-fully-crystallized SiO_2 phase was present in the "shocked" fused-silica. Upon static loading to only 13 GPa, this phase was fully converted into the crystalline stishovite, suggesting that the shock loading was able to devitrify fused silica and form crystalline stishovite.

Salleo et al. [19] demonstrated the formation of a defective form of stishovite in the surface region of fused-silica wafers through irradiation with a high-powered laser. The

formation of such a phase and its continuous growth has been found to be the main cause of failure in optics used for high-power photonics.

4.2.4 Prior Computational Work

A detailed overview of the public-domain literature carried out as part of the present work also revealed three computational investigations dealing with the mechanical response of fused silica to dynamic loading.

Mantisi et al. [20] carried out a comprehensive atomic-scale simulation of fused silica under combined pressure/shear loading conditions. The results obtained established permanent/irreversible densification of the fused silica test sample and the change of the silicon and oxygen coordination relative to that present in the as-received fused silica. However, these microstructural changes could not be considered to be the result of glass devitrification/crystallization processes, i.e. the glass remained amorphous. One of the potential reasons for this observation was inadequacy of the interatomic potentials used in the simulation of the fused-silica mechanical behavior.

Kubota et al. [21] used molecular dynamics simulations to infer the atomic-scale structural changes in fused silica induced by shock-compression loading. The results obtained revealed that shock-compressive loading involving stress levels exceeding the Hugoniot Elastic Limit, gives rise to dramatic changes in the structure and topology of the fused-silica network and densifications of in excess of 20%. Coordination analysis of the as-shocked fused silica revealed the formation of under- and over-coordinated Si atoms. While under-coordinated Si atom regions could be interpreted as shock-induced fused-silica flaws, over-coordinated Si atom regions showed some resemblance to the crystalline stishovite. In addition to the coordination changes just described, changes in glass topology (such as increases in the number of the three-fold, four-fold, seven-fold and larger rings) were observed.

Grujicic et al. [16] carried out an all-atom molecular-level computation of the dynamic response and material microstructure/topology changes of fused silica subjected to ballistic impact by a hard projectile. The results obtained clearly revealed the formation of stishovite (and perhaps α-quartz) within fused silica during ballistic impact. To rationalize the findings obtained, the all-atom molecular-level computational analysis was complemented by a series of quantum-mechanics density functional theory (DFT) computations. The latter computations enabled determination of the relative potential energies of the fused silica, α-quartz and stishovite under ambient pressure (i.e. under their natural densities) as well as under imposed (as high as 50 GPa) pressures (i.e. under higher densities) and shear strains. In addition, the transition states associated with various fused-silica devitrification processes were identified.

4.2.4 Main Objectives

The main objective of the present work is to utilize the atomic-scale and quantum-mechanical-scale results obtained in our recent work [16] regarding the devitrification of fused silica under ballistic-impact conditions in order to enrich and upgrade a continuum-level material model for the same material. Once such material-model enrichment/upgrading is completed and the model is implemented into a material-user subroutine and linked with a finite-element solver, it is used, within a transient nonlinear dynamics finite-element analysis, to investigate the response of a fused-silica target-plate to a normal (i.e. zero-obliquity angle) impact by an armor-piercing bullet. By turning off and on the glass-devitrification process, such analysis will enable quantification of the ballistic-impact improvement brought about by the formation of high-density crystalline polymorphs of SiO_2 from fused silica during a ballistic impact.

4.2.5 Paper Organization

A summary of the molecular- and quantum-mechanics-level computational results (the results used in the present work) regarding the response of fused silica to high-pressure/-shear loading is presented in Chapter 4-2. A brief overview of the original JH2 material model and its proposed modifications is given in Chapter 4-3. Details regarding the transient non-linear dynamics finite-element analysis of impact of a fused-silica target-plate by an armor-piercing bullet, the results obtained and interpretation of the results are all presented in Chapter 4-4. A summary of the main findings and conclusions is provided in Chapter 4-5.

4.3. Summary of Main Results from Ref. [16]

Since the present work utilizes many of the (atomic-scale and quantum-mechanics) results reported in our recent work [16], a brief summary of these results is given in this section. For improved clarity, this summary is divided into several subsections.

4.3.1 Validation of the Fused-Silica Atomic-Scale Material Model

To validate the atomic-scale model for fused silica, a number of model predictions are compared with either their experimental or with their more accurate quantum-mechanical computational counterparts. The material characteristics used in this validation procedure include room-temperature and ambient-pressure: (a) mass density; (b) partial radial distribution functions for the three (Si-Si, Si-O and O-O) atomic pairs; and (c) distributions of the Si-atom and O-atom coordination numbers. The level of agreement obtained indicated that the computational unit-cell used to represent the amorphous structure of fused silica, and the force-field potentials used to quantify various bonding and non-bonding interactions within the computational cell, account quite well for the natural state of densification, for the short-range order, and for the coordination environment within fused silica.

4.3.2 Ballistic-Impact-Induced Fused-Silica Devitrification

In Ref. [16], atomic-scale simulations were carried out of the impact of a fused-silica target-plate by a diamond solid right-circular cylindrical projectile. Examples of such results as a function of the post-initial-contact time are depicted in Figures 4-2(a)–(d). In these figures, for improved clarity, the symbols for the target-plate atoms are made smaller. Examination of the results displayed in Figures 4-2(a)–(d) reveals that the target-plate material in the close vicinity of the projectile experiences major changes. Detailed examination of the regions of the target experiencing such changes revealed:

(a) the presence of numerous six-folded Si and three-folded O atoms (the Si and O coordinations characteristic of stishovite and not of fused silica). Local stishovite-like microstructure showing two six-folded Si and two three-folded O atoms is shown in Figure 4-3(a). For clarity, a larger sphere radius is assigned to the atoms involved. In addition, six-folded Si atoms and three-folded O atoms are tagged with circular symbols. Since the initial state of fused-silica only contained four-folded Si and two-folded O atoms, this result suggested that ballistic impact can lead, at least locally, to the conversion of amorphous SiO_2 into the crystalline (but highly deformed) stishovite structure;

(b) changes in the size distribution of the smallest/primitive Si-O rings (i.e. the rings which cannot be described as combinations of smaller rings). That is, while five-membered rings are found in the as-impacted fused silica, only larger rings were present in the initial state of this material. An example of the results pertaining to the size distribution function for the smallest Si-O rings in the fused-silica initial and as-impacted states is shown in Figure 4-3(b);

(c) changes in the Si-O ring topology. That is, while in the initial state of fused silica these rings resemble the corresponding rings found in cristobalite (another SiO_2 polymorph), in the as-impacted fused silica the topology of the six-membered rings was found to resemble more that found in α-quartz and stishovite;

(d) changes in the Si-Si, O-O, and Si-O partial pair correlation functions from those characteristic of amorphous materials found in the initial state of fused silica, Figure 4-3(c), to those found in the silica region adjacent to the penetration hole, Figure 4-3(d); and

(e) changes in the Si atomic coordination from 4 in the as-received fused silica to approximately 6 in the fused-silica region affected by the ballistic impact, as well as changes in the O atomic coordination from 2 in the as-received fused silica to approximately 3 in the same fused-silica region.

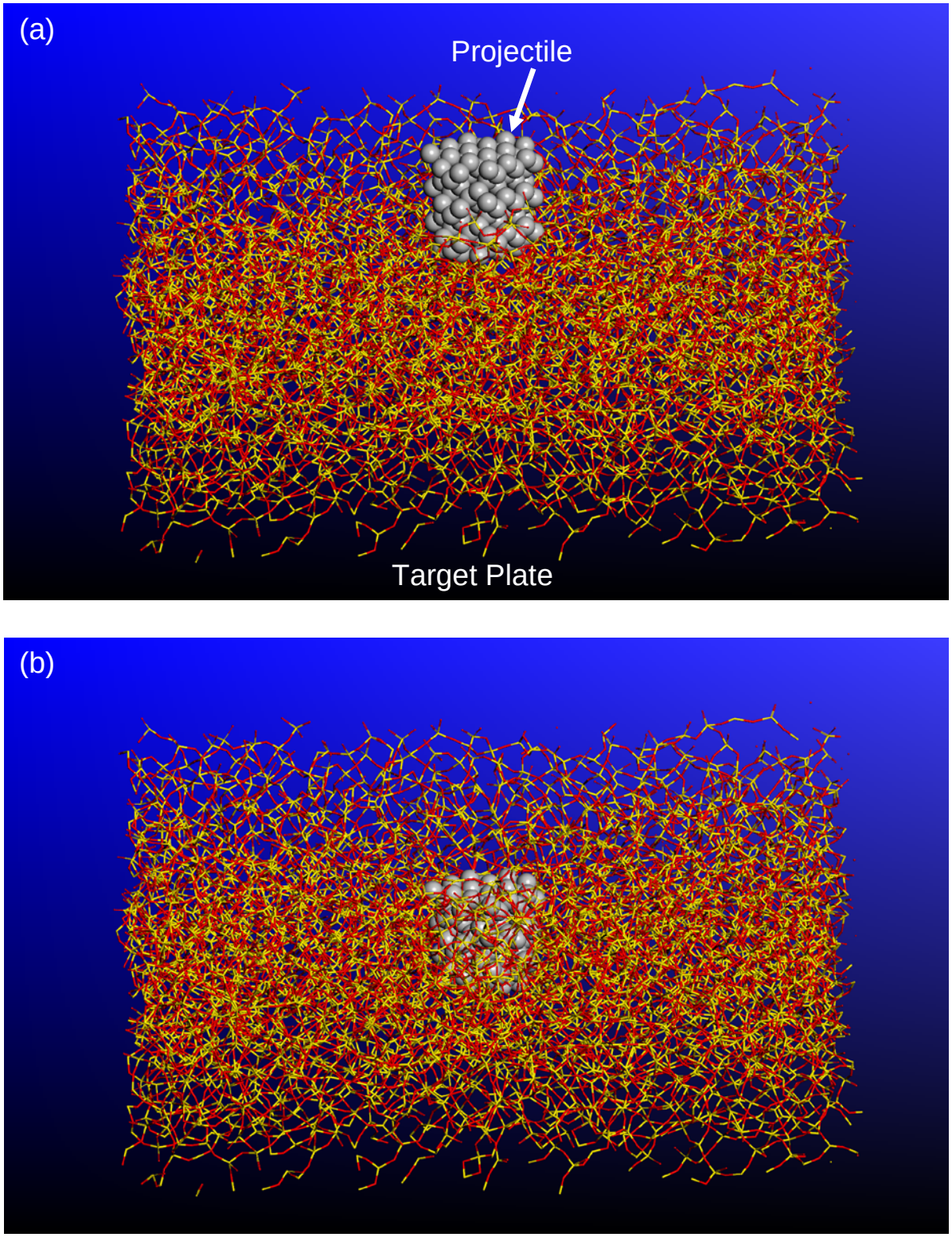

Figure 4-2 Temporal evolution of the computational domain at four times: (a) 0.5 ps; (b) 1.5 ps; (c) 2.5 ps; and (d) 3.5 ps, following the initial contact between the diamond solid right-circular cylindrical projectile moving at a high velocity and the fused-silica target plate.

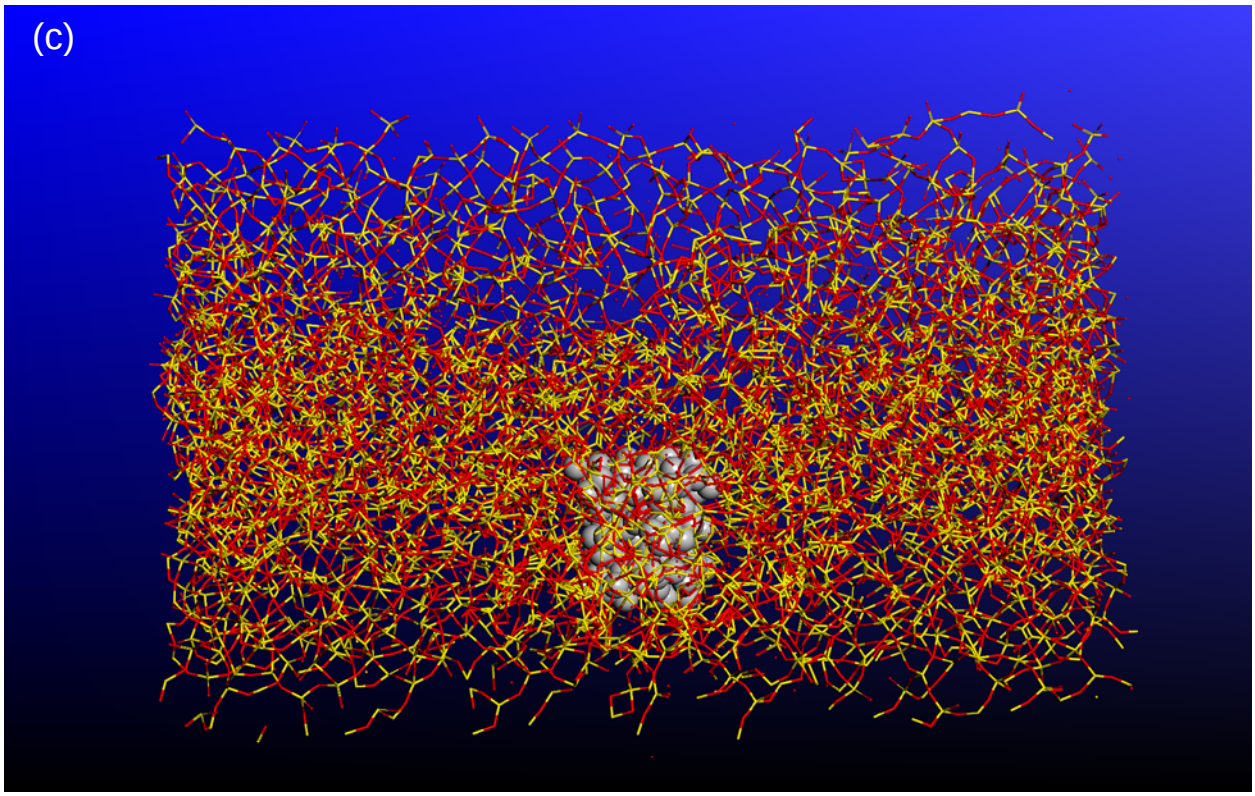

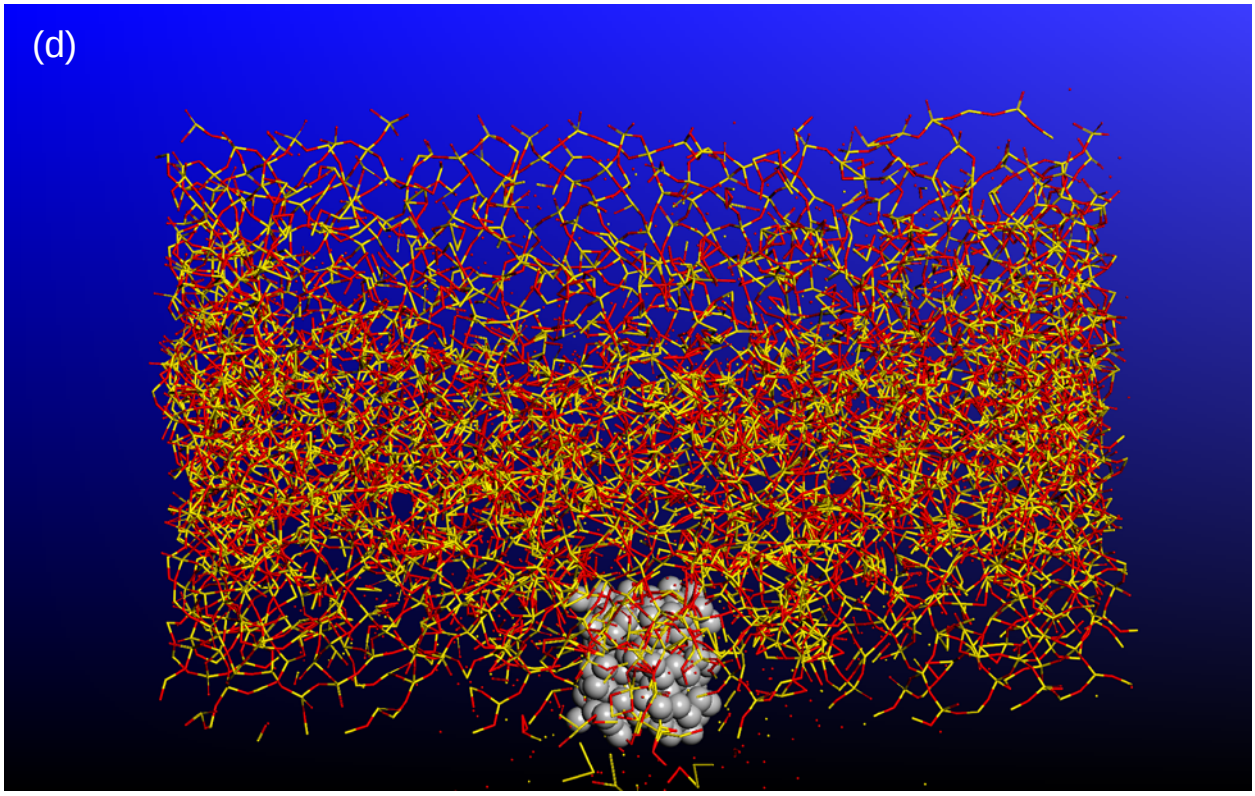

Figure 4-2 Continued.

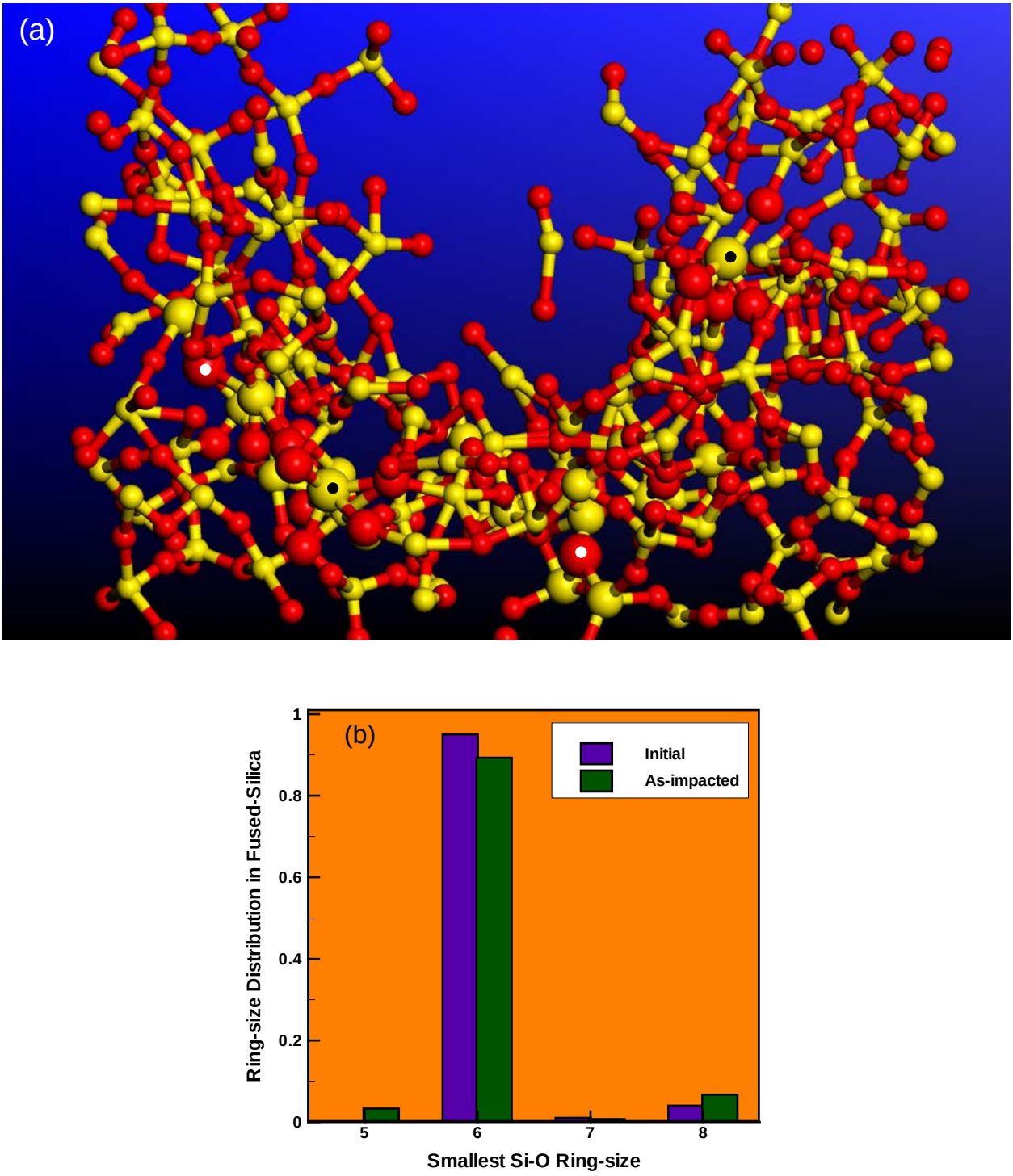

Figure 4-3 Results indicating devitrification of fused silica in the target region adjacent to the penetration hole: (a) Local stishovite-like microstructure showing two six-folded Si and two three-folded O atoms. (b) Size distribution function for the smallest Si-O rings in the fused-silica initial and as-impacted states; (c) and (d) Si-Si, O-O, and Si-O partial radial distribution functions in (c) the as-received/initial state of silica; and (d) the silica region adjacent to the penetration hole.

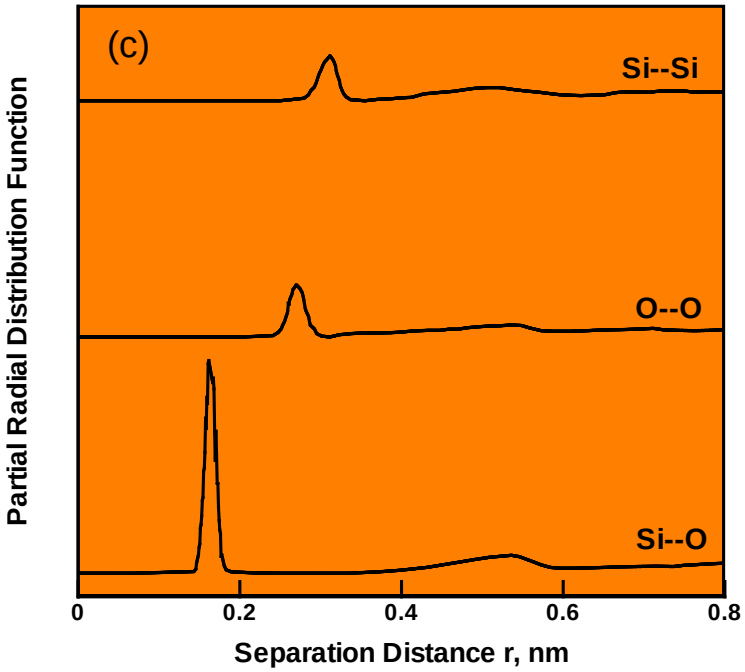

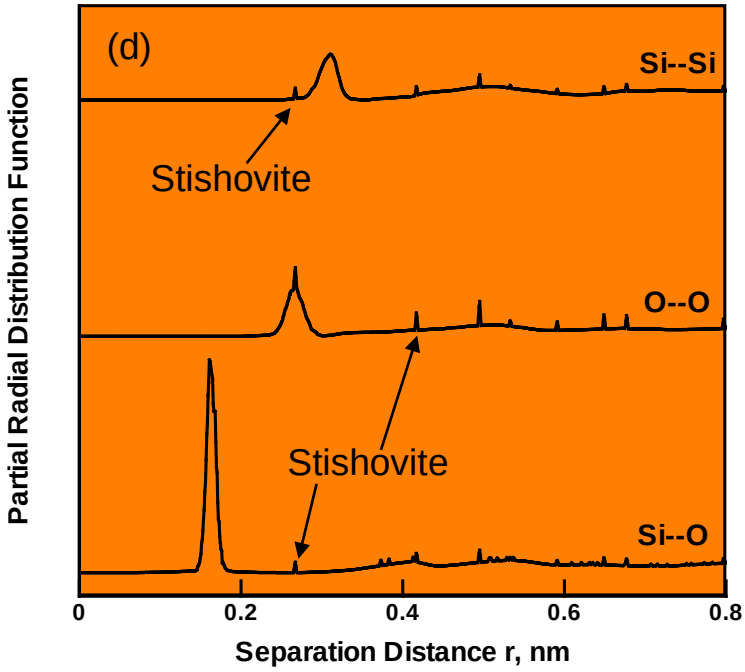

Figure 4-3 continued.

4.3.3 Quantum-Mechanical Analysis Of Fused-Silica Devitrification

To help rationalize the aforementioned changes in the microstructure of fused silica in the region adjacent to the penetration hole, a series of quantum-mechanical calculations is carried out in Ref. [16]. The main objective of these calculations was determination of the relative stability of fused silica, α-quartz and stishovite, as well as of the energy barriers associated with the fused-silica → α-quartz and fused-silica → stishovite transition states. The main results obtained revealed:

(a) At the ambient conditions, the thermodynamic stability of the three states of SiO_2 decreases in the order α-quartz, fused silica and stishovite. When the pressure is increased to 50 GPa, fused silica becomes more stable than α-quartz, while the thermodynamic stability of stishovite (still the lowest) becomes more comparable to those of the other two states;

(b) In the presence of 5% shear, the order of thermodynamic stability of the three states under ambient conditions does not change, although their values become more comparable to each other. On the other hand, at an applied pressure of 50 GPa and in the presence of 5% shear, stishovite becomes the most thermodynamically stable state, followed by α-quartz and then fused silica; and

(c) In the absence of applied shear, the energy associated with the fused-silica → stishovite transition state is higher than that for the fused-silica → α-quartz transition state. However, when 5% shear is applied, the energy associated with the fused-silica → stishovite transition state becomes substantially lower than that for the fused-silica → α-quartz transition state. These findings suggest that, in the presence of shear, and at pressures as high as 50 GPa, fused silica is more likely to convert to stishovite than α-quartz.

4.4. JH2 Continuum-material Model

The results presented and discussed in the previous section were obtained using the atomic-scale and quantum-mechanical-scale computational tools. At these length-scales, glass is modeled as an assembly of discrete interacting particles. On the other hand, when one is concerned with the ballistic limit of a ceramic glass, the employed computational methods treat glass as a continuum and, hence, a high-fidelity constitutive model is needed for this material. One of the frequently used continuum-level material models for ceramic glasses is the Johnson-Holmquist-2 (JH2) material model [22]. This model is adopted in the present work and is briefly reviewed in the remainder of this section. Additionally, in the last portion of this section, details are presented regarding modification of the JH-2 model made in the present work in order to enable the incorporation of the ballistic-impact-induced devitrification and permanent-densification effects on the constitutive behavior of fused silica.

4.4.1 General Structure of a Continuum-Level Material Model

To completely define a continuum-level material constitutive model, the relationships among the flow variables (pressure, effective stress, mass-density, energy-density, temperature, etc.) must be specified. These relations typically involve: (a) an equation of state (EOS); (b) a strength model; (c) a failure model and (d) an erosion equation. These equations arise from the fact that, in general, the total stress tensor can be decomposed into a sum of a hydrostatic stress (negative pressure) tensor (which causes a change in the volume/density of the material) and a deviatoric stress tensor (which is responsible for the shape change of the material).

Equation of state

An EOS is used to define the corresponding functional relationship between pressure, mass density (degree-of-compression) and internal energy density (temperature).

Strength model

As far as the strength model is concerned, the number and the type of equations needed to describe material-shape change induced by the deviatoric component of stress are dependent on the absence/presence of the inelastic components of the deformation tensor. That is, when the response is elastic, the changes in the corresponding deviatoric stress at a given level of deviatoric strain quantities all scale with the shear modulus of the material. Conversely, in the presence of the inelastic strains (e.g. plasticity, micro-cracking, etc.), the strength material model requires specification of the "yield criterion," "flow rule," and "constitutive relation." The yield criterion defines the (typically stress-based) condition which must be met for the onset and continuation of inelastic material response. The flow rule relates the components of the inelastic deformation increment to the applied deviatoric stress. The constitutive relation defines the appropriate equivalent inelastic strain, equivalent inelastic strain rate, and temperature dependencies of the

material yield strength (or, more precisely, the material inelastic-deformation resistance).

Failure model

A failure model generally consists of a failure criterion, i.e. an equation describing the hydrostatic or deviatoric stress and/or strain condition(s) which, when attained, cause the material to fracture and lose its ability to support tensile normal and shear stresses.

Erosion equation

The erosion equation defines one or more stress-/strain-based erosion conditions which, when met, will cause removal of the concerned material region from the computational model. This equation is generally intended for eliminating numerical difficulties arising either from highly distorted Lagrangian elements (within a finite-element framework) or from the cells containing highly degraded material. Since material removal, as modeled by the erosion equation, is a non-physical process, the extent of such removal must be limited to preserve physical fidelity of the computational model.

To summarize, the EOS along with the strength and failure models enable assessment of the evolution of the complete stress tensor during a transient non-linear dynamics analysis (like the one dealing with the transverse impact of a high-speed projectile onto a fused-silica target-plate). Such an assessment is needed in order to solve the governing (mass, momentum and energy) conservation equations. It is important to note that separate treatments of the pressure and the deviatoric stress enable inclusion of the nonlinear effects in the EOS. Generally these effects are shock-related but, in the present work, they will be, at least partly, attributed to the high-pressure-/ballistic-impact-induced devitrification and permanent densification in fused-silica.

4.4.2 Original JH2 Material Model

The JH2 model is a phenomenological model which postulates the existence of two terminal glass states: (a) an intact material; and (b) a failed material. The two material states are weighted by a single scalar variable called damage, ***D***, the evolution of which is governed by an inelastic (plasticity-like) deformation model. In the remainder of this section, details are presented regarding the JH2 model components, i.e. EOS, the strength model, the failure model, and the erosion equation.

Equation of State

The JH2 model utilizes a polynomial EOS, which, for a damage-free material, takes on the following form:

$$P = K_1\mu + K_2\mu^2 + K_3\mu^3, \quad \mu > 0 \quad \text{(Hydrostatic compression)} \tag{4-1}$$

and

$$P = K_1\mu, \quad \mu < 0 \quad \text{(Hydrostatic Tension)} \tag{4-2}$$

where the degree-of-compression is $\mu = \rho/\rho_0 - 1$, ρ and ρ_0 are the current and reference mass-densities, K_1 (the bulk modulus), K_2 and K_3 are material-specific constants.

After glass has begun to accumulate damage (i.e. when the extent of damage is no longer zero, $D > 0$), Eq. (4-1) has to be upgraded to include the effect of bulking. Bulking is a phenomenon associated with the fact that fragments of fractured materials are not generally fully conformable, and consequently fractured material is associated with a larger volume (a lower density at a constant pressure) than the damage-free material. Thus, to reach the same degree of compression μ, an additional pressure ΔP must be applied to the damaged material. The bulking-modified polynomial EOS is then given by [23]:

$$P = K_1\mu + K_2\mu^2 + K_3\mu^3 + \Delta P, \quad \mu > 0 \tag{4-3}$$

where the bulking-induced pressure increment, ΔP, is determined from energy considerations and varies from zero at $D = 0$ to $\Delta P_{\max}$ at $D = 1.0$. Assuming that a fraction $0 < \beta < 1$ of the deviatoric-strain energy decrease ΔU (due to the damage-induced decrease in deviatoric stresses, or more precisely in the material damage-resistance) is converted to an increase in hydrostatic internal energy, the bulking-induced pressure increment ΔP at a time $t + \Delta t$ can be represented in terms of ΔP at the time t as:

$$\Delta P(t + \Delta t) = -K\mu(t + \Delta t) + \sqrt{(K_1\mu(t + \Delta t) + \Delta P(t))^2 + 2\beta K_1 \Delta U}, \quad \mu(t + \Delta t) \tag{4-4}$$

where ΔU is the decrease in deviatoric-strain energy due to damage-induced damage-resistance reduction, and is given by:

$$\Delta U = U_t - U_{t+\Delta t} = \frac{\sigma_t^2 - \sigma_{t+\Delta t}^2}{6G} \tag{4-5}$$

where σ denotes the actual (i.e., not a normalized) damage resistance, and G the (damage-invariant) shear modulus.

Schematics of the JH2 EOS functional relationships for intact, fractured and damaged materials are shown in Figure 4-4(a). Examination of Eqs. (4-1)–(4-5) reveals that the JH2 EOS model includes the following parameters: $\rho_0, K_1, K_2, K_3,$ and β.

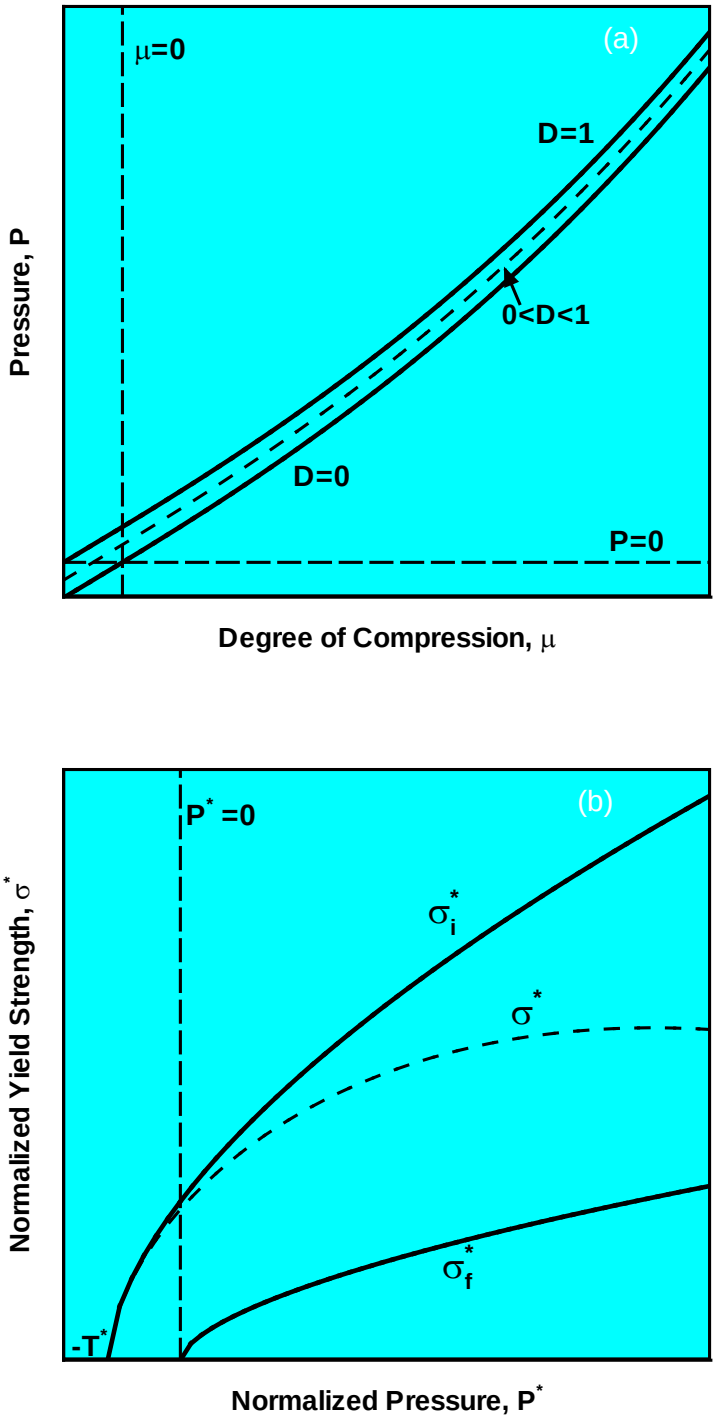

Figure 4-4 Schematics pertaining to the JH2 model: (a) equation of state; (b) strength model; and (c) failure model.

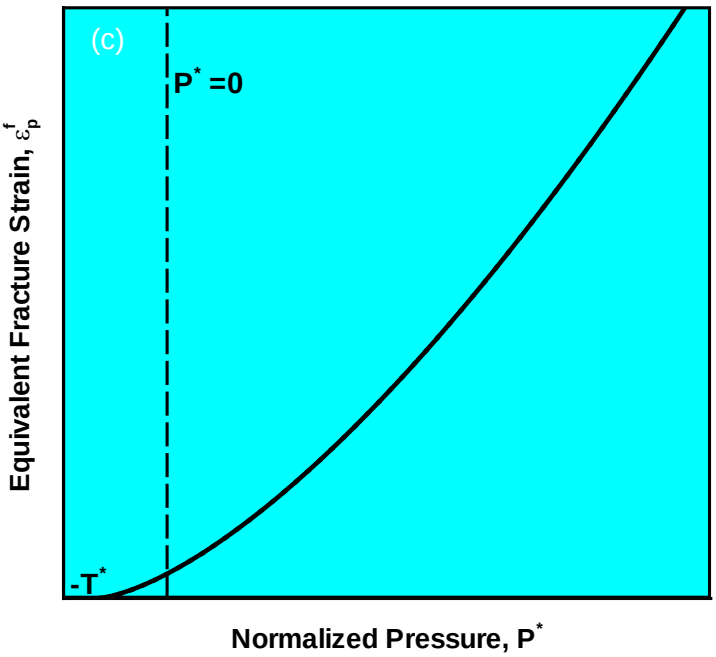

Figure 4-4 continued.

Strength Model

The JH2 strength model [23, 24] utilizes: (a) the von Mises yield criterion; (b) normality flow rule; and (c) a pressure and strain-rate-hardening constitutive relation. Since the von Mises yield criterion and the normality flow rule are well established and frequently used, details regarding their governing equations will not be presented here. However, the JH2 constitutive relation is fairly unique and will be overviewed in the remainder of this section.

For convenience, the JH2 constitutive relations utilize normalized quantities denoted by an asterisk. For example, the normalized damage-resistance (also referred to as the yield strength hereafter) σ^* is a ratio of the yield strength to the deviatoric part σ_{HEL}, of the Hugoniot Elastic Limit, HEL. In other words, σ_{HEL}, is the deviator-based effective-stress component of the (total) uniaxial-strain yield strength, HEL. Next, σ^* is defined as the following rule of mixtures of its intact and damaged counterparts:

$$\sigma^* = \sigma_i^* - D(\sigma_i^* - \sigma_f^*) \tag{4-6}$$

where subscripts *i* and *f* are used to denote intact and fractured material states. The normalized (pressure- and strain-rate-dependent, ideal-plastic) yield strength of the damage-free material, σ_i^*, and the fractured material, σ_f^*, are respectively given by:

$$\sigma_i^* = A(P^* + T^*)^N (1 + C \ln \dot{\varepsilon}^*) \tag{4-7}$$

$$\sigma_f^* = B(P^*)^M (1 + C \ln \dot{\varepsilon}^*) \tag{4-8}$$

where *A*, *B*, *C*, *M*, and *N* appearing in Eqs. (4-7) - (4-8) are all material-specific constants while P^* and T^* are respectively defined as:

$$P^* = \frac{P}{P_{HEL}} \tag{4-9}$$

and

$$T^* = \frac{T}{P_{HEL}} \tag{4-10}$$

where *P* and *T* are the actual pressure and the maximum hydrostatic tensile pressure (defined as a positive quantity) that the fused-silica material can withstand, respectively, and P_{HEL} is the pressure at the Hugoniot Elastic Limit.

As shown in Ref. [23], P_{HEL} and σ_{HEL} are related to the (uni-directional shockwave-based) uniaxial-strain compressive-yield strength, HEL, as:

$$HEL = P_{HEL} + \tfrac{2}{3}\sigma_{HEL} = K_1\mu_{HEL} + K_2\mu_{HEL}^2 + K_3\mu_{HEL}^3 + \tfrac{2}{3}\frac{2G\mu_{HEL}}{1+\mu_{HEL}} \tag{4-11}$$

Eq. (4-11) shows that both P_{HEL} and σ_{HEL} can be determined from the known HEL and μ_{HEL} (degree of compression at the elastic limit). Finally, the dimensionless material strain rate, $\dot{\varepsilon}^*$, appearing in Eqs. (4-7) and (4-8) is defined as:

$$\dot{\varepsilon}^* = \frac{\dot{\varepsilon}}{\dot{\varepsilon}_0} \tag{4-12}$$

where $\dot{\varepsilon}$ is the actual equivalent strain rate and $\dot{\varepsilon}_0$ is the reference strain rate (typically set to 1.0 s^{-1}).

Schematics of the JH2 strength model in the normalized yield strength vs. normalized pressure plane, for intact, fractured and damaged materials are shown in Figure 4-4(b). Examination of Eqs. (4-6) – (4-12) reveals that the JH2 strength model includes the following parameters: *A*, *B*, *C*, *M*, *N*, σ_{HEL} and P_{HEL}.

Failure Model

The JH2 failure model [23, 24] is of a progressive character and the evolution/accumulation of damage in this model is defined as:

$$D_{t+\Delta t} = D_t + \frac{\Delta \varepsilon_{p,t+\Delta t}}{\varepsilon^f_{p,t+\Delta t}} \tag{4-13}$$

where $\Delta \varepsilon_p$ is the increment in equivalent inelastic strain with an increment in loading and the failure strain ε_p^f is a pressure-dependent equivalent fracture strain which is defined as:

$$\varepsilon_p^f = D_1 (P^* + T^*)^{D_2} \tag{4-14}$$

where D_1 and D_2 are material specific constants.

Within the JH2 failure model, fracture occurs either when damage reaches a critical value of 1.0 or when negative pressure reaches a value of $\boldsymbol{T}$. Fractured material has no ability to support any negative pressure, while its ability to support shear is defined by Eq. (4-4 - 4-8).

A schematic of the JH2 failure model showing the effect of the pressure on the equivalent fracture strain is given in Figure 4-4(c). Examination of Eqs. (4-13) – (4-14) reveals that the JH2 failure model includes the following parameters: D_1 and D_2.

Erosion Equation

The JH2 failure model discussed above revealed that the "failed" elements do not completely lose their load-bearing capacity (at least with respect to the compression and shear). However, the resistance to deformation in such elements may be so low that they can readily acquire a large amount of deformation and significantly distort the associated finite elements. Excessively distorted elements may cause numerical problems, and should be removed from the model when a condition for the maximal allowable total equivalent strain is met. The element removal is carried out in such a way that the momentum associated with the removed nodes is transferred to the adjacent remaining nodes. The erosion model contains only one parameter, ε_{rem}, the maximum allowable total equivalent strain.

Model Parameterization for Fused Silica

Table 1 summarizes the parameterization for fused silica of the original JH2 model, i.e. the model which does not account for potential devitrification under high pressure and shear conditions encountered during a ballistic-impact event.

Parameter	Units	Value
Equation of State		
ρ_0	kg/m^3	2203
K_1	GPa	37
K_2	GPa	30
K_3	GPa	20
β	N/A	1.0
Strength Model		
A	N/A	0.93
B	N/A	0.35
C	N/A	0.003
M	N/A	0.4
N	N/A	0.77
σ_{HEL}	GPa	5.95
P_{HEL}	GPa	4.73
Failure Model		
D_1	N/A	0.053
D_2	N/A	0.85
Erosion Equation		
ε_{rem}	N/A	1.0

Table 4-1 Original Johnson–Holmquist-2 material model parameters for fused silica.

4.4.3 Inclusion of High-Pressure-Induced Devitrification into the JH2 Material Model

Before the JH2 model can be modified to include the effects of devitrification, additional atomic-scale simulations, using the same methods and tools as those employed in Ref. [16], had to be conducted. Two types of such simulations were conducted: (i) simulations of hydrostatic-pressure-loading/unloading; and (ii) simulations of simple-shear-loading of the hydrostatic-pressure-preloaded fused silica. A brief description of these simulations is presented in the remainder of this subsection.

4.4.3.1 Inclusion of High-Pressure-Induced Devitrification into the JH2 Material Model

Within these simulations, the computational cell for fused silica (given in Figure 4-3(a) of Ref. [16]) is subjected to a series of hydrostatic-compression loading-unloading cycles, where each subsequent loading cycle was associated with a somewhat higher peak pressure. These simulations resulted in two sets of results: (a) peak pressure vs. degree of compression (under loading); and (b) peak pressure vs. degree of irreversible compression (after unloading). Examples of these results are given in Figures 4-5(a)-(b), respectively.

Examination of the results depicted in Figure 4-5(a) shows that:

(a) as the degree of compression initially increases, the pressure grows at an increasing rate up to a value of approximately 8.76 GPa;

(b) as the compression increases beyond this point, the pressure first goes through an inflexion point, beyond which it grows at a decreasing rate, and then through another inflexion point, beyond which it again grows at an increasing rate; and

(c) the pressure continues to grow at an increasing rate as compression increases.

The behavior of fused silica revealed in Figure 4-5(a) suggests the occurrence of some kind of phase transition, which is initiated at the pressure of 8.76 GPa (point *A* in Figure 4-5(a)), and appears to terminate at the pressure of 17.2 GPa (point *B* in Figure 4-5(a)). Examination of the molecular-level microstructure of fused silica after its exposure to very high pressures revealed the presence of stishovite-like topology. Thus, the phase transition in question appears to be devitrification of fused silica into a stishovite-like structure.

Examination of the results depicted in Figure 4-5(b) and its comparison with the results depicted in Figure 4-5(a) revealed that:

(a) once the pressure vs. degree-of-compression begins to deviate from its initial behavior, unloading starts to produce residual compression. In other words, subjecting the material to pressure levels $P > P_A = 8.76$ GPa produces permanent changes in the fused-silica microstructure;

(b) as the applied pressure increases, the degree of residual compression also increases, first at a progressively higher rate, and subsequently at a progressively lower rate; and

(c) once the pressure exceeds a value $P > P_B = 17.2$ GPa, increase in the degree of residual compression ceases. This finding suggests that in this regime of loading, fused silica does not transform any further and the (transformed/devitrified) material is also stable and does not undergo any additional permanent changes.

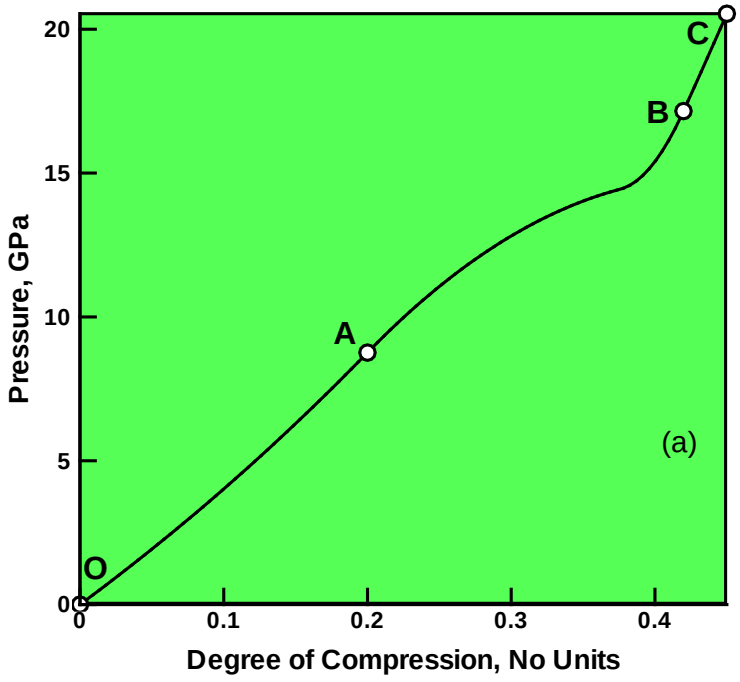

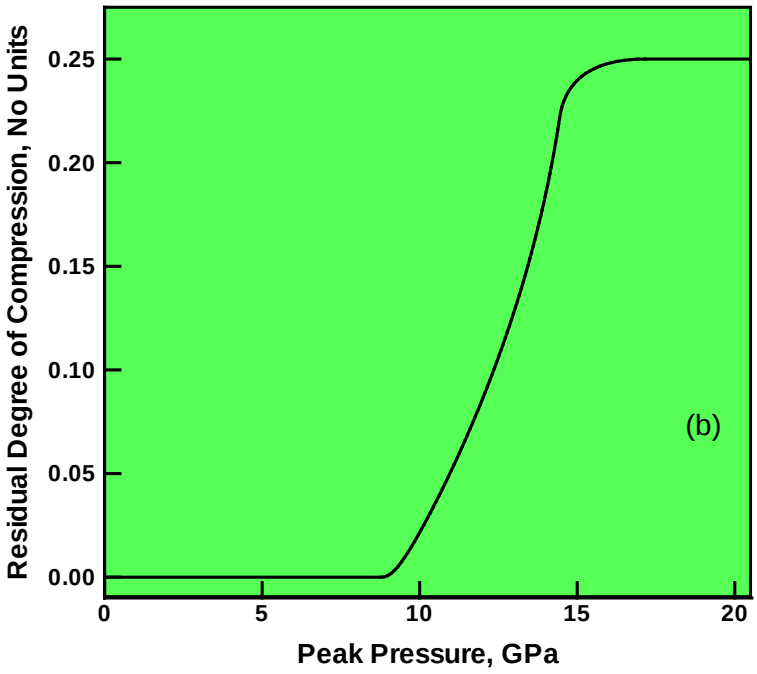

Figure 4-5 (a) Peak pressure vs. maximum degree of compression (under loading); and (b) peak pressure vs. degree of irreversible compression (after unloading).

4.4.3.2 Simple-Shear-Loading Simulations

Molecular level simple-shear tests were carried out in order to assess the effect of the irreversible changes in the fused-silica microstructure and the residual degree of compression, observed in Figure 4-5(b), on the material (shear) strength. Towards that end, once the unit cell is subjected to a sufficiently high level of pressure, and made to acquire the maximum level of residual compression, it is subjected to simple shear in small increments followed by energy minimization with respect to the atomic positions. To help prevent the computational crystal from settling into a nearby metastable higher-energy configuration, a 10,000-step 300K *NVT* (*N* – number of particles, *V* – computational-cell volume, *T* – temperature, all fixed) molecular dynamics (*equilibration*) run was introduced between the cell shearing and the energy-minimization steps. This procedure yielded a plot of the potential energy increase (relative to that in the initial optimized computational cell) versus the shear angle of the computational cell. The shear angle gradient of the potential energy increase divided by the constant unit-cell volume is then used to define the material shear strength. This procedure revealed that the shear strength of (partially) devitrified fused silica is higher by a factor of ca. 1.87 relative to the strength of fused silica in the initial state.

4.4.3.3 Modification of the JH2 Model

To account for the devitrification and permanent-densification effects revealed by the results depicted in Figures 4-5(a)-(b), both the JH2 equation of state and the associated strength model are modified. Details of these modifications are presented in the remainder of this subsection.

EOS model

Modification of the EOS entailed a number of steps including:

(a) Functional representation of the *P* vs. μ relationship depicted in Figure 4-5(a). This was done by decomposing the *P* vs. μ curve in Figure 4-5(a) into the following three segments:

(i) *OA* segment, within which the *P* vs. μ functional relationship is represented by that for the initial fused silica, Eq. (4-1), as:

$$P_{OA} = K_1^{FS}\mu + K_2^{FS}\mu^2 + K_3^{FS}\mu^3, \quad \mu > 0 \tag{4-15}$$

where superscript *FS* is used to denote the fact that the EOS parameters refer to the original fused silica.

(ii) *AB* segment, within which the *P* vs. μ segment shown in Figure 4-5(a) is represented as a cubic-spline function; and

(iii) *BC* segment, which is assumed to correspond to the state of pure (highly deformed) stishovite, in which the following P vs. μ functional relationship is used:

$$P_{BC} = K_1^{ST}\left(\mu - \mu_{irr}^{\max}\right) + K_2^{ST}\left(\mu - \mu_{irr}^{\max}\right)^2 + K_3^{ST}\left(\mu - \mu_{irr}^{\max}\right)^3, \quad \left(\mu - \mu_{irr}^{\max}\right) > 0 \tag{4-16}$$

where superscript *ST* is used to denote the fact that the EOS parameters refer to stishovite, and $\mu_{irr}^{\max}$ is the maximum degree of compression (which corresponds to complete devitrification of fused silica into stishovite); and

(b) Calculation of the pressure $P_{t+\Delta t}$ corresponding to the value of the degree of compression at the end of a given time step, $\mu_{t+\Delta t} = \mu_t + \Delta\mu$, is then done accordingly depending on which of the three (*OA*, *AB* or *BC*) segments $\mu_{t+\Delta t}$ lies, whether the $\mu_{t+\Delta t}$ is larger than the degree of compression ever experienced by the material point in question and whether the material point is under a state of (compressive) loading, unloading or reloading as:

(i) when $\mu_{t+\Delta t}$ is associated with *OA* and *BC* segments, then loading, unloading and reloading are all defined using Eqs. (4-15) and (4-16), respectively; and

(ii) when $\mu_{t+\Delta t}$ is associated with *AB* segment, the way in which $P_{t+\Delta t}$ is calculated is dependent on whether $\mu_{t+\Delta t}$ is larger than the maximum degree of compression, $\mu_{\max}$, ever experienced by the material point in question (loading) or not (unloading/reloading). In the case of loading, $P_{t+\Delta t}$ is obtained from $\mu_{t+\Delta t}$ using the aforementioned *P* vs. μ spline-function representation for *AB* segment. On the other hand, in the case of unloading or elastic-reloading, $P_{t+\Delta t}$ is given by the following relationship:

$$P_{t+\Delta t} = K_1^{AB}\left(\mu - \mu_{irr}\left(P_{\max}\right)\right) + K_2^{AB}\left(\mu - \mu_{irr}\left(P_{\max}\right)\right)^2 + K_3^{AB}\left(\mu - \mu_{irr}\left(P_{\max}\right)\right)^3, \quad \mu - \mu_{irr}\left(P_{\max}\right) > 0 \tag{4-17}$$

where superscript *AB* is used to denote the fact that the EOS parameters refer to the partially devitrified condition of fused silica associated with *AB* segment, and $\mu_{irr}\left(P_{\max}\right)$ is given by tabulating the results depicted in Figure 4-5(b). The EOS parameters appearing in Eq. (4-17) are

assumed to be given by the rule of mixtures of the corresponding parameters for the fused silica and stishovite as:

$$K_i^{AB}(P_{\max}) = \left(1 - f_{ST}(P_{\max})\right)K_i^{FS} + f_{ST}(P_{\max})K_i^{ST}, \quad i = 1-3 \tag{4-18}$$

where the volume fraction of stishovite, which is controlled by the maximum pressure ever experienced by the material point in question, is given as:

$$f_{ST}(P_{\max}) = \frac{\mu_{irr}(P_{\max})}{\mu_{irr}^{\max}} \tag{4-19}$$

The procedure outlined above ensures that, during loading, the pressure traces the P vs. μ relationship depicted in Figure 4-5(a), while during unloading and reloading, P vs. μ is given by the non-linear elastic relationship of the polynomial type.

Strength model

As indicated by the molecular-level simple-shear loading results described earlier, devitrification strengthens the material, and the intrinsic strength of devitrified glass is higher by a factor $\alpha \approx 1.87$ than that of the initial fused silica. To account for this finding, the JH2 strength model given by Eq. (4-6) is modified by multiplying the right-hand side of this equation by a factor $1-(\alpha-1)f_{ST}$.

Implementation

The modified JH2 model is next implemented in the material user subroutine, VUMAT, of the commercial finite element program ABAQUS/Explicit [25]. This subroutine is compiled and linked with the finite element solver and enables ABAQUS/Explicit to obtain the needed information regarding the state of the material and the material mechanical response during each time step, for each integration point of each element. The essential features of the coupling

between the ABAQUS/Explicit finite-element solver and the VUMAT material user subroutine at each time increment at each integration point of each element can be summarized as follows:

(a) The corresponding previous time-increment stresses and material state variables as well as the current time-step deformation gradient are provided by the ABAQUS/Explicit finite-element solver to the material subroutine. In the present work, the components of the strain tensor, damage variable D, a variable characterizing the extent of fused-silica → stishovite conversion, the maximum pressure ever experienced by the material point in question during loading, and one variable pertaining to the deletion status of the finite element are used as the state variables; and

(b) Using the information provided in (a), and the functional relationships constituting the modified JH2 material model presented in the previous section, the material stress state as well as values of the material state variables at the end of the time increment are determined within the VUMAT and returned to the ABAQUS/Explicit finite-element solver. In addition, the changes in the total internal and the inelastic energies (where appropriate) are computed and returned to the solver.

4.4.4 Fused-Silica Devitrification And Ballistic Limit

In the previous section, the JH2 model was modified to include the effects of high-pressure/high-shear-induced devitrification on the (dynamic) mechanical response of fused silica. In this section, a simple transverse impact of a monolithic fused-silica target-plate by an armor-piercing bullet is analyzed computationally in order to assess if the aforementioned modifications in the JH2 model have any significant effect on the temporal evolution and spatial distribution of damage within the fused-silica plate during impact and on the overall fused-silica-plate penetration resistance.

4.4.4.1 Computational Analysis

The transverse impact of the fused-silica target plate by the armor-piercing bullet is investigated using a Lagrangian, transient, non-linear dynamics finite element analysis (FEA). Within such an analysis, the following should be specified: (a) geometrical model; (b) meshed model; (c) computational algorithm; (d) initial conditions; (e) boundary/loading conditions; (f) contact interactions; (g) material models; (h) computational tool; and (i) computational accuracy, stability and cost. These items are briefly overviewed in the remainder of this sub-section.

Geometrical Model

The geometrical model consists of: (a) a circular-disk-shaped fused-silica target-plate with dimensions $\boldsymbol{R} \times \boldsymbol{H}$ = 90 mm × 22 mm; and (b) an M855 armor-piercing bullet, having a diameter of 5.56 mm and a mass of ~4.0 g, consisting of a steel tip, a lead core, and a 0.5-mm thick copper jacket. Due to the fact that only a normal (i.e. zero obliquity angle) impact is considered, the geometrical model possesses two vertical planes of symmetry and, hence, only one quarter of the model, Figure 4-6(a), needs to be analyzed explicitly.

Meshed Model

The fused-silica target-plate is discretized using 70,720 six-node triangular-prism first-order continuum elements, while the bullet is meshed using 1,955 four-node tetrahedron first-order continuum elements. A close-up of the finite-element mesh is depicted in Figure 4-6(b). It is seen that, in order to improve the resolution of the deformation, damage and devitrification fields, smaller finite elements are used in: (a) the cylindrical portion of the target-plate which will be affected by the advancing armor-piercing bullet; and (b) the surface sections of the bullet.

Computational Algorithm

To ensure robustness of the computational analysis, all the calculations carried out in the present work utilized a transient, displacement-based, purely-Lagrangian, conditionally-stable, dynamic explicit finite-element algorithm.

Initial Conditions

The target-plate is assumed to be initially stress-free and stationary. While the bullet is also assumed to be stress-free, it is assigned a uniform downward (i.e. in the $-\boldsymbol{z}$ direction) initial velocity.

Boundary/Loading Conditions

Due to the fact that only one quarter of the model was analyzed explicitly, the symmetry boundary condition had to be applied over the faces of the quarter-model coinciding with the symmetry planes. In addition, to simulate simple all-around simple-supporting conditions, the rim nodes on the bottom face of the target-plate are fixed in the $\boldsymbol{z}$-direction, and left unconstrained in the in-plane $\boldsymbol{x}$- and $\boldsymbol{y}$-directions. Also, to properly simulate the propagation of the impact-induced shock waves in a fused-silica structure larger than the target-plate, transmit boundary conditions are prescribed over the outer transverse faces of the target-plate.

Material Models

The three metallic materials (steel, lead and copper) present in the bullet are modeled using a linear equation of state, the Johnson-Cook strength model, the Johnson-Cook failure model and an erosion algorithm based on the maximum allowable instantaneous geometrical strain. Considering the fact that these material models were reviewed in our recent work [26], they will not be discussed any further here. As far as the fused-silica material model is concerned, the modified JH2 model (developed in the previous section) is employed. In a few of the

analyses, the original JH2 material model for fused silica was used. This model is generally constructed at pressures which are not high enough to induce fused-silica devitrification. Here, this model, without modification, is used in the pressure range in which fused-silica devitrification takes place. By comparing the results obtained using this model and the modified JH2 model, it was possible to assess the effect of fused-silica devitrification on the ballistic-penetration resistance of this material.

Contact Interactions

At the beginning of the simulation, only contact interactions between the bullet and the target-plate exist. However, as the fused-silica plate begins to experience damage and fragments are created, additional contacts involving these fragments must be taken into account.

Normal interactions are modeled using a "penalty" contact method, within which the interpenetration of the surfaces is resisted by linear spring forces/contact-pressures with values proportional to the depth of penetration. These forces, hence, tend to pull the surfaces into the (no-penetration) equilibrium position. Contact pressures are not transmitted between the interacting bodies unless the nodes on the (node-defined) "slave surface" of one body contact the (element-defined) "master surface" of the other body. There is no limit to the magnitude of the contact pressure that could be transmitted when the surfaces are in contact. Transmission of shear stresses across the contact interfaces is defined in terms of a static and a kinetic friction coefficient as well as an upper-bound shear stress limit (a maximum value of shear stress which can be transmitted before the contacting surfaces begin to slide).

Computational Tool

All the calculations carried out in the present work were done using ABAQUS/Explicit, a general purpose finite-element program [25]. Within this tool, the problem at hand (formulated in

terms of a set of mass, momentum and energy conservation differential equations along with the material constitutive relations, initial, boundary and contact/interaction conditions) is solved numerically using the aforementioned finite-element algorithm.

Computational Accuracy, Stability and Cost

A standard mesh sensitivity analysis was carried out (the results not shown for brevity) in order to ensure that the results obtained are accurate, i.e. insensitive to the size of the elements used.

Due to the conditionally-stable nature of the explicit finite element analysis used, the maximum time increment during each computational step had to be lower than the attendant stable time increment. To keep the computational cost reasonable while ensuring accuracy and stability of the computational procedure, a mass-scaling algorithm is used. This algorithm adaptively adjusts material density in the critical stable-time-increment-controlling finite elements without significantly affecting the computational analysis results. A typical transient non-linear dynamics analysis of a VMT required 15 minutes to 2 hours of (wall-clock) time on a 12-core, 3.0 GHz machine with 12 GB of memory.

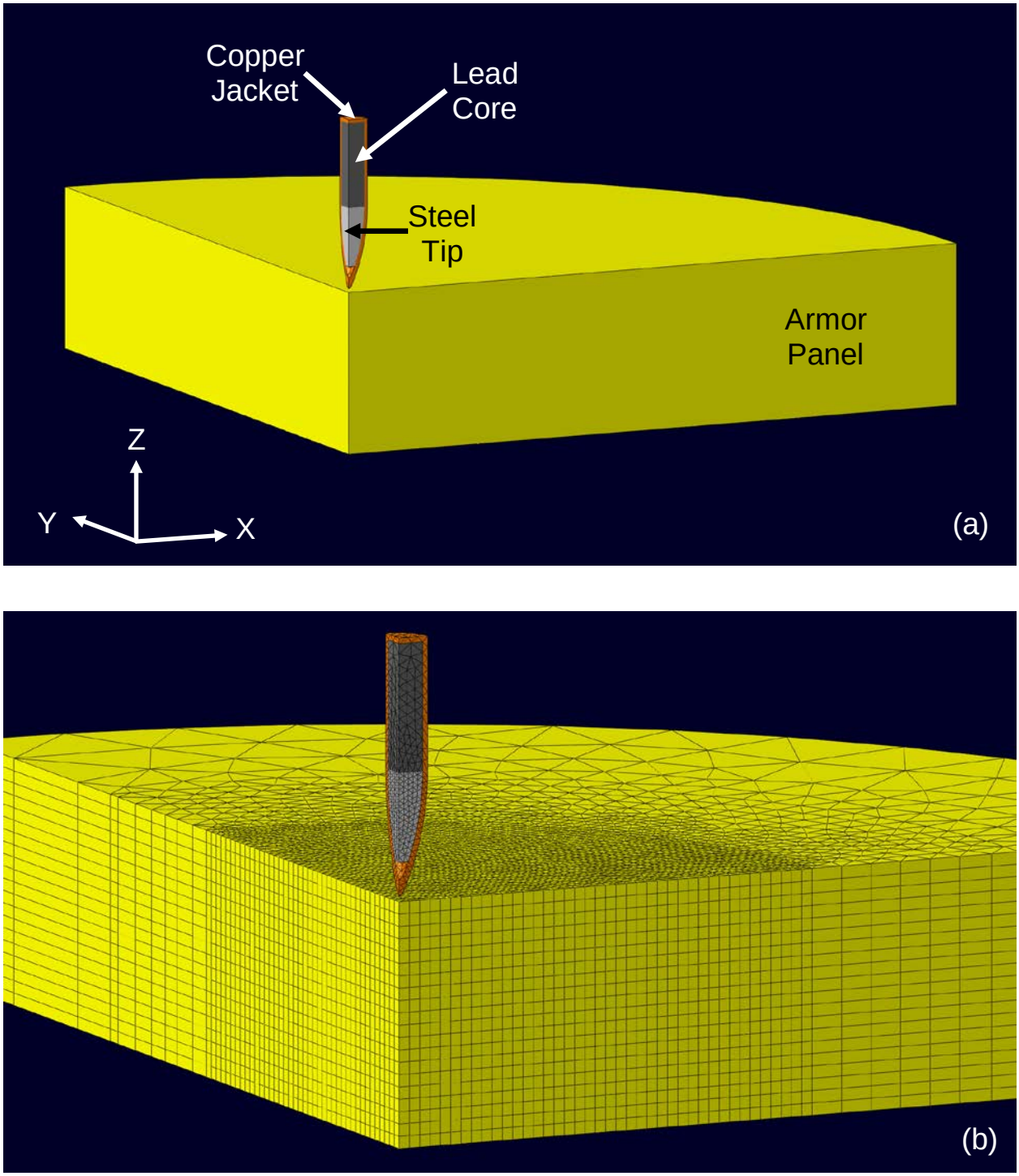

Figure 4-6 (a) Geometrical; and (b) meshed models for the transient non-linear finite element analyses of the impact of a full-jacketed metal bullet onto a fused-silica target-plate. Due to inherent symmetry of the problem, only one-quarter of the model is analyzed.

4.5 Results and Discussion

In this section, the main results pertaining to the transverse-normal impact of the M855 armor-piercing projectile onto the fused-silica target-plate are presented and discussed. Since fused-silica devitrification takes place only at sufficiently high pressures and the peak pressure of the fused-silica target-plate impacted by the projectile scales directly with the projectile incident velocity, the results at one representative low projectile incident velocity (the condition which does not result in fused-silica devitrification) and the results at one representative high projectile incident velocity (the condition which results in fused-silica devitrification) are presented and discussed. In each case, two sets of results are presented (unless they are practically indistinguishable), one for the original and the other for the modified JH2 fused-silica material models. This approach enabled quantification of the effect of fused-silica devitrification on its ballistic-penetration resistance.

Projectile Incident Velocity 1000 m/s

The temporal evolution and spatial distribution of the hydrostatic pressure within the fused-silica target-plate for the case of the projectile incident-velocity of 1000 m/s and the original JH2 fused-silica material model is displayed in the right half of Figures 4-7(a)–(d). The corresponding (mirrored across the symmetry plane) results for the case of the modified JH2 material model are presented in the left half of Figures 4-7(a)-(d). It is seen that the corresponding results obtained using the two JH2 models are essentially identical. This finding suggests that at this projectile incident velocity, the attendant pressures are too low to initiate fused-silica devitrification.

It should be noted that in Figures 4-7(a)–(d), for improved clarity, the projectile is not shown. Also, the finite elements within the impacted region of the fused-silica target-plate and the

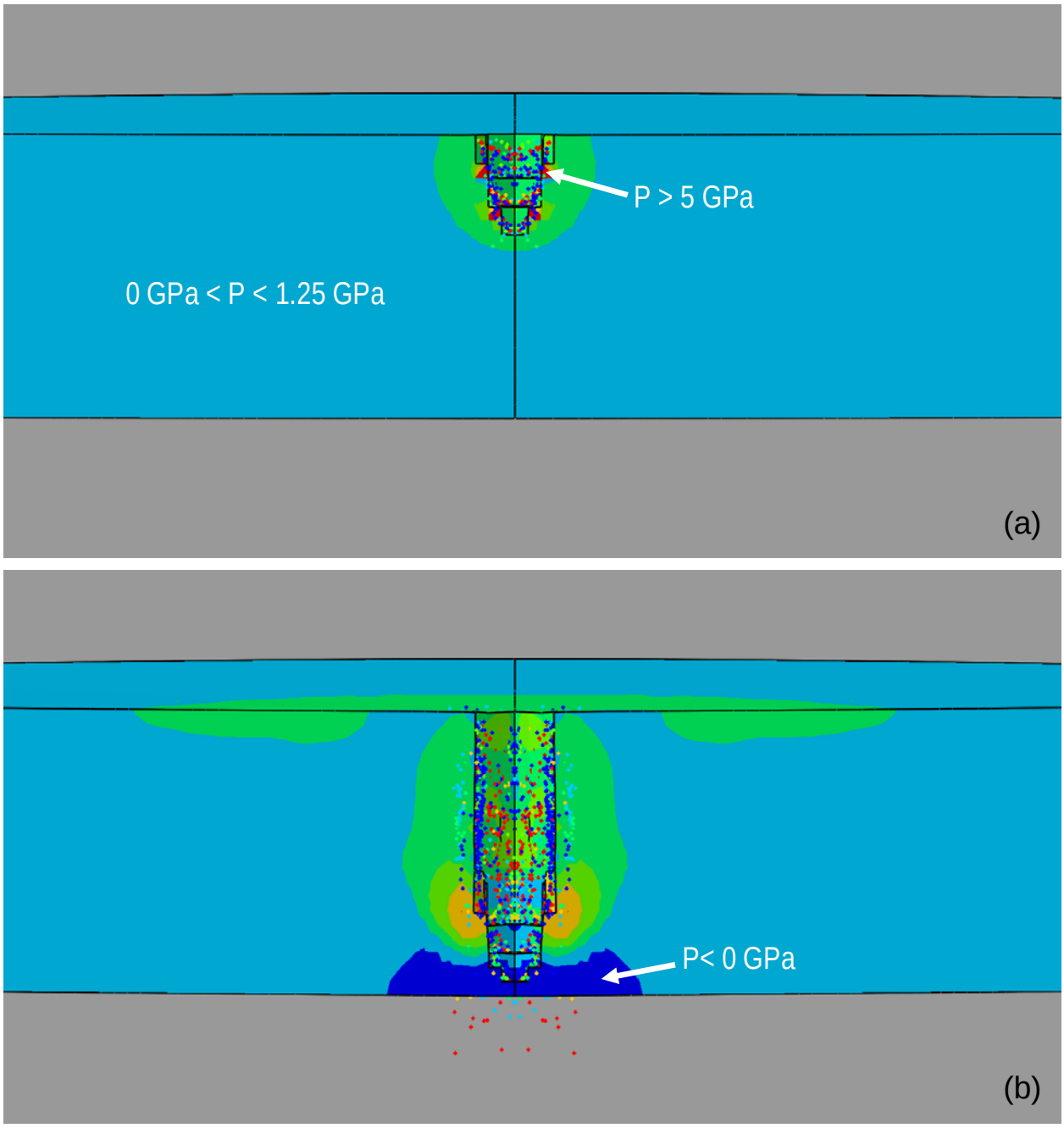

Figure 4-7 Temporal evolution and spatial distribution of the hydrostatic pressure within the fused-silica target-plate for the case of the projectile incident-velocity of 1000 m/s at post-impact times of: (a) 8 μs; (b) 22 μs; (c) 36 μs; and (d) 50 μs. In each part, the results shown on the left and the right halves correspond to the cases of the modified and the original JH2 material models, respectively.

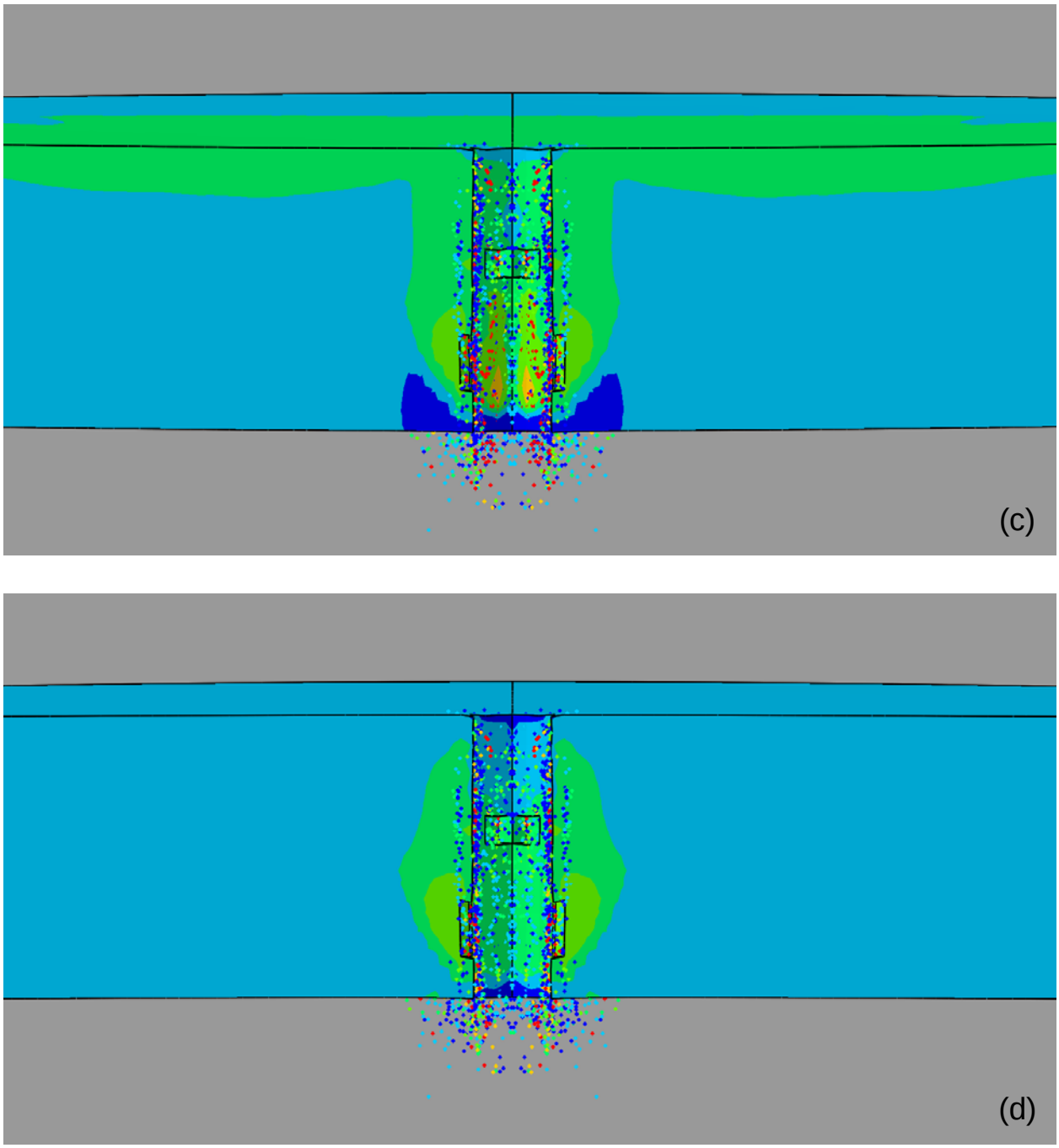

Figure 4-7 continued.

surrounding region are adaptively (i.e., when their distortion reaches a critical level) converted into the smoothed particle hydrodynamics (SPH) particles. Traditionally, to avoid numerical problems caused by highly distorted elements, such elements are removed from the analysis (an unphysical process which compromises the accuracy of the results). The conversion of such elements into SPH (interpolation pseudo-)particles is a significant improvement since these particles continue to provide the material they represent with structural and inertial deformation resistance. Within the ABAQUS viewer, SPH particles are shown as circles regardless of the orientation of the computational model.

Examination of the results displayed in Figures 4-7(a)–(d) reveals:

(a) for all the simulation times covered in these figures, the highest pressures are found in the region of the fused-silica target plate surrounding, laterally, the penetration hole; (b) at the shortest simulation time, Figure 4-7(a), a high-pressure region is also found underneath the advancing projectile. However, by the next simulation time, Figure 4-7(b), the compressive pressure wave emitted from the projectile tip arrives to, and reflects as a tensile pressure wave from, the target-plate back-face;

(c) as the wider cylindrical portion of the projectile enters the penetration hole, it pushes the fused-silica material outward, causing the development of an increased high-pressure region in the top portion of the target plate, Figures 4-7(b)-(d); and

(d) as the projectile begins to leave the penetration hole, high pressure regions surrounding the hole begin to relax, Figures 4-7(c)-(d).

The temporal evolution of the projectile (back face) velocity for the cases of the original and the modified JH2 material models, and the projectile incident-velocity of 1000 m/s, are

depicted in Figure 4-8. Examination of the results depicted in Figure 4-8 reveals that, as expected, the two sets of results are effectively identical.

Projectile Incident Velocity 2000 m/s

The temporal evolution and spatial distribution of the stishovite volume fraction and hydrostatic pressure within the fused-silica target-plate for the case of the projectile incident-velocity of 2000 m/s and the original JH2 fused-silica material model is displayed in the left and right halves of Figures 4-9(a)–(d), respectively. The corresponding results, but for the case of the fused-silica represented using the modified JH2 model, are given in Figures 4-10(a)–(d). At this projectile incident velocity, the attendant pressures are sufficiently high to initiate fused-silica devitrification. Again, the finite elements are adaptively converted into the SPH particles.

Examination of the results displayed in Figures4- 9(a)–(d) reveals:

(a) since the original JH2 model used does not allow fused-silica devitrification, the volume fraction of stishovite formed, as shown in Figures 4-9(a)–(d), is zero;

(b) for all the simulation times covered in these figures, the highest pressures are found in the region of the fused-silica target plate surrounding, laterally, the penetration hole;

(c) at the shortest simulation time, Figure 4-9(a), a high-pressure region is also found underneath the advancing projectile. However, by the next simulation time, Figure 4-9(b), the compressive pressure wave emitted from the projectile tip arrives to, and reflects as a tensile pressure wave from, the target-plate back-face; and

(d) as the wider cylindrical portion of the projectile enters the penetration hole, it pushes the fused-silica material outward, causing the development of an increased high-pressure region in the top portion of the target plate, Figures 4-9(b)-(d).

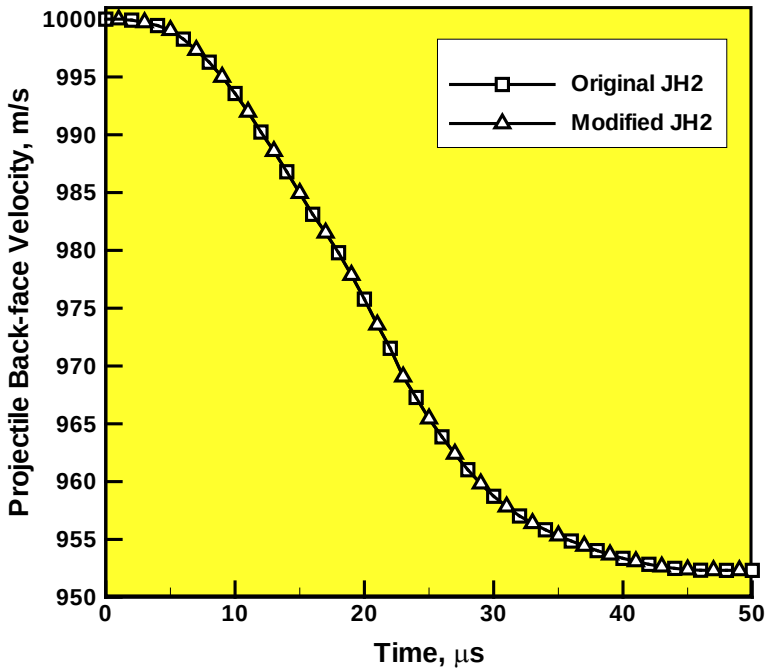

Figure 4-8 Temporal evolution of the projectile (back face) velocity for the case of the original and modified JH2 material models, with projectile incident velocity of 1000 m/s.

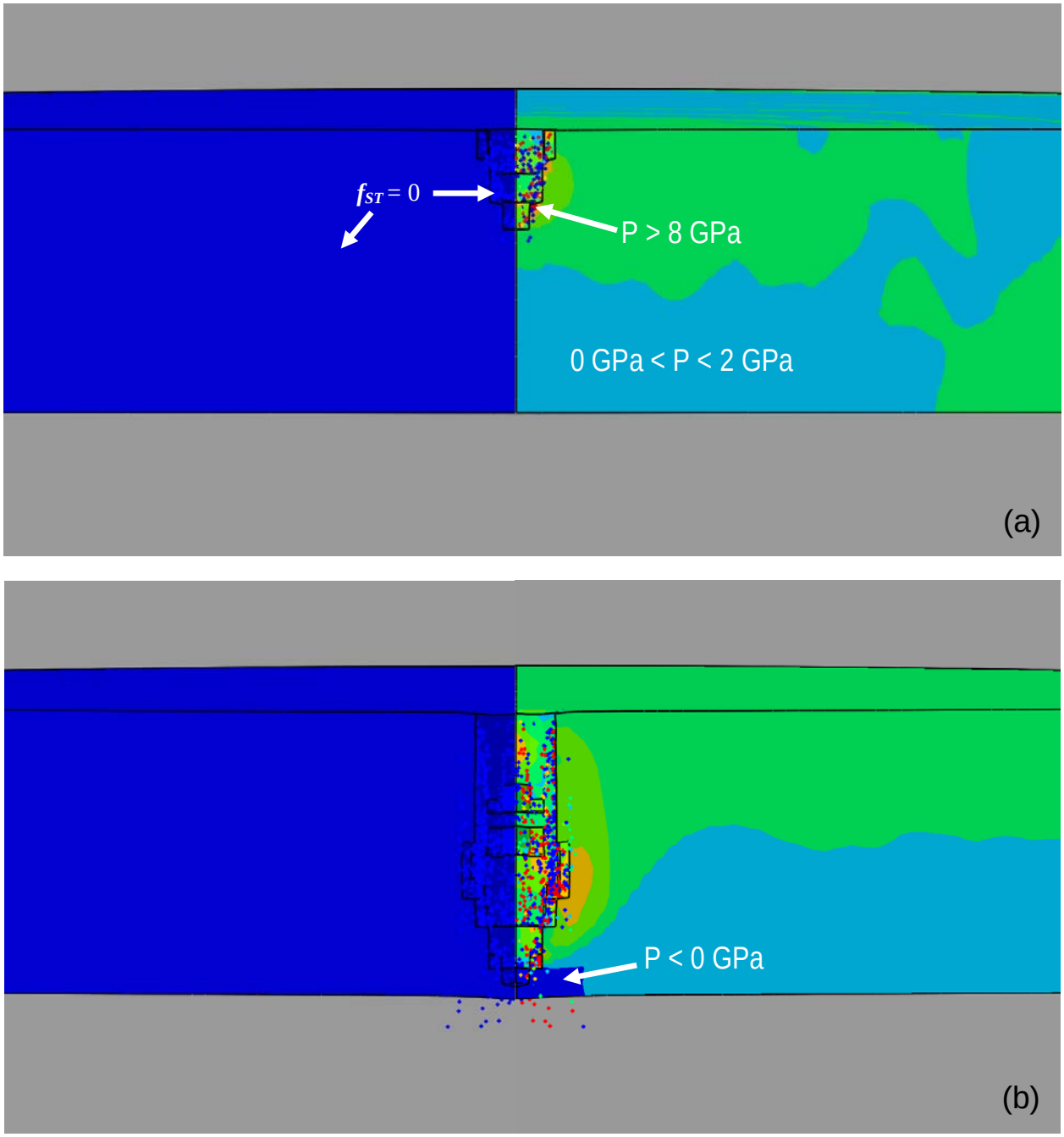

Figure 4-9 Temporal evolution and spatial distribution of the stishovite volume fraction (left half) and hydrostatic pressure (right half) within the fused-silica target-plate for the case of the projectile incident-velocity of 2000 m/s and stable fused-silica target plate, at post-impact times of: (a) 4 μs; (b) 11 μs; (c) 18 μs; and (d) 25 μs.

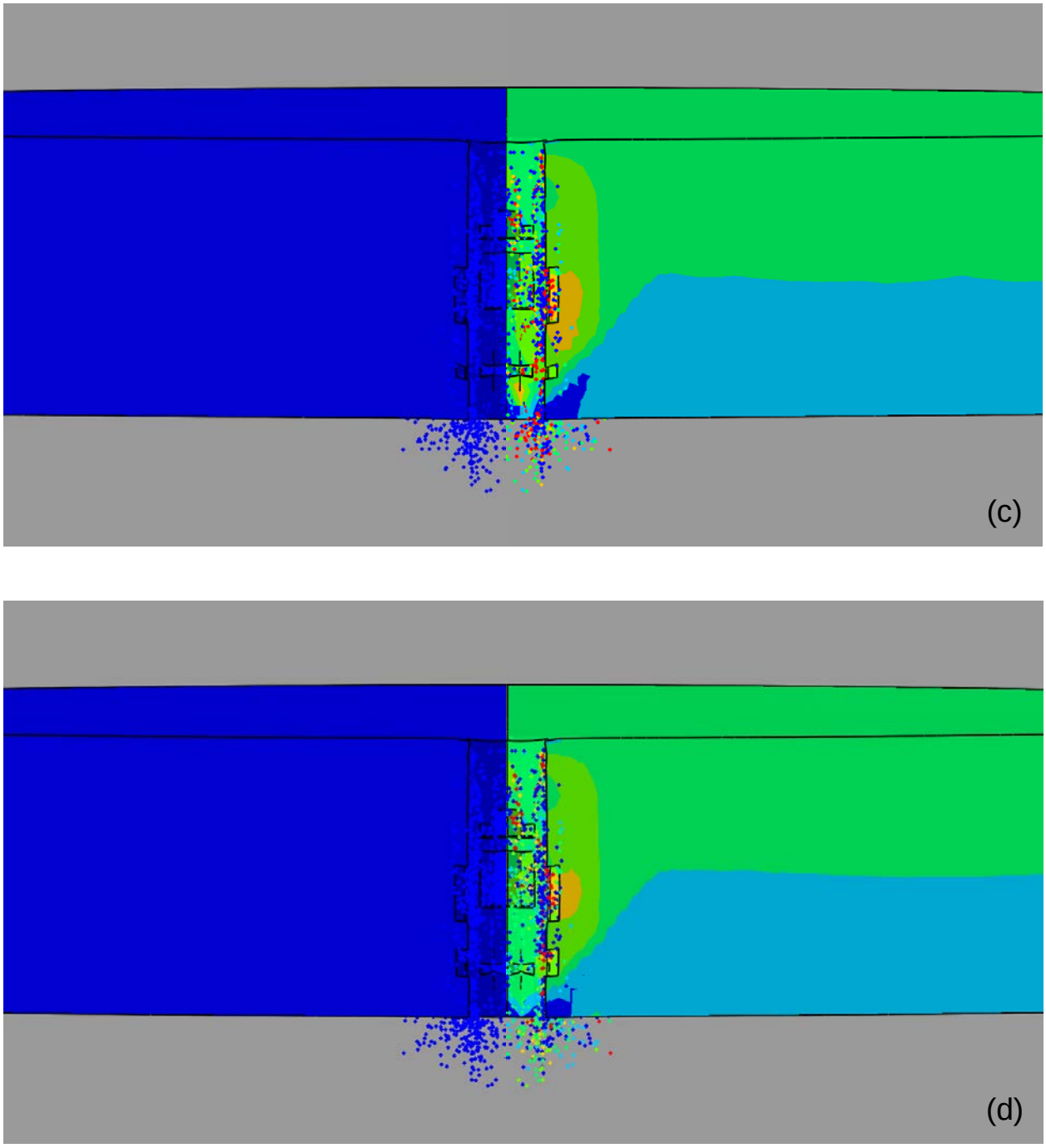

Figure 9. continued.

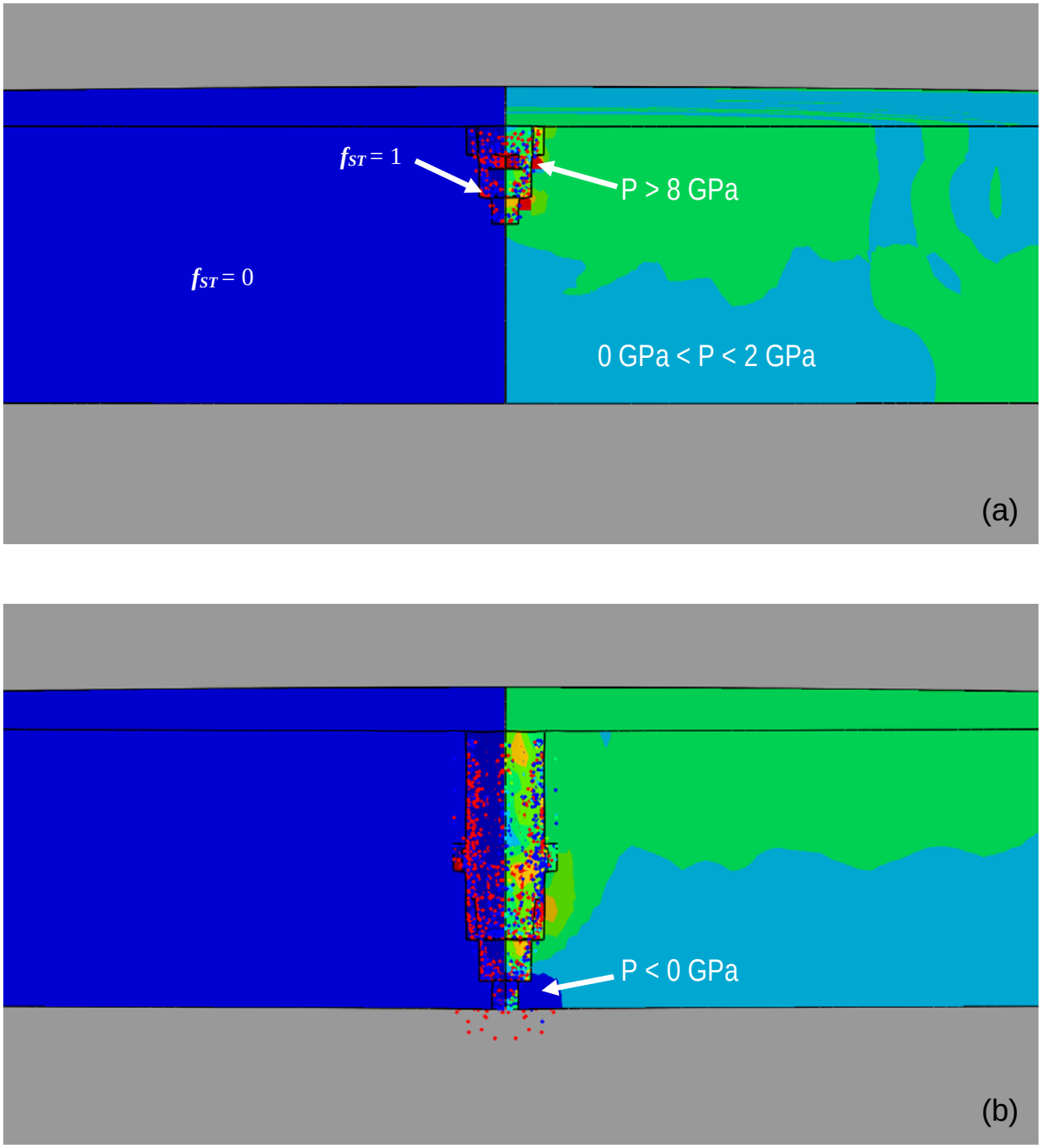

Figure 4-10. Temporal evolution and spatial distribution of the stishovite volume fraction (left half) and hydrostatic pressure (right half) within the fused-silica target-plate for the case of the projectile incident-velocity of 2000 m/s and devitrified fused-silica target plate, at post-impact times of: (a) 4 μs; (b) 11 μs; (c) 18 μs; and (d) 25 μs.

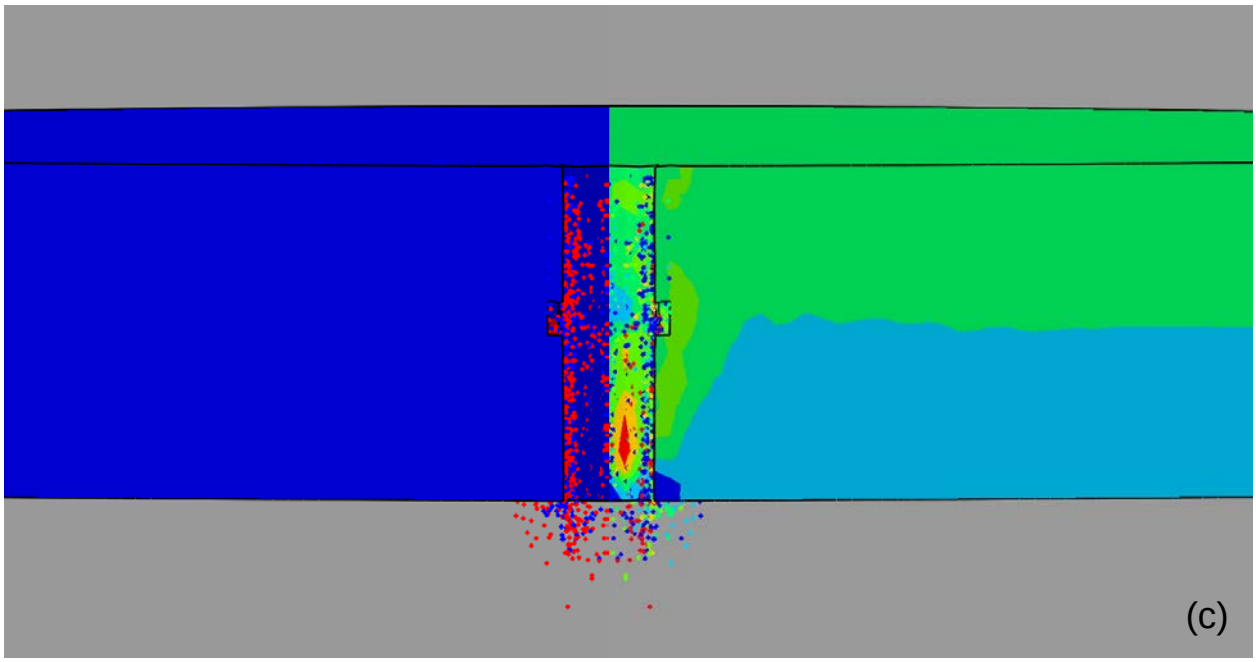

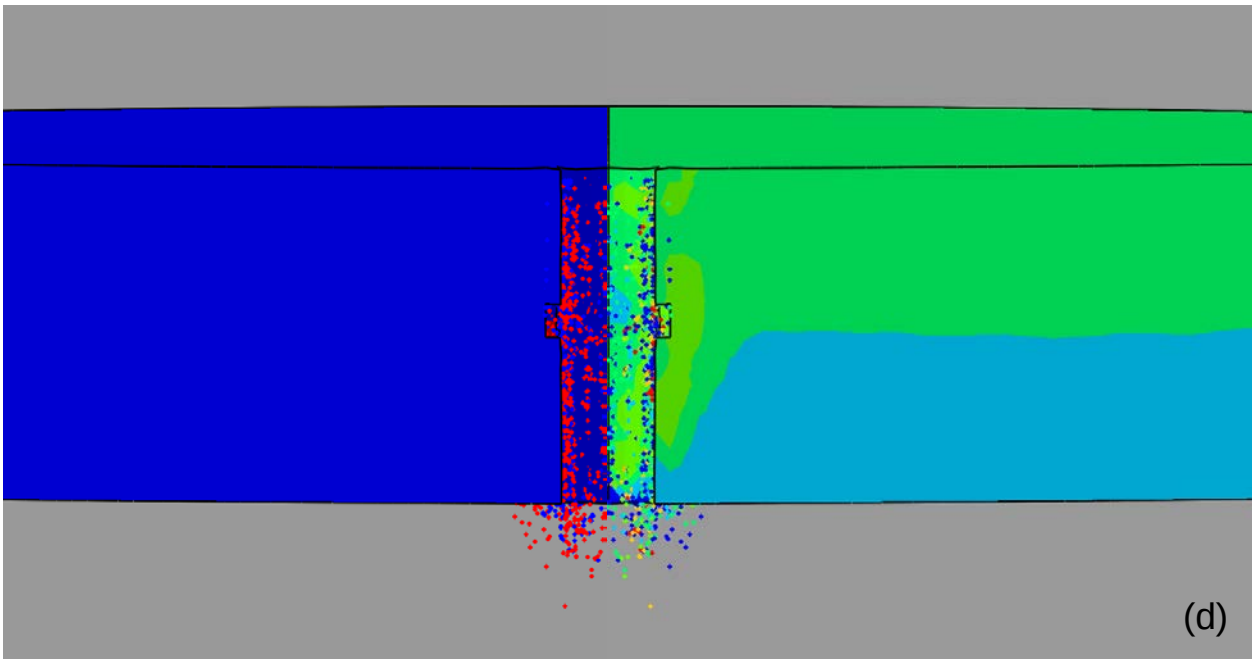

Figure 4-10. continued.

Comparison of the results displayed in Figures 4-9(a)–(d) and Figures 4-7(a)–(d) reveals the effect of the incident projectile velocity on the structural and the failure response of fused silica in the case when devitrification of this material is not permitted. It is seen that:

(a) higher projectile incident velocities increase the size of the damage region, as represented by the number of target-plate continuum elements converted to SPH particles;

(b) the pressures in the target-plate region surrounding the penetration hole are generally higher for the case of the higher projectile incident velocity; and

(c) at the lower projectile incident velocity, the projectile causes both penetration and elastic bending of the target-plate. Consequently, once the projectile has left the penetration hole, the target-plate springs back, Figures 4-7(c)–(d). In the case of the higher projectile incident velocity, on the other hand, the projectile mainly penetrates the target-plate and very little target-plate spring-back is observed, Figures 4-9(c)–(d).

Examination of the results displayed in Figures 4-10(a)–(d) reveals:

(a) formation of stishovite in the target-plate region surrounding the penetration hole, Figures 4-10(a)–(d) (left half); and

(b) points (b)–(d) made for the results shown in Figures 4-9(a)–(d) are still valid here.

Comparison of the results displayed in Figures 4-9(a)–(d) and Figures 4-10(a)–(d) reveals the effect of fused-silica devitrification on its structural and failure response during impact by the same type of projectile with the same (2000 m/s) incident velocity. It is seen that:

(a) the extent of damage surrounding the penetration hole is reduced in the case of fused-silica undergoing devitrification, e.g. Figure 4-9(b) vs. Figure 4-10(b). This finding is expected since devitrification competes with the fused-silica deformation/fracture processes; and

(b) high-pressure regions are more closely localized to the walls of the penetration-hole in the case of the fused-silica undergoing devitrification, e.g. Figure 4-9(c) vs. Figure 4-10(c). This finding is also expected since, as shown in Figure 4-5(a), once the devitrification process begins, the accompanying pressure levels are lower (compared to the case of fused-silica).

The temporal evolution of the projectile (back face) velocity for the case of the original and modified JH2 material models, and the projectile incident-velocity of 2000 m/s, is depicted in Figure 4-11. Examination of the results depicted in Figure 4-11 reveals that fused-silica devitrification enables more extraction of the kinetic energy from the projectile. This results in lowering residual velocity of the projectile from 1971 m/s to 1963 m/s. On the absolute scale, the effect is quite small (8 m/s). On the other hand, in relative terms, the effect is significant ($\frac{1971-1963}{2000-1971}\times 100 = 27.6\%$).

Brief Discussion

The results presented in the previous subsection clearly revealed that, if the projectile velocity, and thus, the pressure in the target-plate region surrounding the penetration hole, is sufficiently high, fused-silica devitrification can lead to measurable improvements in the glass ballistic-resistance. It should be noted that this effect is an outcome of the competition between two opposing phenomena: (a) since devitrification results in a reduction of pressure, at a given level of compression, and the strength of the JH2-intact-phase of the fused-silica is affected by the pressure level, devitrification tends to promote inelastic deformation (and thus fracture) of fused-silica; and (b) since the result of fused-silica devitrification is stishovite, which possesses substantially higher shear strength than fused-silica, devitrification also contributes to an increase

in the strength of the JH2-intact-phase of the fused-silica, and thus reduces the tendency for fused-silica inelastic deformation/fracture. The fact that improvements in the fused-silica ballistic-penetration resistance are observed as a result of its devitrification then suggests that the contribution of the second phenomenon to the material strength overrides the contribution of the first phenomenon.

Another way to analyze the outcome of the projectile/target-plate interaction in the case of the non-devitrified and devitrified fused-silica is to consider partitioning of the energy transferred from the projectile to the target-plate during impact. In the case of stable fused-silica, the target-plate acquires three nonzero components of its energy: (a) kinetic energy; (b) strain energy; and (c) friction-induced dissipated energy. In the case of the devitrified fused-silica, on the other hand, the target-plate acquires an additional component of its energy, that is, the zero-stress internal energy. This energy is associated with the transformation of the amorphous SiO_2 into a crystalline high-energy form of SiO_2. Furthermore, zero-stress internal energy may become a significant fraction (approximately 20%, in the present case) of the total energy acquired by the target-plate. Since zero-stress internal energy is associated with fused-silica devitrification and, hence, is not present in the case of stable fused silica, one would expect an increase in the target-plate penetration resistance in the case of fused silica undergoing devitrification.

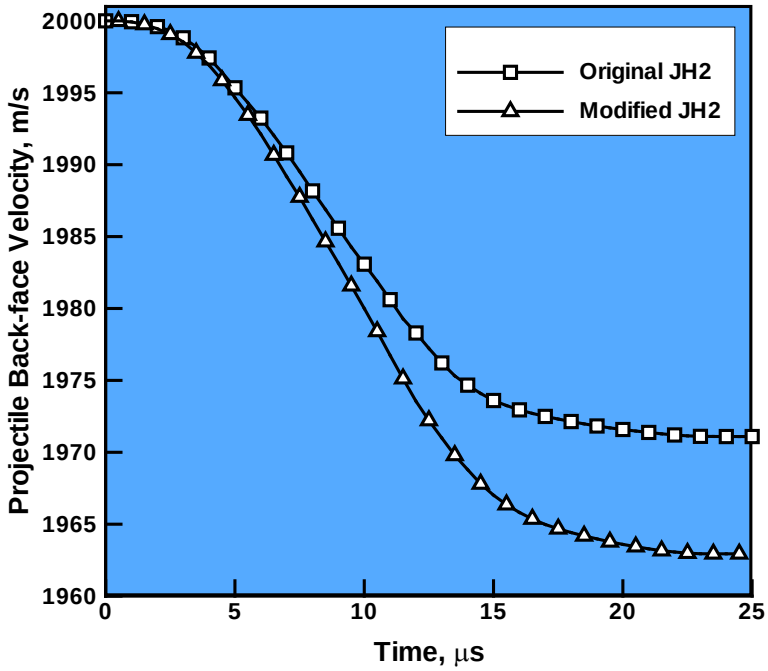

Figure 4-11 Temporal evolution of the projectile (back face) velocity for the case of the original and modified JH2 material models, with projectile incident velocity of 2000 m/s.

4.6. Summary and Conclusions

Based on the results obtained in the present work, the following main conclusions can be made:

1. Molecular-level simulations revealed that fused-silica, when subjected to high pressures, can undergo devitrification which results in the formation of high-density stishovite. This process is facilitated by the application of shear stresses which help lower the energy barrier associated with the fused-silica → stishovite transition-state.

2. To include the aforementioned devitrification effects into the fused-silica constitutive response, the classical Johnson-Holmquist-2 (JH2) model was appropriately modified. This was done by using the molecular-level computational results to infer the nature and extent of the devitrification process, as a function of the applied pressure, as well as the effect of the formed stishovite on the material (shear) strength.

3. The modified JH2 model was used within a transient, non-linear dynamics finite-element analysis of a fused-silica target-plate normal-impact by an armor-piercing bullet, in order to assess the potential devitrification-induced improvements in the fused-silica ballistic limit. To help with this assessment, a parallel set of computational analyses was carried out in which the original JH2 fused-silica material model was used, the model which does not account for the pressure-induced devitrification and strengthening.

4. The results obtained revealed that only when the bullet incident velocity and, thus, the impact-generated pressures within the fused-silica target-plate are sufficiently high, can the fused-silica devitrification process improve ballistic-penetration resistance of fused-silica. Furthermore, when the degree of devitrification is high, as observed at the highest bullet incident velocities, the effects of devitrification on the ballistic-penetration resistance are considerable.

4.6. References

1. E. Strassburger, P. Patel, W. McCauley and D. W. Templeton, "*Visualization of Wave Propagation and Impact Damage in a Polycrystalline Transparent Ceramic- AlON*," Proceedings of the 22nd International Symposium on Ballistics, November 2005, Vancouver, Canada.
2. AMPTIAC Quarterly: *Army Materials Research*: *Transforming Land Combat Through New Technologies*, 8, no.4, 2004.
3. E. Strassburger, P. Patel, J. W. McCauley, C. Kovalchick, K. T. Ramesh and D. W. Templeton, "*High-Speed transmission Shadowgraphic and Dynamic Photoelasticity Study of Stress Wave and Impact Damage Propagation in Transparent Materials and Laminates Using The Edge-on Impact Method*," Proceedings of the 23rd International Symposium on Ballistics, Tarragona, Spain, April 2007.
4. D. Z. Sun, F. Andreiux, A. Ockewitz, "*Modeling of the Failure Behavior of Windscreens and Component Tests*," 4th LS-DYNA Users' Conference, Bamberg, Germany, 2005.
5. W. D. Kingery, H. K. Bowen and D. R. Uhlmann, *Introduction to Ceramics*, 2nd ed., John Wiley & Sons: New York, 1976, 91–124.
6. M. Grujicic, W. C. Bell, B. Pandurangan, B. A. Cheeseman, C. Fountzoulas and P. Patel, D. W. Templeton and K. D. Bishnoi, "*The Effect of High-pressure Densification on Ballistic-penetration Resistance of Soda-lime Glass*," Journal of Materials: Design and Applications, 225: 298–315, 2011.
7. C. S. Alexander, L.C. Chhabildas, W.D. Reinhart, D.W. Templeton, "*Changes to the shock response of quartz due to glass modification*," International Journal of Impact Engineering, 35: 1376–1385, 2008.
8. M. Grujicic, B. Pandurangan, N. Coutris, B. A. Cheeseman, C. Fountzoulas, P. Patel and E. Strassburger, "*A Ballistic Material Model for Starphire®, A Soda-lime Transparent Armor Glass*," Materials Science and Engineering A, 492: 397–411, 2008.
9. M. Grujicic, B. Pandurangan, W. C. Bell, N. Coutris, B. A. Cheeseman, C. Fountzoulas and P. Patel, "*An Improved Mechanical Material Model for Ballistic Soda-Lime Glass*," Journal of Materials Engineering and Performance, 18: 1012–1028, 2009.
10. M. Grujicic, B. Pandurangan, N. Coutris, B. A. Cheeseman, C. Fountzoulas and P. Patel, "*A Simple Ballistic Material Model for Soda-Lime Glass*," International Journal of Impact Engineering, 36: 386–401, 2009.
11. M. Grujicic, W. C. Bell, P. S. Glomski, B. Pandurangan, B. A. Cheeseman, C. Fountzoulas, P. Patel, D. W. Templeton and K. D. Bishnoi, "*Multi-length Scale Modeling of High-pressure Induced Phase Transformations in Soda-lime Glass*," Journal of Materials Engineering and Performance, 20: 1144–1156, 2011.
12. M. Grujicic, W. C. Bell, B. Pandurangan, B. A. Cheeseman, P. Patel and G. A. Gazonas, "*Inclusion of Material Nonlinearity and Inelasticity into a Continuum-Level Material Model for Soda-lime Glass*," Materials and Design, 35: 144–155, 2012.

13. M. Grujicic, W. C. Bell, B. Pandurangan, B. A. Cheeseman, P. Patel and P. G. Dehmer, "*Effect of the Tin- vs. Air-side Plate-glass Orientation on the Impact Response and Penetration Resistance of a Laminated Transparent-Armor Structure,*" Journal of Materials: Design and Applications, 226: 119–143, 2012.

14. M. Grujicic, B. Pandurangan, Z. Zhang, W. C. Bell, G. A. Gazonas, P. Patel and B. A. Cheeseman, "*Molecular-Level Analysis of Shock-wave Physics and Derivation of the Hugoniot Relations for Fused Silica,*" Journal of Materials Engineering and Performance, 21: 823–836, 2012.

15. M. Grujicic, W. C. Bell, B. Pandurangan, B. A. Cheeseman, C. Fountzoulas and P. Patel, "*Molecular-Level Simulations of Shock Generation and Propagation in Soda-Lime Glass,*" Journal of Materials Engineering and Performance, 21: 1580–1590, 2012.

16. M. Grujicic, J. S. Snipes, S. Ramaswami, R. Yavari, and R. S. Barsoum, "*All-Atom Molecular-Level Analysis of the Ballistic-Impact-Induced Densification and Devitrification of Fused Silica*," Journal of Nanomaterials, Volume 2015, Article ID 650625, 2015. DOI: 10.1155/2015/650625.

17. R. Chakraborty, A. Dey and A. K. Mukhopadhyay, "*Loading Rate Effect on Nanohardness of Soda-Lime-Silica Glass,*" Metallurgical and Materials Transactions A, 41: 1301–1312, 2010.

18. O. Tschauner, S-N Luo, P. D. Asimow and T. J. Ahrens, "*Recovery of stishovite-structure at ambient conditions out of shock-generated amorphous silica,*" American Mineralogist, 91: 1857–1862, 2006.

19. A. Salleo, S. T. Taylor, M. C. Martin, W. R. Panero, R. Jeanloz, T. Sands and F. Y. Génin, "*Laser-driven formation of a high-pressure phase in amorphous silica,*" Nature Materials, 2: 796–800, 2003.

20. B. Mantisi, A. Tanguy, G. Kermouche, and E. Barthel, "*Atomistic response of a model silica glass under shear and pressure,*" European Physical Journal B, 85: 304–316, 2012.

21. A. Kubota, M.-J. Caturla, L. Davila, J. Stolken, B. Sadigh, A. Quong, A. Rubenchik and M. D. Feit, "*Atomistic response of a model silica glass under shear and pressure,*" Laser-Induced Damage in Optical Materials 2001, G. J. Exarhos, A. H. Guenther, K. L. Lewis, M. J. Soileau, C. J. Stolz, Editors, Proceedings of SPIE Vol. 4679, pp. 108–116, 2002.

22. G. R. Johnson and T. J. Holmquist, "*An improved computational constitutive model for brittle materials,*" High-Pressure Science and Technology, 1993: Proceedings of the joint International Association for Research and Advancement of High Pressure Science, June 28 – July 2, 1993, pp. 981–991.

23. T. J. Holmquist, D. W. Templeton, K. D. Bishnoi, "*Constitutive Modeling of Aluminum Nitride for Large Strain High-strain Rate, and High-pressure Applications*," International Journal of Impact Engineering, 25: 211–231, 2001.

24. G. R. Johnson and T. J. Holmquist, "*An Improved Computational Constitutive Model for Brittle Materials,*" High Pressure Science and Technology, 1993. (AIP, New York, 1994).

25. ABAQUS Version 6.14, User Documentation, Dassault Systèmes, 2014.

26. M. Grujicic, B. Pandurangan, U. Zecevic, K. L. Koudela and B. A. Cheeseman, "*Ballistic Performance of Alumina/ S-2 Glass-Reinforced Polymer-Matrix Composite Hybrid Lightweight Armor Against Armor Piercing (AP) and Non-AP Projectiles*," Multidiscipline Modeling in Materials and Structures, 3: 287–312, 2007.

CHAPTER 5: CONCLUSIONS AND SUGGESTIONS FOR FUTURE WORK

5.1. Conclusions

In the present work, all-atom (molecular-level and quantum-mechanics) based computational methods as well as the continuum-level computational methods were used to investigate the phenomena of fused-silica devitrification and permanent densification under high-pressure- and shear-loading conditions (as those encountered during a ballistic impact) as well as the potential of these phenomena for improving the ballistic-penetration resistance of fused silica. Based on the work conducted and the results obtained, the following main conclusions can be drawn:

1. By determining the Si-Si, Si-O and O-O partial radial distribution functions, and the coordination numbers for Si and O atoms, before and after a ballistic impact experienced by a sub-micron-sized fused-silica target-plate, devitrification (i.e. conversion into stishovite and α-quartz) and permanent densification of the initial material was established using all-atom non-equilibrium molecular-dynamics simulations.
2. To rationalize the all-atom molecular-level computational results obtained, quantum-mechanical density-functional-theory computational analyses are employed. These analyses helped establish the effect of high pressure and shear on the relative stability of the amorphous fused-silica, crystalline α-quartz and crystalline stishovite, and on the energy barriers associated with the fused-silica $\rightarrow$ α-quartz and fused-silica $\rightarrow$ stishovite conversion reactions. The results obtained demonstrated that under pressures on the order of 50 GPa, and in the presence of shear, stishovite becomes the most stable form of SiO_2

and the energy barrier associated with the fused-silica → stishovite conversion is the smallest. Since the fused-silica target-plate regions beneath and surrounding the hard projectile experience high pressures and shear, formation of stishovite and, to a lower extent, α-quartz from fused silica, as observed in the all-atom molecular-level computational analyses of the ballistic-impact problem, is justified.

3. In order to assess the potential devitrification-induced improvements in the fused-silica ballistic limit, a series of transient, non-linear dynamics finite-element analyses is conducted of a 10-cm-size fused-silica target-plate normal-impact by an armor-piercing bullet. Before such analyses could be conducted, a new material constitutive model for fused-silica had to be developed and linked with the finite-element solver.

4. To include the aforementioned devitrification effects into the fused-silica constitutive response, the classical Johnson-Holmquist-2 (JH2) model was appropriately modified. This was done by using the molecular-level computational results to infer the nature and extent of the devitrification process, as a function of the applied pressure, as well as the effect of the formed stishovite on the material (shear) strength.

5. The finite-element analysis results obtained revealed that only when the bullet incident velocity and, thus, the impact-generated pressures within the fused-silica target-plate are sufficiently high, can the fused-silica devitrification process improve the ballistic-penetration resistance of fused-silica. Furthermore, when the degree of devitrification is high, as observed at the highest bullet incident velocities, the effects of devitrification on the ballistic-penetration resistance are considerable.

5.2. Suggestions for Future Work

Based on the findings obtained in the present work, the following recommendations can be made for its future extension:

1. Modification of the JH2 model carried out in the present work did not include the effect of shear on the propensity of fused-silica to form stishovite under high-pressure- and shear-loading conditions. To include these effects, more detailed investigations, using molecular-level and quantum-mechanical methods and tools, of the effect of shear stresses are needed. Then additional modifications of the JH2 model should be made following the same general procedure developed in the present work.

2. A parametric study involving variations of the key irreversible-devitrification and irreversible-densification parameters within physically realistic limits should be conducted in order to reveal the optimal combination of these parameters which would result in substantial improvements in the ballistic-resistance of fused-silica over a wide range of projectile velocities. Then the ability of various chemical-modification and thermo-mechanical treatment strategies should be investigated in order to assess the feasibility of attaining this optimal set of irreversible-densification parameters. This is an example of the materials-by-design concept, within which an optimal combination of material parameters/properties is identified in order to maximize component-level (the target-plate, in the present case) performance.